AN EXPERIMENTAL STUDY OF THE ROLE OF CONTAMINATION IN THE FORMATION OF CHROMITITES IN THE RING OF FIRE INTRUSIVE SUITE

by

Erin E. Keltie

Submitted in partial fulfilment of the requirements
for the degree of Master of Science

at

Dalhousie University
Halifax, Nova Scotia
December 2018

TABLE OF CONTENTS

List of Tables

List of Figures

Abstract

The Ring of Fire Intrusive Suite (ROFIS) in the James Bay lowlands, Ontario, is emplaced into the 2.734 Ga McFauld's Lake greenstone belt, and hosts five chromite deposits, together comprising ~201.3 million tonnes of measured and indicated chromite resources. The formation process of these and other stratiform chromitites worldwide is still debated, with numerous models for their petrogenesis, one of which is the contamination of a primitive magma by surrounding country rock during ascent and emplacement. Although this process is likely to occur, with evidence for this in the ROFIS context, its effect on chromite crystallization has not been rigorously experimentally tested. This thesis addresses this shortcoming in a series of experiments involving komatiite-ROFIS country rock mixtures, komatiite-magnetite mixtures, and chromite-doped komatiite to measure phase equilibrium, chromite solubility, and chromite composition. Experiments involved equilibrating synthetic komatiite (2187 ppm Cr) containing 0-50 wt.% Cr-free contaminants and 0-2 wt.% chromite on Fe-presaturated Pt loops at 1192-1462ºC and 0.1 MPa at the fayalite-magnetite-quartz (FMQ) oxygen buffer in a vertical tube furnace. Results show that assimilation of Fe-rich material decreases the chromium content of the melt at chromite saturation and decreases the olivine-in temperature, thereby increasing the temperature interval over which chromite crystallizes alone. Assimilation of 16 wt.% of BIF is enough to induce chromite-only crystallization and consistent with other metrics of parental melt contamination. These results indicate that assimilation of Fe-rich country rocks by komatiite may contribute to chromite accumulation in stratiform chromitites.

List of Abbreviations and Symbols Used

a	activity
γ	activity coefficient
BIF	banded iron formation
cm	centimetre
ΔG^o	change in standard state Gibbs free energy
ΔH^o	change in standard state enthalpy
ΔS^o	change in standard state entropy
CCCS	chromium content at chromite saturation
ºC	degrees Celsius
EPMA	electron probe micro-analysis
K_{eq}	equilibrium constant
FMQ	fayalite-magnetite-quartz
R	gas constant
Ga	giga-annum
GPa	gigapascal
GD	granodiorite
Hz	hertz
h	hour
IW	iron-wustite
J	joules
K	kelvin
kg	kilogram
km	kilometre
kV	kilovolt
LA-ICPMS	laser ablation inductively coupled plasma mass spectrometry
Ma	mega-annum
MPa	megapascal

MS	metasediment
m	metre
µm	micrometre
mm	millimetre
mV	millivolts
X	molar fraction
nA	nanoamps
NNO	nickel-nickel oxide
NBO/T	non-bridging oxygens over tetrahedral sites
OB	optical basicity
fO_2	oxygen fugacity
ppm	parts per million
ROFIS	Ring of Fire Intrusive Suite
T	temperature
VMS	volcanic massive sulphide
wt.%	weight percent

Acknowledgements

Funding for this research was generously provided by a TGI 4 grant from Natural Resources Canada (to Drs. James Brenan and James Mungall) and by a research grant from the Society of Economic Geologists. I would also like to thank the Mineralogical Association of Canada for providing me a travel grant to present my research at the Goldschmidt geochemistry conference in Boston, MA.

I thank Dr. James Brenan for giving me the opportunity to work on this project, for all the support and guidance he has provided me, and for tolerating me all the times I barged into his office and completely derailed his previous train of thought. I would also like to thank the other members of my supervisory committee (Drs. Jim Mungall and Yana Fedortchouk) for their support and guidance throughout my degree, and Ryan Weston (VP Exploration, Noront Resources Ltd.) for contributing his extensive knowledge of the ROFIS during committee meetings.

I am grateful to Noront Resources, Ltd. for providing samples and data from the ROFIS. I thank Dan MacDonald for his EPMA support and Roman Kislitsyn for his LA-ICPMS support.

Lastly, I would like to thank my friends and family. I thank Bryan, Kate, and Corin for their comradery (and at times, commiseration) in the experimental petrology lab; my office-mates Laura, Rachel, Taylor, Cody, and Xueni for tolerating all my talk about this project; my family, for their unending support of me; and Danielle, for being by my side through all the highs and lows of these past two (point-three) years.

CHAPTER 1: INTRODUCTION

1.1 Chromite: An Overview

1.1.1 Chromite Structure

Chromite is a member of the spinel group of minerals, which are oxides with the general formula AB_2O_4 (Waychunas, 1991), in which A is a divalent cation, such as Fe^{2+} or Mg, and B are trivalent cations, such as Fe^{3+}, Al, and Cr, or pairs of divalent and quadrivalent cations, such as Fe^{2+} and Ti^{4+}.

The unit cell of spinel group minerals has 8 filled tetrahedral (4-fold coordination) sites and 16 filled octahedral (6-fold coordination) sites. The spinel structural formula is $(A_{1-x}B_x)[A_xB_{2-x}]O_4$, where parentheses and square brackets denote tetrahedral and octahedral sites respectively, A and B are di- and trivalent cations in the case of 2-3 spinels or di- and quadrivalent cations in the case of 2-4 spinels, and x is an inversion parameter equal to 0 in normal $A[B_2]O_4$ spinel structures and 1 in inverse $B[AB]O_4$ spinel structures (Waychunas, 1991; Kurepin, 2005).

1.1.2 Chromite Chemistry

Spinel group minerals are divided into series based on the most abundant B cation. The most abundant B cation in spinel, magnetite, and chromite series minerals are Al, Fe^{3+}, and Cr respectively. The chromite series contains two end-members: chromite *sensu stricto* ($FeCr_2O_4$) and magnesiochromite ($MgCr_2O_4$), between which there

is continuous solid solution (Ghiorso and Sack, 1991). As a result, it is common to refer to any chromite series mineral as "chromite", and this custom is adopted in this work.

Chromite chemistry is generally expressed in terms of Cr# [Cr/(Cr+Al)] and Fe# [Fe^{2+}/(Mg+Fe^{2+})]. Barnes and Roeder (2001) compiled and presented a global dataset of chromite compositions and identified two key compositional trends (Figure 1.1a,b). In general, increasing Cr# is correlated with increasing Fe#, referred to as the Cr-Al trend, and reflects the changes in Cr, Al, Fe, and Mg content of the melt due to fractional crystallization of olivine and plagioclase (Barnes and Roeder, 2001; Roeder and Reynolds 1991). Increases in Fe^{3+} and Fe# are correlated with increased TiO_2, termed the Fe-Ti trend, and reflect increases in the Fe:Mg ratio, Fe^{3+}, and Ti content of the melt due to fractional crystallization. The Fe# of chromite is controlled by two factors: the composition of the melt during crystallization, and subsolidus reactions with coexisting silicates, such as olivine, involving the exchange of Fe^{2+} and Mg, which increase the Fe# of chromite as temperature decreases.

Chromites originating from high pressure environments (Figure 1.1c,d), such as xenoliths in kimberlites, have a clear Cr-Al trend and a large range of Cr# that spans from 0.0 to 1.0. Chromites from ultramafic plutonic cumulate rocks (Figure 1.1e,f), such as ophiolites emplaced in high-temperature and high-pressure conditions, also have a well-developed Cr-Al trend. The composition of chromites from continental mafic intrusions (Figure 1.1e,f) vary depending on whether chromitites are included. Excluding chromitites, a strong Fe-Ti trend is evident. Chromitites from layered mafic intrusions (Figure 1.1e,f) cluster at moderately high Cr# and have a much weaker Fe-Ti trend. Tholeiitic basalts (Figure 1.1g,h) crystallize spinels whose compositions are bimodal

between chromite and magnetite; the Cr# of chromites vary widely and both the Cr-Al and Fe-Ti trends are observed.

Komatiitic spinels (Figure 1.1g,h) often consist of chromite cores and chromian magnetite rims developed during metamorphism and alteration (Barnes and Roeder, 2001). The chromite cores generally have high $Cr/(Cr+Al+Fe^{3+})$ and low Ti content. At a constant Cr#, Fe# can vary greatly in komatiitic chromite. This is due to post-cumulus, subsolidus Fe-Mg cation exchange between chromite and olivine (Irvine, 1965). The metamorphic chromian magnetite rims differ from primary igneous magnetite because the interaction between spinel, silicate phases, and metamorphic fluids depletes the spinel of Al relative to Cr during the process of forming amphibole or chlorite (Barnes and Roeder, 2001). Komatiitic chromites usually have low TiO_2 contents with the exception of chromites from slowly cooled orthocumulate rocks (Barnes, 1998).

1.1.3 Chromite Applications

Chromite is the only ore mineral of chromium, the primary use of which is in the production of stainless steel (USGS, 2018). The most important factor in determining whether a chromite deposit is economic is the Cr:Fe ratio of the ore; a ratio of >1.6 (Murthy et al., 2011) is required to produce ferrochrome rich enough in chromium to be used in the manufacturing of stainless steel. Chromite is mined from stratiform chromitites, which are laterally continuous layers of chromite-rich rock that occur in layered mafic intrusions, as well as podiform chromitites, which are irregularly shaped chromitites that occur in ophiolite complexes. In general, the maximum Cr:Fe ratio of

stratiform chromite deposits increases with age, with the oldest deposits such as the 3.5 Ga Shurugwi and 2.9 Ga Mashaba deposits in Zimbabwe having Cr:Fe ratios of 4.4 and 3.9 respectively (Stowe, 1994). Aside from these two deposits, however, podiform chromite deposits generally have higher Cr:Fe ratios (2.7-4.2) than stratiform chromite deposits (0.7-3.2) (Stowe, 1994).

An estimated 95% of the world's chromium resources are concentrated in the podiform chromitites in Kazakhstan and stratiform chromitites in South Africa; in 2017, most chromite was mined in South Africa, Kazakhstan, India, and Turkey (USGS, 2018). South Africa currently produces the most ferrochrome and the biggest importer of ferrochrome is China, where the majority of the world's stainless steel was produced in 2017 (USGS, 2018).

1.2 Stratiform Chromitites and Their Formation

1.2.1 Features of Stratiform Chromitites

Massive chromitites occur in two forms: as stratiform bodies in layered mafic intrusions and as podiform bodies in ophiolites. What follows is a summary of the general features of stratiform chromitites, as they are the focus of this study.

Layered mafic intrusions usually occur in tectonically stable environments, such as cratons in Africa, Russia, and North America. The layering can extend laterally for hundreds of kilometers, and most intrusions follow a predictable order of mineral crystallization that produces ultramafic rocks at the base and iron-rich rocks at the top (Cawthorn et al., 2005). Intrusions with an ultramafic parental magma, such as the

Bushveld Complex in South Africa, the Great Dyke in Zimbabwe, and the Stillwater Complex in the USA have well-developed ultramafic portions (Cawthorn et al., 2005). Those with basaltic parental magma, such as the Skaergaard intrusion in Greenland, may not include an ultramafic portion (Cawthorn et al., 2005). Stratiform chromitite deposits occur in the ultramafic rocks at the base of layered mafic intrusions and are associated with PGE deposits and vanadiferous magnetite deposits that occur further up the vertical section in more evolved, mafic rocks (Cawthorn et al., 2005). Some intrusions do not develop well-defined layers, such as the Noril'sk-Talanakh sills in Russia, and those that develop in tectonically active areas, such as the Lac des Iles intrusion in Canada, the Duluth Complex in the USA, and the Kemi intrusion in Finland, are irregularly shaped (Cawthorn et al., 2005).

Compared to the estimated concentrations of chromium in their source magmas, stratiform chromitite deposits are enriched in chromium by a factor of ~1000 (Cawthorn et al., 2005). The process that causes this concentration has been debated for decades, but one principle is widely acknowledged: closed-system fractional crystallization of the parental magma is unlikely to be the sole cause, as mass balance indicates there is more chromium in the chromitite deposits than could have been contributed by the observed volume of parental magma (Cawthorn et al., 2005). Several proposed mechanisms for chromitite formation will be discussed in section 1.2.2.

The most intensely studied layered mafic intrusion is the 2.06 Ga Bushveld Complex in South Africa. It is the largest known ultramafic-mafic intrusion, thought to occupy an area of >90,000 km^2 (Finn et al., 2015). Stratiform chromitites of the Bushveld Complex occur in the Rustenburg Layered Suite (RLS), which is subdivided

into several vertical zones based on changes in lithology (Cameron, 1980). From bottom to top they are the Marginal, Lower, Critical, Main, and Upper zones; chromitite layers occur in the Critical Zone (Cawthorn et al., 2005). The chromitite seams are numbered in sequence from bottom to top, and are subdivided into the Lower (LG1-LG7), Middle (MG1-MG4), and Upper (UG1-UG3) groups.

Due to the observed lateral continuity of layers in the Bushveld Complex, it has generally been assumed that the layers indicate aggradation of crystals on the floor of a massive magma chamber. Recent field observations and geochronological data from the RLS (Mungall et al., 2016; Mukherjee et al., 2017), however, have challenged this assumption. Mungall et al. (2016) conducted high-precision U-Pb isotope dilution-thermal ionization mass spectrometry (ID-TIMS) to determine ages of zircon ($ZrSiO_4$) and baddeleyite (ZrO_2) from the lower Main Zone and Upper Critical Zone of the RLS. They found that the UG1 (2056.28±0.15 Ma) and MG4a (2056.04±0.15 Ma) chromitite units are older than the underlying MG2a (2055.68±0.20 Ma) chromitite unit, signifying out of sequence emplacement. In addition, the underlying Lower Critical Zone has been dated at 2055.40±0.30 Ma to 2055.65±0.38 Ma (Zeh et al., 2015), also younger than the overlying UG1. Mungall et al. (2016) interpreted these results to suggest that the Bushveld Complex has a complex emplacement history in which the noritic rocks of the Upper Critical Zone intruded first, followed by the mafic Main and Upper zones, then ultramafic sills episodically intruded into the existing mafic rocks at successively lower levels.

Mukherjee et al. (2017) studied the field relationships of the UG1 chromitite seam with the anorthosites below and orthopyroxenites above it. The UG1 chromitite forms

potholes, semicircular depressions with steep sides that cut into the anorthosite below them, and the potholed chromitite locally lays above an orthopyroxenite layer, whereas this layer usually overlies the UG1 chromitite regionally. A thick (15 cm) chromitite layer also laterally protrudes from the pothole into the anorthosite, truncating layering in the anorthosite defined by interstitial pyroxenite layers. The contact between the chromitite layer and anorthosite away from the pothole truncates layering in the anorthosite, and in some areas, remnant anorthosite lenses are preserved within the chromitite. Mukherjee et al. (2017) interpreted these field relationships to suggest sill-like emplacement of UG1 with simultaneous magmatic chemical erosion of the anorthosite.

1.2.2 Models for the Origin of Stratiform Chromitites

The process by which stratiform chromitites form is still debated, with models for their petrogenesis including gravitational settling of liquidus chromite to the base of an evolving magma chamber, mechanical sorting of chromite during flow, transient changes in pressure (Latypov, 2018; Lipin, 1993), addition of water to the magma (Nicholson and Mathez, 1991), changes in oxygen fugacity, magma mixing between primitive and evolved magma (Irvine, 1977), and contamination of a primitive magma by surrounding country rock (Irvine, 1975). A brief review of these mechanisms is provided below.

1.2.2.1 Gravitational Settling

The simplest hypothesis for stratiform chromitite formation is that they represent the gravitational settling of dense chromite crystals to the bottom of a wide, shallow magma chamber (Kruger, 2005), but there are numerous lines of evidence that do not support this mechanism. Eales (2000) showed that the amount of chromium in the chromite and orthopyroxene in the Critical Zones of the Bushveld Complex is more than could be provided by the volume of magma thought to be parental to the intrusion. Calculations showed that the Critical Zone contains ~1.4 wt.% Cr_2O_3, requiring a column of magma containing ~0.15 wt.% Cr_2O_3 with a thickness of ~15 km, double the thickness of the layered mafic rock sequence. This problem could be overcome by increasing the initial Cr content of the magma or increasing the volume of magma that was parental to the Bushveld Complex, but the latter solution implies that the excess magma was removed from the system, and there are no suggestions as to where it might have gone (Kruger, 2005). Another problem with this hypothesis is that geochronological work by Mungall et al. (2016) has shown that some chromitite horizons are in fact older than the layers they overly, suggesting that they were emplaced as sills. Finally, Mukherjee et al. (2017) showed textural evidence of remnant anorthosite lenses within chromitite layers, indicating that the Bushveld Complex chromitites did not form from simple gravitational settling.

1.2.2.2 Mechanical Sorting

Another relatively simple hypothesis for stratiform chromitite formation is that chromite was mechanically sorted from silicate phases during flow and deposited as a layer on the floor of the magma chamber. Mondal and Mathez (2007) observed no difference in the composition of orthopyroxenites that bracket the UG2 chromitite layer in the Bushveld Complex and suggested that it was formed by an injection of a magmatic slurry containing chromite and orthopyroxene crystals with subsequent mechanical sorting then rapid accumulation of chromite on the magma chamber floor. Mungall et al. (2016) suggested that chromitite sills in the Bushveld Complex could have formed by intrusion of olivine-orthopyroxene-clinopyroxene-chromite crystal mushes followed by mechanical sorting of the chromite grains. In this model, escape of remaining melt from the sill could address the chromium mass balance problem by accounting for the "missing" volume of komatiitic melt required to produce the mass of chromium in the chromitite layers. Jenkins and Mungall (2018) argued that mechanical sorting of chromite and olivine could also explain the variability in the ratio of olivine to chromite in the Ultramafic Series of the Stillwater Complex.

1.2.2.3 Transient Changes in Pressure

Lipin (1993) showed that the expansion of the chromite liquidus phase field with increased pressure could explain stratiform chromitite formation via transient increased pressure in the magma chamber. Due to the topology of the peritectic curves in a ternary system of forsterite-anorthite-silica, a magma whose liquidus phases are olivine and

spinel at 0.1 MPa would crystallize spinel alone at 1 GPa (Liu and Presnall, 1990). It follows that chromitite layers could represent transient periods in which increased pressure in the magma chamber caused chromite-only crystallization until the pressure dissipated (Lipin, 1993). Such pressure increase could be caused by exsolution of CO_2 during the ascent of mafic magma to a shallow magma chamber, because the solubility decreases with pressure, but the increase in volume of CO_2 is dramatic during the transition from >6 km depth to the surface (Lipin, 1993). Although it is a common assumption that magma chambers are unlikely to withstand significant overpressurization, Pollard et al. (1983) showed that transient overpressure is possible. One problem with this model is that there is little experimental evidence to verify that CCCS is affected by pressure, with the only available data (Roeder and Reynolds, 1991) suggesting that CCCS increases only slightly with increasing pressure, which would result in chromite dissolution. Another problem is that the phase equilibria used to support the model are based on a chromium- and iron-free system, making the application to natural magmas uncertain.

Latypov et al. (2018) recently modified this model by considering chromium in the system, and analyzed the phase relations in the forsterite-anorthite-silica-magnesiochromite system. They identified a "chromite topological trough" between the orthopyroxene/olivine and anorthite phase volumes, whose position shifts away from plagioclase and towards the forsterite vertex at low pressures, meaning that a melt saturated in orthopyroxene or olivine at high pressures would shift into the chromite stability volume at low pressures during ascent to shallow levels (Latypov et al., 2018). They used the alphaMELTS thermodynamic model to trace the phase relations of a

model Bushveld parental magma from 0.1 to 1 GPa and found the liquidus phase assemblage was orthopyroxene-chromite at pressures >0.6 GPa, shifting to chromite as the sole liquidus phase at lower pressure. However, it is well documented that the MELTS thermodynamic model is not accurate for spinel saturated compositions. Nikolaev et al. (2018) compared experimental spinel phase equilibrium data to MELTS output and demonstrated that both the MELTS and pMELTS thermodynamic models overestimate the temperature of spinel saturation by 100°C or more at all pressures, temperatures, and compositions considered. This effect would have resulted in erroneously high chromite liquidus temperatures in the models calculated by Latypov et al. (2018), leading to incorrect results and interpretations.

1.2.2.4 Addition of Water

Ford et al. (1972) showed that in a system saturated in olivine, anorthite, diopside, and silica, the addition of water to a lunar basalt increased the spinel liquidus field at the expense of the plagioclase, olivine, and pyroxene fields. Sisson and Grove (1993) showed that the addition of 1 wt.% water to basalt supresses the formation of silicate phases, but not oxide phases such as magnetite. Nicholson and Mathez (1991) developed a model for stratiform chromitite formation in which a melt originally saturated in orthopyroxene and plagioclase is hydrated by water propagating through fractures in the intrusion footwall. The hydration would cause the orthopyroxene and plagioclase to be resorbed and chromite to begin to crystallize. Much like gravitational settling, this model has a mass balance problem. For the amount of chromite seen in the Bushveld Complex to form by this mechanism, Mondal and Mathez (2007) estimated based on the observed

Cr content of the pyroxenes that 50 times its mass in clinopyroxene and 100 times its mass in orthopyroxene would have to have been resorbed. In the example of the UG2 chromitite layer, this would require resorption of all the orthopyroxene in a 100 m thick body of partially crystallized magma, which Mondal and Mathez (2007) deemed geologically unreasonable.

1.2.2.5 Changes in Oxygen Fugacity (fO_2)

Cameron and Desborough (1969) suggested that mixing two magmas with different fO_2 values could induce chromite crystallization. Numerous experimental studies (Barnes, 1986; Murck and Campbell, 1986; Roeder and Reynolds, 1991) have shown that CCCS decreases with increasing fO_2. Changes in fO_2, however, would be expected to impact the chemistry of other minerals in layered mafic rocks, such as orthopyroxene. Barnes (1986) showed that the chromium content of orthopyroxene increases with increasing fO_2, which suggests that if an increase in fO_2 causes chromite crystallization, there should be an increase in the Cr/Al ratio of the orthopyroxene in pyroxenites above chromitite layers. Mondal and Mathez (2007) found that the Cr/Al ratios of the orthopyroxene in norite and pyroxenite both below and above the UG2 chromitite layer were similar, which is inconsistent with the changes predicted by this model.

1.2.2.6 Magma Mixing

The magma mixing hypothesis is based on the ternary liquidus phase relations for the system olivine, chromite, and silica (Fig. 1.2.1). The salient feature of the relevant phase diagram is that the cotectic boundary between olivine and chromite is curved in such a way that the proportion of chromite to olivine decreases as the two crystallize together, and the peritectic between olivine, orthopyroxene, and chromite, such that when orthopyroxene begins to crystallize, both olivine and chromite cease to form (Irvine, 1977). For example, a liquid parental to the Critical Zone of the Bushveld Complex would initially plot in the olivine primary phase volume, and evolve by olivine crystallization towards the cotectic between olivine and chromite. Once reaching the cotectic, the liquid will evolve along the cotectic until reaching the peritectic, resulting in the crystallization of orthopyroxene alone (Irvine 1977). The curved nature of the olivine-chromite cotectic suggests that if a more primitive melt on the cotectic mixed with a more evolved melt in the orthopyroxene field, the resulting melt composition would fall in the chromite-only crystallization field (Fig. 1.2.2). Irvine (1977) hypothesized that this process could explain differences in the sequences of lithologies in layered mafic intrusions, where different proportions of primitive and evolved magma result in different orders of crystallization. One shortcoming of this hypothesis is that it is based on a simplified system with only three components: MgO, Cr_2O_3, and SiO_2. The topology of cotectic boundaries in a more geologically realistic system, with more components, is not well known, and it is difficult to quantitatively predict the phases that would crystallize due to mixing. In addition, mixing of a primitive magma with an evolved magma would be expected to impact the chemistry of other lithologies above the

chromitite layers in layered mafic intrusions, for instance by causing an increase in the Mg# [Mg/(Mg+Fe^{2+})] of olivine or orthopyoxene. Mondal and Mathez (2007) did not find a resolvable increase in the Mg# of orthopyroxene in norites and pyroxenites above the UG2 chromitite layer, hence inconsistent with the layer forming by injection of primitive magma into a more evolved composition.

1.2.3.7 Contamination

The contamination hypothesis is based on the same ternary system as for magma mixing (Fig 1.2.3). Instead of shifting a primitive melt into the chromite-only crystallization field by mixing with an evolved melt, the contamination hypothesis suggests that the same could be achieved by assimilation of more siliceous country rock (Irvine 1975). Irvine (1975) provided evidence in support of this with the observation that chromite grains in the Muskox intrusion (Nunavut, Canada) chromitite layers contain melt inclusions of granitic bulk composition. Similarly, Spandler et al. (2005) described melt inclusions in chromite from the Stillwater Complex (Montana, USA) that could not be explained by evolution of a melt by fractional crystallization, but instead by mixing ultramafic and trondhjemitic members. Irvine (1975) also noted the presence of country rock xenoliths that were rounded and embayed at the top of the Muskox intrusion. Irvine later criticised his hypothesis, stating that contamination by a Si-rich country rock would increase the alkali content of the melt and shift the olivine-orthopyroxene cotectic boundary toward the silica vertex in such a way that geologically improbable amounts of assimilation would be required to achieve chromite-only crystallization (Irvine, 1977).

However, in the context of crustal contamination, there are other possible contaminants besides Si-rich granodiorites, so the model has not been tested exhaustively.

In summary, field observations from the Bushveld Complex indicate that stratiform chromitites may not simply be a product of closed-system fractional crystallization and gravitational settling of chromite to the bottom of a magma chamber. Although field observations and geochronological studies of stratiform chromitite deposits inform us about their emplacement history, such work does not provide unique constraints on the geochemical processes involved in their formation. Experimental studies provide a complementary approach, in which factors that may contribute to significant chromite accumulation may be isolated and tested separately.

1.2.3 Previous Experimental Studies

1.2.3.1 Chromium Content at Chromite Saturation (CCCS)

Murck and Campbell (1986) conducted experiments in which natural basaltic and komatiitic melts were doped with chromite and equilibrated at atmospheric pressure in vertical-tube gas mixing furnaces at 1150-1500ºC and fO_2 between the iron-wustite (IW) and nickel-nickel oxide (NNO) oxygen buffers. Roeder and Reynolds (1991) conducted similar experiments at 1300ºC and $\log fO_2$ between -0.70 and -12.78. Murck and Campbell (1986) found that CCCS increases with increasing temperature (Figure 1.2.4) and decreases with increasing fO_2 (Figure 1.2.5), which was also confirmed by Roeder and Reynolds (1991). Murck and Campbell (1986) showed that CCCS is higher in komatiitic melts than basaltic melts, but that this compositional effect diminishes with

increasing temperature, and disappears at temperatures above 1400ºC. Experiments were also done to test the effect of alkalis on CCCS, with results indicating that as the K_2O content of the melt increased from 2 to 16 wt.%, CCCS decreased from 462 to 366 ppm. Similar experiments by Barnes (1986) using a synthetic analogue of a proposed parental magma to the Bushveld Complex doped with orthopyroxene ($[Mg,Fe]_2Si_2O_6$) and chromite confirmed Murck and Campbell's findings that CCCS increases with increasing temperature and decreases with increasing fO_2. The dependence on fO_2 has been explained as a result of the reduction of Cr^{3+} to Cr^{2+} at fO_2 lower than the FMQ buffer (Murck and Campbell, 1986; Barnes, 1986). Murck and Campbell (1986) did not offer a detailed explanation as for why CCCS decreases with increasing alkali content, but did suggest that it may reflect that Cr^{3+} does not exist as charge-balanced complexes with monovalent cations in the melt.

Liu and Presnall (1990) did experiments using mixtures of synthetic $CaAl_2Si_2O_8$, $MgSiO_3$, and SiO_2 at 1390-1650ºC and 2 GPa in a piston-cylinder apparatus. They showed that at high pressures the spinel liquidus phase field expands relative to that at atmospheric pressure (Liu and Presnall, 1990). This suggests that CCCS decreases with increasing pressure, however experiments done by Roeder and Reynolds (1991) attempting to confirm any such dependence showed that CCCS may in fact increase with increasing pressure: at 1300°C and FMQ – 1, CCCS in a terrestrial basalt increased from 1389 ppm at 0.1 MPa to 1724 ppm at 1 GPa.

Systematic study of melt composition effects on the CCCS is limited. Ford et al. (1972) found that the addition of water and alkalis to a lunar basalt resulted in spinel saturation at 25 MPa, whereas a dry lunar basalt became saturated in spinel at 1.1 GPa.

Sisson and Grove (1993) conducted experiments using natural and synthetic materials at 925-1132ºC, 200 MPa, and the NNO oxygen buffer in cold-seal pressure vessels. They found that the addition of ~1 wt.% water to basaltic compositions decreased the magnitude of the temperature interval over which silicate phases crystallize before spinel by 150ºC, indicating that the addition of water supresses the crystallization of silicate phases more than oxide phases. In other terms, the addition of water does not appreciably change the solubility of magnetite. Another compositional effect on CCCS was shown by Mungall and Brenan (2014), wherein basalt was equilibrated in chromite capsules in gas-mixing furnaces at varying fO_2. They found that CCCS decreased with increasing FeO content of the melt, a result further confirmed in this study.

1.2.3.2 Chromite Composition

Figure 1.2.6 summarizes the composition of chromite produced in previous experimental studies on komatiitic melts. Murck and Campbell (1986) found that at a fixed fO_2 of FMQ, the Fe# of chromite increases with decreasing temperature, and the Cr# decreases with decreasing temperature. This was confirmed by Roeder and Reynolds (1991) and Brenan et al. (2012). Both Murck and Campbell (1986) and Roeder and Reynolds (1991) also determined that the Fe# of chromite increases with increasing fO_2. Komatiitic starting compositions yield chromite with lower Fe# than those from basaltic starting compositions (Murck and Campbell, 1986; Roeder and Reynolds, 1991). Roeder and Reynolds (1991) also found that increased pressure does not affect chromite Fe# or Cr#. The effects of temperature and fO_2 on Cr# are small relative to Fe# (Murck and Campbell 1986; Roeder and Reynolds, 1991).

1.3 Chromitites of the Ring of Fire Intrusive Suite

The discovery of chromitites in the Ring of Fire Intrusive Suite (ROFIS), located in the James Bay lowlands of northern Ontario, followed soon after the discovery of the Eagle's Nest Ni-Cu-PGE-Fe deposit in 2007. The main focus of this thesis is to understand the genesis of these chromitites, and what follows is the geological context of the ROFIS. The majority of the following information about the ROFIS is derived from Mungall et al. (2010).

1.3.1 Regional Geology

The Ring of Fire Intrusive Suite (ROFIS) was emplaced into the McFaulds Lake greenstone belt, which is within the Oxford-Stull domain of the North Caribou superterrane of the Superior province (Figure 1.3.1). Very little field work has been done in this region due to the swampy terrane and scarce outcrop; most knowledge about the geology has been from drill core or geophysical surveys obtained in the pursuit of diamondiferous kimberlites.

Plutonic rocks within the McFaulds Lake greenstone belt have been dated between 2.727-2.683 Ga (Rayner and Stott, 2005). Intermediate volcanic rocks from the McFaulds Lake VMS deposits have a U-Pb age of 2.737 Ga and a crust formation age of 2.84 Ga. A combination of airborne magnetometer surveys and diamond drill holes found that the McFaulds Lake greenstone belt is shaped like a half-circle 60 km in diameter (Fig. 1.3.2) and contains silicate- and oxide-facies iron formation in addition to felsic intrusive rocks, VMS deposits, and magmatic sulphide deposits. Mungall et al.

(2010) interpreted the spatial proximity of iron formation, volcanic rock, VMS deposits, and magmatic sulphide deposits to indicate that the McFaulds Lake greenstone belt is a package of supracrustal metasedimentary and metavolcanic rocks that underwent several deformation events and whose volume was expanded by the intrusion of felsic magmas.

1.3.2 Geology of the Ring of Fire Intrusive Suite

A major episode of magmatism occurred some time after the deposition of the McFaulds Lake iron formation, forming an intrusive suite of peridotitic to dunitic dikes and sills, anorthosite, ferrogabbro, and intermediate to felsic lavas and pyroclastics along with ferrograbbro sills collectively named the ROFIS. The ROFIS can be split into domains that contain various kinds of mineral deposits, each with different geophysical responses. A zone of weak magnetic response with a northeast-southwest lineament is interpreted as a series of stacked felsic intrusions, similar to the granodiorite that hosts the Eagle's Nest Ni-Cu-PGE-Fe deposit. A string of highly magnetic bodies follow the southeastern margin of the felsic intrusions and also appear as extensive sheets to the northeast; the bodies are ultramafic dikes and layered sills of dunite, harzburgite, and orthopyroxenite which host the Blackbird, Big Daddy, Black Label, and Black Thor chromitite deposits. To the northeast, a prominent structure of concentric layers of high magnetic response was drill tested and found to contain layers of anorthosite and magnetite-rich ferrogabbro, and was named the Thunderbird V-Ti-Fe deposit.

A sample of ferrogabbro taken about 12 km east of the Eagle's Nest deposit in the Ring of Fire Complex was dated at 2734.5 +/- 1.0 Ma by zircon U-Pb, which is within

error of the age of the McFaulds Lake VMS deposits (2737 +/- 7 Ma), determined by Rayner and Stott (2005). Mungall et al. (2010) also obtained a zircon U-Pb age of 2773.37 +/- 0.9 for a tonalite host rock of the Eagle's Nest deposit. These ages imply that the magmatism that formed the ROFIS was contemporaneous to the McFaulds VMS deposits. Mungall et al. (2010) suggested that the ROFIS was emplaced on the northern margin of the microcontinent now known as the North Caribou superterrane, on thinned lithosphere in an active volcanic belt at 2735 Ma, prior to the collision of the microcontinent with the North Superior superterrane ca. 2720 Ma. They also noted that the Bird River ultramafic and mafic intrusions that also host Ni-sulphide and chromitite deposits were emplaced in the southern margin of the same microcontinent ca 2745 +/- 5 Ma and suggested that the pair of intrusive suites could indicate the existence of a single large igneous province.

1.3.3 Chromitite Geology and Chemistry

1.3.3.1 Geology

The ROFIS contains five known chromitite deposits: Black Thor, Big Daddy, Blackbird, Black Label, and Black Creek (Fig. 1.3.2). Together these deposits comprise ~201.3 million tonnes of measured and indicated chromite resources (Aubut, 2015). The following information on the Blackbird deposit is derived from Azar (2010), and information on the Black Thor, Black Label, and Big Daddy deposits are derived from Laarman (2014).

The Blackbird deposit occurs within a dunite sequence near the Eagle's Nest deposit. Azar (2010) described the Blackbird deposit as having several lithological facies, including harzburgite, dunite, pyroxenite, chromitite, and granodiorite, with a shear zone separating the contact between the ultramafic units and the granodiorite. Chromite in the deposit occurs massive and non-massive, with the latter being subdivided into disseminated, clastic, semi-massive, and intercalated. Disseminated chromite occurs as isolated, sub-millimeter euhedral to subhedral grains, comprising 1-25% of the modal abundance in ultramafic silicate rock. Clastic chromite occurs as isolated, 1-20 cm clusters in peridotite and is interpreted to be derived from pre-existing small chromitite layers that were disaggregated during magma injection. Semi-massive chromite is the term used by geologists from Noront Resources Ltd. when chromite comprises 25-45 modal % of the sample. Intercalated chromite occurs as thin lenticular bands of massive and semi-massive chromite, from 1 cm to several meters thick, that tend to flank larger chromitite lenses. Massive chromite occurs as lenticular or tabular bodies of chromitite that extend for hundreds of meters, and the modal abundance of chromite is usually 65-75%. This chromitite usually has an orthocumulate texture, with interstitial serpentine, talc, magnesite, and kammererite, a chromian clinochore. Chromite crystals often contain inclusions containing Mg-rich hydrous silicates such as serpentine, phlogopite, and chlorite, as well as Na-rich minerals such as albite and pargasite.

The Big Daddy deposit occurs 5 km north of the Blackbird deposit. It is a stratiform layer of chromitite underlain by dunite and overlain by pyroxenite. The chromitite occurs in disseminated, semi-massive, and massive forms. The main

chromitite layer is up to 60 m thick and extends >1.4 km along strike, and the chromite occurs as euhedral grains 0.1-0.2 mm in diameter.

The Black Label and Black Thor deposits occur 3 km northeast of the Big Daddy deposit. Figure 1.3.3 shows a generalized stratigraphic column of these chromitite deposits. The Black Label chromitite extends 2.2 km along strike and is overlain by the same dunite layer that lies beneath the Big Daddy deposit. The Black Thor chromitite extends 2.6 km along strike and is comprised of two chromitite layers that range in thickness from 10s to 100s of meters separated by a band of dunite-hosted disseminated chromite in dunite. This contrasts the more typical occurrence of disseminated chromite in these deposits which is hosted in harzburgite that has been altered to serpentine, talc, and kammererite. Intermittent chromitite beds between disseminated and semi-massive or massive chromitites range from 10-30 cm in thickness. Intercalated silicate layers are 50-100 cm intervals of dunite or pyroxenite. The bottom of the intermittent chromitite layers are usually sharp, while the tops grade into dunite with disseminated chromite. Semi-massive chromite occurs with olivine or pyroxene cumulate with 45-70 modal % chromite. The chromite in the massive chromitite occurs as meso- to adcumulus with interstitial pyroxene. The Black Thor and Big Daddy chromitite layers are >90 modal % chromite. The Black Label chromitites are >80 modal % chromite and occur as wavy to lensoidal layers with magmatic breccia textures.

1.3.3.2 Geochemistry

Azar (2010) presented major and trace element analyses of four drill cores from the Blackbird chromitite, labelled BB2-1 to BB2-4. Whole-rock chemistry of BB2-1 exhibits a high but variable Mg#, with nearly constant Cr#, and that higher Mg# is correlated with high Fe^{3+}. Sample BB2-2 shows variability due to a high frequency of intermittent chromitite beds, but thicker chromitites have the highest Cr# and exhibit an increase in Zr concentrations down hole. BB2-3 is similar to BB2-2. Sample BB2-4 shows a steady decrease in Cr# and Mg# down hole along with increasing TiO_2. Overall, the whole rock chemistry of the drill core suggests that the chromite-forming magma was becoming more evolved down-hole. The Cr# of chromite in massive chromitite at Blackbird clusters around ~0.70 (Fig. 1.3.4), ranging from 0.67-0.73. Fe# is more variable, with an average of 0.46 and a range from 0.40-0.60, likely due to subsolidus re-equilibration with olivine (see below). Where chromitites are adjacent to pyroxenites, chromite has lower Cr# and Mg#. The Cr# of chromite from the Black Thor deposit ranges from 0.40-0.95, clustering around 0.6-0.8, while the Fe# ranges between 0.50-0.93. The following section describes how the Black Thor chromite samples were used to estimate the fO_2 of the ROFIS chromitites.

1.3.4 Estimates of the Oxygen Fugacity of the ROFIS Chromitites

Samples from drill core from the Black Thor and Eagle's Nest deposits provided by Noront Resources, Ltd. were analysed in order to estimate the fO_2 of the ROFIS, as this is clearly an important parameter affecting chromite solubility, based on previous

experimental work. Ballhaus et al. (1991) developed an oxygen barometer based on the compositions of olivine and spinel in orthopyroxene-saturated melts, applicable to mantle rocks and mantle-derived melts at temperatures <800ºC:

$$\Delta log(fO_2)^{FMQ} = 0.27 + \frac{2505}{T} - \frac{400P}{T} - 6log(X_{Fe}^{ol}) - \frac{3200(1-X_{Fe}^{ol})^2}{T} + 2log(X_{Fe^{2+}}^{sp}) + \frac{2630(X_{Al}^{sp})^2}{T}, \quad (1.1)$$

in which $\Delta\log(fO_2)^{FMQ}$ is oxygen fugacity expressed in terms of deviation from the FMQ buffer, T is temperature in K, P is pressure in GPa, and X is molar proportion. The samples from the Black Thor deposit contain the requisite assemblage of olivine, orthopyroxene, and spinel for the oxygen barometer. The olivine and chromite analyses were conducted by Mr. Sam Robb under the guidance of Dr. Yanan Liu in the summer of 2017 using the JEOL JXA8230 electron microprobe in the Department of Earth Sciences at the University of Toronto. Appendix A contains summaries of chromite and olivine analyses and descriptions of the analytical conditions. The fO_2 for individual chromite-olivine pairs was calculated using the method of Ballhaus et al. (1991), with input temperatures estimated after the method of O'Neill and Wall (1987), as modified by Ballhaus et al. (1991). The mole fractions of ferrous iron, ferric iron, and aluminum in the chromite were calculated using the method of Barnes and Roeder (2001).

As described by Barnes (1998), komatiite chromite compositions are susceptible to modification by metamorphism and alteration, leading to compositions that do not reflect equilibrium with coexisting olivine. To account for these effects, the chromite composition dataset has been filtered to exclude analyses that do not meet the criteria for magmatic equilibrium, including unusually high MnO concentrations and low Mg#

[Mg/(Mg+Fe^{2+})]. Figure 1.3.5 shows the MnO-Mg# variation for the Black Thor dataset, with a clear correlation at high Mg#, consistent with presumed chromite-olivine equilibrium, and strong deviation from this trend at low Mg# (>0.15), reflecting non-magmatic processes, such as replacement by Cr-bearing magnetite during metamorphism and hydrothermal alteration (Barnes, 1998).

Oxygen fugacities recorded by the Black Thor chromitites estimated using the method of Ballhaus et al. (1991) are summarized in Table 1.3. Sample IDs 202.5 and 209.5 are olivine orthocumulates with accessory chromite from Eagle's Nest, and sample IDs 221-2, 264-4, 251-2, and 209-1 are olivine websterite, chromitite, hybrid chromite harzburgite, and chromitite xenoliths, respectively, from Black Thor. They span a range of >10 orders of magnitude, but are strongly correlated with temperature. All measured oxygen fugacities are more oxidized than the FMQ buffer (Fig. 1.3.6), varying from FMQ+1 at T > 700ºC to FMQ+2 at T < 500ºC. The accuracy of the Ballhaus et al. (1991) fO_2 calibration is less certain below ~800ºC, owing to changes in the spinel ordering at these conditions, which could in part explain the apparent deviation to more oxidizing conditions recorded for the lowest temperature samples. Results for the samples reflecting equilibration nearest to magmatic conditions suggest oxygen fugacities ~0.5 log units higher than the FMQ buffer.

1.3.5 Models for the Formation of the ROFIS Chromitites

Azar (2010) described the chromite mineralization in the Blackbird deposit as sill-hosted and conduit-style, distinct from other stratiform chromitites such as those from the

Bushveld Complex due to their lenticular shape. Azar (2010) used MELTS to model chromite solubility and found that a column of magma of the composition thought to be parental to the ROFIS would have to be 1.2-4.7 km to crystallize only 1 m of chromitite, and suggested that other processes such as magma contamination or addition of water are required. Reiners et al. (1995) presented models that showed MORB or high-alumina basalt can assimilate 5-18 percent of its weight while crystallizing 3-7%, and Azar (2010) postulated that more primitive magmas such as komatiites could assimilate even more. Evidence that contamination occurred during the formation of the Blackbird deposit includes banded iron formation xenoliths and enriched REE patterns relative to typical komatiites (Azar, 2010). MELTS modelling indicated that 0.2 wt.% water addition supresses the orthopyroxene liquidus for the ROFIS parental melt composition, resulting in cumulates with higher modal percentages of chromite. Azar (2010) ultimately concluded that the Blackbird chromitites could have formed by a combination of assimilation of water-bearing country rock and mechanical separation of chromite into lenticular bodies. Azar (2010) suggested that gravitational and mechanical sorting of chromite in a turbulent magma chamber could produce the lenticular chromitite bodies.

Laarman (2014) explained the Black Label, Black Thor, and Big Daddy chromitites as a result of a two-stage process of early gravitational settling of chromite followed by in situ adcumulate chromite growth. The increasing Mg# of chromite up drill hole was explained by repeated injection of new, more primitive magma as gravitational settling of chromite occurred (Laarman, 2014). Later, *in situ* chromite formation explained why some chromitites would contain high MgO chromite and low MgO chromite at the same depth, as well as lower MgO and Cr_2O_3 content of the rims of

chromite grains compared to their cores (Laarman, 2014). Two stages of crystallization also explained why only some chromite contained silicate inclusions, as the adcumulate chromite phase would be more likely to trap melt during growth (Laarman, 2014). Laarman (2014) also stated that crustal contamination likely occurred during komatiite emplacement, resulting in the observed negative Nb-Ta and Zr-Hf anomalies in the komatiitic magma.

In summary, the existing hypotheses for the formation of the ROFIS chromitites include crustal contamination, magma mixing, water addition, and gravitational or mechanical sorting, with general agreement that a combination of these processes likely occurred together during magma emplacement.

1.4 Statement of Hypothesis and Thesis Objectives

1.4.1 Hypothesis

Despite the popularity of the contamination model of chromitite formation and its success in at least partially explaining the formation of the ROFIS chromitites, there remain sparse experimental data on the effect of contamination on phase equilibria, CCCS and chromite composition. This thesis tests the hypothesis proposed by Irvine (1975) that contamination of a primitive komatiitic melt by country rocks causes the melt to shift into a field of chromite-only crystallization. It also tests the hypothesis proposed by Azar (2010) that the crustal contamination process played a significant role in the formation of the Blackbird chromitite deposit.

1.4.2 Objectives

The long term objective of this study is to evaluate the contamination hypothesis for the formation of the ROFIS chromitites by comparing experimentally-produced and natural ROFIS chromite. The short term objectives of this study that will ultimately facilitate achievement of this long term objective are:

1. Perform experiments in which komatiite melts with varying amounts of Cr are contaminated with a range of crustal contaminants whose compositions are based on those from the ROFIS;

2. Obtain data on how different crustal contaminants affect phase equilibria, CCCS, and chromite composition; and

3. Compare experimental data to measured values from the ROFIS chromitites.

CHAPTER 2: METHODS

2.1 Experimental Methods

2.1.1 Synthesis of Starting Materials and Sample Preparation

Synthetic starting materials were prepared by mixing reagent-grade oxides and carbonates in an agate mortar and pestle under ethanol until a well-mixed and very fine-grained powder was achieved. The mixture was then calcined in a Pt crucible at 1000°C in air for 12 hours and ground in an agate mortar and pestle. The calcined material was then fused at 1530°C in air for 30 minutes, ground in an agate mortar and pestle, fused for another 30 minutes at 1530°C in air, and finally ground in an agate mortar and pestle, saving a small piece of fused glass to be analyzed by EMPA and LA-ICPMS. Four synthetic starting materials were prepared based on compositions from Azar (2010): modelled komatiite parental to the ROFIS (K), banded iron formation (BIF), granodiorite (GD), and metasediment (MS). Two batches of komatiite (K1 and K2) were synthesized and contained 2187 and 2121 ppm Cr respectively; BIF, GD, and MS were Cr-free. Three aliquots of K2 were doped with 0.5, 1.0, and 2.0 wt.% synthetic chromite ($FeCr_2O_4$) powder, made by mixing stoichiometric amounts of reagent-grade Fe_2O_3 and Cr_2O_3 under ethanol in an agate mortar and pestle. Table 2.1 describes the compositions of the starting materials.

Samples were prepared by mixing various proportions of komatiite and assimilant compositions with a polyvinyl alcohol “glue” to create a slurry and attaching it to a loop made of 0.010” diameter Pt wire. The loop was then left in a 100°C drying oven until the slurry had hardened.

2.1.2. Experiment Design

Experiments were conducted in two vertical tube gas mixing furnaces housed at the Dalhousie High Pressure and Temperature Geochemistry Laboratory. Temperatures ranged from 1192-1462ºC. Oxygen fugacities ranged from FMQ-1 to FMQ+1 and were controlled by mixtures of CO and CO_2. Temperature and fO_2 were measured by a Y-doped zirconia sensor and Pt-$Pt_{87}Rh_{13}$ thermocouple before and after each experiment. Experiments involved two steps, the first to pre-saturate the Pt wire in Fe to avoid Fe-loss during the second step, which was the solubility experiment. To pre-saturate the Pt wire, up to 3 samples were hung from a fused silica rod 4 mm in diameter that was lowered into the hot spot of the furnace and held there for 24 h, then quenched by plunging the samples into a beaker of cold water. The pre-saturated Pt loops were submerged in HF for 12 h to remove the residual sample, then fresh material was attached to the loops, which were then re-run at the same fO_2 for 48-96 h. Figure 2.1 shows an image of the sample configuration and the vertical tube gas mixing furnaces employed in experiments. Experiments were done by first retracting the silica rod so the samples were in the cool part of the furnace, which was then sealed. The samples were then lowered into the furnace hot spot and equilibrated for 48 h. Experiments were terminated by opening the bottom of the furnace and rapidly lowering the rod through the furnace and into a beaker of water placed below the bottom opening.

2.2 Analytical Methods

2.2.1 Electron Probe Micro-Analysis

Run products were mounted in epoxy and polished with 240 grit SiC, followed by 400 and 600 grit SiC, then 1 μm alumina, and finally 0.3 μm alumina. The major element composition of run products was determined using the JEOL JXA-8200 Electron Probe Micro-Analyzer (EPMA) housed in the Robert M. MacKay Electron Microprobe Lab at Dalhousie University. Silicate glass analyses were done using an accelerating voltage of 15kV, a beam current of 10 nA, and a 10 μm defocused beam to limit glass damage. Standards for silicate melt analysis were natural basalt (Si, Ca, Al, Fe, Mg, Na), pyrolusite (Mn), rutile (Ti), chromite (Cr), sanidine (K), and apatite (P). Count times were 20 seconds for major elements, and 40 seconds for Cr. Chromite analyses were done using an accelerating voltage of 15 kV, a beam current of 12 nA, and a 1 μm spot size. Chromite standards were chromite (Al, Fe, Mg, Cr), pyrolusite (Mn), rutile (Ti), kaersutite (Ca), and sanidine (Si). Count times on all elements were 20 seconds. Olivine analyses were done using an accelerating voltage of 15 kV, a beam current of 12 nA and a 1 μm spot size. Olivine standards were olivine (Fe, Mg, Si), sanidine (Al), chromite (Cr), pyrolusite (Mn), rutile (Ti), and kaersutite (Ca). For all analyses, raw count rates were converted to concentrations suing the ZAF data reduction scheme.

2.2.2 Laser Ablation Inductively Coupled Plasma Mass Spectrometry

Chromium concentrations in the silicate glass were determined using the Dalhousie laser ablation ICPMS facility located in the Health and Environments

Research Centre (HERC) Laboratory at Dalhousie University. The system employs a frequency quintupled Nd:YAG laser operating at 213 nm, coupled to a Thermo Scientific iCAP Q ICPMS quadrupole mass spectrometer with He flushing the ablation cell to enhance sensitivity (Eggins et al., 1998). Silicate glasses were analyzed using a laser repetition rate of 10 Hz, spot size of 20-50 μm, and laser output of ~8 J/cm^2. Factory-supplied time resolved software was utilized for the acquisition of individual analyses. A typical analysis involved 20 seconds of background acquisition with the ablation cell being flushed with He, followed by laser ablation for 60 seconds, then 60 seconds of cell washout. Analyses were collected in a sequence in which two analyses were done on a standard reference material (NIST610) at the start of the acquisition cycle, then after every 20 analyses on the unknowns. When possible, 3 to 5 analyses were done on each sample. Data reduction was done off-line using the Iolite version 3.6 software package. Cr concentrations in the silicate glass were quantified using the NIST610 silicate glass, which contains 405.2 ppm Cr (Pearce et al., 1997). Ablation yields were corrected by referencing to the known concentration of Ca as determined by EPMA. The ^{52}Cr and ^{53}Cr isotopes were measured as a check for interfering isobars.

2.2.3 External Standards

Two basalts from a suite of USGS reference materials, BHVO-1 and BIR-1, were used to test the accuracy of the EPMA and LA-ICPMS glass analyses. Glasses were prepared by fusing powders at 1400°C and 1 GPa for 30 minutes in high purity graphite. Analyses of the BHVO-1 and BIR-1 glasses were done in the same analytical sessions to measure glass unknowns. Table 2.2 summarizes the results, and indicates that measured

values agree within 1 standard deviation of the preferred values from Jochum et al. (2005).

CHAPTER 3: THE DALHOUSIE GAS-MIXING FURNACES

3.1 Design and Components of the 0.1 MPa Gas-mixing Furnace

The gas-mixing furnaces employed in this study are a vertical tube design manufactured by Deltech, Inc. (Denver, USA). The tubes are made from high-purity Al_2O_3, have an outer diameter of 31 cm, an inner diameter of 25 cm, and are approximately 75 cm long. High temperature in the furnaces is generated by six $MoSi_2$ heating elements arranged concentrically around the tube, with long axis parallel to the tube. Temperature is monitored by an internal Pt-$PtRh_{13}$ (type R) thermocouple touching the outside of the tube in the hotspot, which is connected to a Eurotherm 2404 power output controller. The temperature gradient and location of the hot spot in the furnaces are measured with a Pt-$PtRh_{10}$ (type S) thermocouple connected to a temperature display. The fO_2 is controlled by controlling the proportions of CO_2 and CO gases flowing through the furnace tube.

3.1.1 Furnace Flow Design

Figure 3.1 shows one of the furnaces. Each furnace has a dedicated pair of mass flow controllers (Aalborg Instruments & Controls, Inc. TlO Totalizer Input/Output Flow Monitor/Controller) calibrated for CO_2 and CO gases. Gases flow separately from the mass flow controllers, then join a single length of tubing approximately 1 m from the furnace entrance, which ensures sufficient mixing. Once mixed, the gas enters the furnace tube through the bottom and rises, exiting the tube at the top, which is then vented to outside the lab.

3.1.2 Y-doped Zirconia Sensor

The fO_2 inside the furnace was measured before and after experiment with a Y-doped zirconia sensor manufactured by Australian Oxytrol Solutions Ltd. The sensor measures fO_2 by generating an electric potential in response to the difference in oxygen concentration between the atmosphere in the furnace and a reference gas. The electric potential is generated due to the reaction:

$$O_2 + 4e^- = 2O^{2-}. \tag{3.1}$$

Figure 3.2 shows a schematic of this process. The electric potential generated by the sensor is related to the fO_2 of atmosphere in the furnace by the Nernst equation:

$$E = \frac{RT}{nF} ln(\frac{fO_2^x}{fO_2^{ref}}) \tag{3.2}$$

where E is the electric potential in mV, R is the gas constant, T is temperature in K, n is the number of charges per reactant species, F is the Faraday constant, fO_2^x is the oxygen fugacity of the atmosphere in the furnace, and fO_2^{ref} is the oxygen fugacity of the reference gas. If the reference gas is air, then the Nernst equation can be recast as:

$$log(fO_2) = log(0.209e^{-46.421E/T}), \tag{3.3}$$

in which fO_2 is expressed in the more conventional base-10 log.

3.2 Calibration of Thermocouple Accuracy

The accuracy of type R thermocouples used to measure temperature in the gas-mixing furnaces before and after experiments was determined by measuring the melting temperature of pure gold, which can be traced to the reference value of 1064ºC (O'Neil, 2001).

3.2.1 Experiment Design, Execution, and Results

The calibration was done by simultaneously measuring thermocouple temperature and the conductivity of an Au wire, with the temperature at the melting point defined by a rapid loss of conductivity corresponding to the melting of the wire. The experiment employed an alumina tube 6 mm in diameter with four holes 1.3 mm in diameter threaded with two thermocouples: one type S thermocouple connected by a bead at the bottom used during experiments ("experimental thermocouple") and one type S thermocouple connected at the bottom by an Au wire ("Au wire circuit"). This assembly (Figure 3.3) was inserted into the furnace at 1000ºC, the experimental thermocouple was connected to a temperature display, and the Au wire circuit was connected to a voltmeter to measure conductivity. The temperature of the furnace was then increased by 0.5ºC per minute until the Au wire circuit lost conductivity. The temperature recorded at that point was 1064°C, consistent with the accepted melting point of Au.

3.2.2 Accuracy of the Thermocouple

The results confirmed the accuracy of the type S thermocouple that is typically used to measure the furnace temperature, and this thermocouple was then used to calibrate the type R thermocouple used in the Y-doped zirconia sensor. This was accomplished by measuring the temperature at a fixed depth in the furnace with the type S and type R thermocouple subsequent to each other using the same output meter. The type R thermocouple reports temperatures that are 8ºC than the true value. This offset could be due to a small inaccuracy in the default voltage-to-temperature conversion in the temperature display output device.

3.3 Accuracy of the Y-doped Zirconia Sensor

The accuracy of the Y-doped zirconia sensor for measuring fO_2 was determined using the sliding sensor method described in Taylor et al. (1992). This method involves equilibrating NiO-MnO mixtures with pure Ni to form $Ni_xMn_{1-x}O$, in which x depends on fO_2. The composition of the resulting oxide can be measured after an experiment using EPMA, and the resulting fO_2 was calculated using equation 3.7, whose basis is outlined below.

3.3.1 Thermodynamic Basis

The (Ni,Mn)O redox sensor is based on the heterogeneous reaction:

$$\mathrm{Ni}_{(s)} + \frac{1}{2}\mathrm{O}_{2(g)} = \mathrm{NiO}_{(s)}. \tag{3.4}$$

The equilibrium constant for this reaction can be written as

$$\mathrm{K}_{eq} = \frac{a_{\mathrm{NiO}}}{a_{\mathrm{Ni}}(f\mathrm{O}_2)^2}, \tag{3.5}$$

where a_{NiO} is the activity of NiO in the oxide phase, and a_{Ni} is the activity of Ni in the metal phase. If Ni and NiO are pure phases, then their respective activities are equal to unity, and the equation for K_{eq} can be rewritten as

$$log(\mathrm{K}_{eq}) = -\frac{1}{2}log(f\mathrm{O}_2). \tag{3.6}$$

If the NiO component is diluted with another metal oxide such as MnO, a_{NiO} becomes less than 1, and the effect on fO_2 can be calculated using:

$$log(f\mathrm{O}_2) = -2[log(\mathrm{K}_{eq}) - log(a_{\mathrm{NiO}})]. \tag{3.7}$$

From these relations, when fO_2 is fixed such as in a gas-mixing furnace, the sample material adjusts its composition to achieve equilibrium with the ambient atmosphere. Therefore, the composition of the resulting oxide phase $Ni_xMn_{1-x}O$ depends on the fO_2 of the furnace.

Taylor et al. (1992) compiled data for binary oxide and alloy system activity coefficients and fit them to a Redlich-Kister polynomial form. Substituting the relevant Redlich-Kister polynomial into Equation 3.4, Taylor et al. (1992) derived Equation 3.7 relating the composition of the oxide to fO_2:

$$log(f\mathrm{O}_2)_{(\mathrm{Ni,Mn})\mathrm{O}} = 2log(X_{\mathrm{NiO}}) - \frac{1}{2.303RT}(480104 - 244.700T + 21.1078Tlog(T) - [2(1 - X_{\mathrm{NiO}})^2(9731 + 2.388T)]), \tag{3.8}$$

where X_{NiO} is the molar proportion of NiO in the oxide phase, R is the gas constant, and T is the temperature in K.

3.3.2 Experiment Design and Execution

Calibration experiments were done at 1192ºC and $\log fO_2 = -8.34$ (FMQ+0.16). Two sets of two capsules were prepared, one with powders of MnO_2 and an excess of Ni, and the other with powders of MnO_2 and an excess of NiO. The purpose of the two experiments is to approach equilibrium of the oxide phase by oxidation of Ni as well as reduction of NiO. The powder mixtures were cold pressed into open ended, thick-walled silica tubes which were then attached with Pt wire to the hooked end of a fused silica rod, which was used to suspend samples in the furnace hot spot (Figure 3.4). Experiments were done by first retracting the silica rod so the samples were in the cool part of the furnace, which was then sealed, and the samples were then lowered into the furnace hot spot and equilibrated for 48 h. Experiments were terminated by opening the bottom of the furnace and rapidly lowering the rod through the furnace and into a beaker of water placed below the bottom opening. Before and after each experiment the fO_2 was measured and recorded with the Y-doped zirconia sensor, which was equilibrated for at least one hour to achieve a stable reading. After experiments, samples were removed from the silica tube, mounted in epoxy, then ground and polished for EPMA. Oxide analyses were done using a 15 kV accelerating voltage, 20 nA current, and 1 μm spot size. Standards for oxide analysis were pyrolusite (Mn) and pentlandite (Ni).

3.3.3 Results

Table 3.1 provides a summary of experiments, with resulting oxide phase composition, calculated X_{NiO} and $\log fO_2$ from Equation 3.7, as well as values measured from the Y-doped zirconia sensor. At conditions near the FMQ buffer measured by the Y-doped zirconia sensor (1192ºC and $logfO_2 = 8.34$), the fO_2 calculated by the oxide phase composition is between -8.34 and -8.36. The maximum error reported for the (Ni,Mn)O sensor by Taylor et al. (1992) was 0.14 log units. These results indicate that the Y-doped zirconia sensor used to measure fO_2 of experiments is accurate to within 0.02 log units.

CHAPTER 4: RESULTS

4.1 Attainment of Equilibrium

To ensure that 48 hours is sufficient to achieve equilibrium, experiments at the lowest temperature investigated (1192°C) were duplicated with 24 h and 96 h run durations, and the melt compositions were compared in terms of FeO and Cr concentrations (Figure 4.1.1). These two parameters were chosen to evaluate equilibrium because Fe can be lost to the Pt loop, and results show that wt.% FeO is the melt composition parameter that exerts the most influence on the CCCS. Five sets of time series experiments on the following compositions were compared: komatiite (K1), 20 wt.% BIF, 50 wt.% BIF, 5 wt.% GD, and 10 wt.% GD (Figure 4.1.1). In terms of wt.% FeO, all sets agreed within 1 standard deviation except K1. In the K1 set, there was no systematic change in wt.% FeO with increasing duration. In terms of Cr, all sets except K1 and 50 wt.% BIF agreed within 1 standard deviation. Between K1 and 50 wt.% BIF there is no systematic change in Cr concentration content with change in duration, as the 96 h K1 run had higher Cr than the 48 h run, whereas the 96 h 50 wt.% BIF run had lower Cr than the 48 h run. The absence of systematic change in glass composition with increased run duration, and the overall reproducibility of results, suggests that samples run at 1192ºC or higher had reached equilibrium within 48 h.

Another metric for equilibrium is consistent major element partitioning between chromite and melt. In their reversed experiments, Roeder and Reynolds (1991) showed that chromite-melt Fe-Mg partitioning is constant, with $Fe\#^{chr}/Fe\#^{melt}$ of 1.18±0.05, independent of temperature and melt composition. Experiments by Murck and Campbell (1986), which also include reversals, have $Fe\#^{chr}/Fe\#^{melt}$ of 1.05±0.04. The Fe# was

calculated using the Fe^{2+} content of the melt determined using the calibration of Kress and Carmichael (1991) and the Fe^{2+} content of chromite from mineral stoichiometry after the method of Barnes and Roeder (2001). Parkinson & Arculus (1999) have shown that the uncertainties associated with Fe speciation in chromite determined by stoichiometry are small for spinels with Fe^{3+}/total Fe >0.4, which is the case for experiments in this study. Experiments from this study display $Fe\#^{chr}/Fe\#^{melt}$ of 0.98±0.06, respectively, thus consistent with Murck and Campbell (1986) but not with Roeder and Reynolds (1991). One difference between the datasets is that the oxide totals of EPMA analyses by Roeder and Reynolds (1991) are consistently lower (<98.5 wt.%) than those from Murck and Campbell (1986) and this study (>98.5 wt.%), which could affect the $Fe\#^{melt}$ calculation.

Another test for equilibrium is homogeneity within run products. This was assessed by monitoring the LA-ICPMS analyses of spots across the diameter of the sample bead. Figure 4.1.3 shows that there is no systematic change in Cr content of glass with increased distance from the edge of the sample, attesting to glass homogeneity. In terms of chromite compositions, the average relative standard deviation for major elements is 2.89%.

4.2 Textural Observations

Most experiments produced sub- to euhedral chromite and olivine with all bulk compositions. Runs at 1192°C produced chromite < 5 μm in diameter, olivine 2-40 μm in diameter, and occasionally, euhedral anorthite oikocrysts up to 150 μm long (Figure B1). Crystals were dispersed evenly across experiments done at this temperature. Runs

at 1292°C produced chromite < 10 μm in diameter and olivine 5-50 μm in diameter; crystals were also dispersed evenly (Figure B2). Runs at 1392°C produced chromite < 10 um in diameter and olivine < 10 μm in diameter. Crystals were evenly dispersed across 1392ºC samples except for runs with high amounts of Fe, where samples had a cumulate texture (Figure B3). Runs done above 1400°C produced chromite < 20 μm in diameter and olivine 10-100 μm in diameter (Figure B4). These high-temperature samples had cumulate textures and minor quench textures within the crystal piles. Occasionally, high-temperature experiments also had clinopyroxene crystals ~20 μm in diameter around the edge of the sample, interpreted as a quench product. In all run products, some olivine crystals contained chromite inclusions. Runs containing natural magnetite had more complex textures: a relict core of magnetite that was rimmed by a magnetite-glass symplectite replacing the original magnetite cube, in turn surrounded by glass with a quench texture containing skeletal magnetite (Figure B5).

4.3 Chromium Content at Chromite Saturation (CCCS)

Table 4.3 summarizes the compositions of melt in equilibrium with chromite. Proportions of Fe^{2+} and Fe^{3+} were calculated using the method of Kress and Carmichael (1991). The dataset has been filtered using mass balance to exclude run products that lost Fe to the Pt loops by summing the FeO contents of all phases and excluding any samples whose sum is less than the starting FeO content.

4.3.1 Effect of Temperature and fO_2

The CCCS of uncontaminated komatiite at the FMQ oxygen buffer increased with increasing temperature, from 262 ppm Cr at 1192ºC to 2296 ppm Cr at 1462ºC. Figure 4.3.1 provides a summary of the variation in CCCS with 1/T for experiments from this study, Murck and Campbell (1986), Roeder and Reynolds (1991), and Brenan et al. (2012). All of the data define a coherent trend of decreasing CCCS with 1/T, with results from this study consistent with previous work. The CCCS dependence on 1/T in komatiites can be described by the relationship

$$log(\mathrm{CCCS}) = -0.853(\pm 0.055) * \frac{10^4}{\mathrm{T(K)}} + 8.40(\pm 0.33) \quad (4.1)$$

in which CCCS is in ppm and T is in K, obtained by linear regression (Fig. 4.3.1).

It was also found that the CCCS of uncontaminated komatiite decreased with increasing fO_2; at 1292ºC CCCS decreased from 1002 ppm Cr at the FMQ oxygen buffer to 871 ppm Cr at FMQ + 1, and at 1392ºC CCCS decreased from 1758 ppm Cr at the FMQ oxygen buffer to 1679 ppm Cr at FMQ + 1. Figure 4.3.2 summarizes the variation in CCCS with fO_2 from this study and Murck and Campbell (1986). Previous experiments on mostly basaltic compositions (Roeder and Reynolds, 1991; Murck and Campbell, 1986) show that the effect of fO_2 on CCCS diminishes as fO_2 increases above the FMQ buffer, which agrees well with data from this study. Figures 4.3.1 and 4.3.2 show that the data from this study are shifted to lower chromite solubilities for a given temperature or fO_2 compared to data from Murck and Campbell (1986). This offset is likely due to the higher FeO content of komatiite used in this study (12.21 wt.% FeO)

compared to the komatiite composition used in their study (10.44 wt.% FeO). As will be shown in the next section, at constant temperature and fO_2, the FeO content of the melt is the most important compositional parameter that affects CCCS.

4.3.2 Effect of Melt Composition

Figures 4.3.3, 4.3.4, and 4.3.5 summarize the effects of varying degrees of contamination by banded iron formation (BIF), granodiorite (GD), and metasediment (MS) respectively, on CCCS. CCCS was found to decrease with increasing BIF content, and increase with increasing GD content. Addition of MS did not result in any systematic change in CCCS. The compositional effect of GD on CCCS diminished at high temperatures, agreeing with previous findings (Murck and Campbell, 1986), but the compositional effect of BIF on CCCS persisted to the highest temperature investigated in which the melt was still saturated in chromite (1422ºC).

Following a systematic evaluation of melt composition parameters (e.g., wt.% oxides, NBO/T, optical basicity), the strongest correlation with CCCS is with the FeO content of the melt. This relation is portrayed in Figure 4.3.6, and clearly shows that CCCS decreases with increasing FeO. This is consistent with addition of BIF and GD having opposite effects on CCCS, as BIF contains more FeO than the komatiite, whereas GD contains less. The MS composition used in this study has a similar FeO content to the komatiite, such that assimilation of MS does not cause a significant change in FeO and therefore an undetectable effect on CCCS, but other metasedimentary compositions could have different results based on their FeO content.

4.4 Phase Equilibria

Figure 4.4.1 shows the effect of increased melt FeO, through the addition of BIF, on komatiite phase equilibria. The dataset consists of all experiments containing BIF, including those with komatiite doped with additional chromite. The liquidus temperature of uncontaminated komatiite could not be determined experimentally as it exceeds the temperature for which the furnace is rated. However, a minimum olivine-in temperature of ~1500ºC can be estimated from the results of Murck and Campbell (1986) done using a similar melt composition. Experiments did not distinguish the liquidus phase for experiments using komatiitic starting material with 2187 ppm Cr. The olivine-in temperature decreased with increasing FeO, from ~1475ºC at 12.21 wt.% FeO to ~1375ºC at 15.55 wt.% FeO. The olivine-in temperature calculated by the MELTS thermodynamic model is also shown in Figure 4.4.1 for comparison. The slope of the calculated olivine-in line is similar to the line inferred from experiments, however the calculated line is offset to temperatures ~50ºC higher than the inferred line.

4.5 Chromite Chemistry

Figure 4.5.1 portrays Cr# vs. Fe# for experimental chromites. Cr# increases and Fe# decreases with increasing temperature, and there is no systematic effect of changing melt composition on chromite chemistry. The Cr# of chromites produced in experiments that did not contain added magnetite, equilibrated at or above 1392ºC, is 0.60-0.67, within the range of Cr# from ROFIS chromite (0.56-0.73), however the Fe# of the same

experimental chromites is 0.16-0.25, which is much lower than that of ROFIS chromite (0.40-0.88). The cause of the shift to low Fe# in high temperature experiments is discussed in section 5.2. Experiments that contained 5-10 wt.% synthetic magnetite at 1392ªC had slightly higher Fe# (0.28-0.29) and lower Cr# (0.51-0.53), and experiments that contained 5-10 wt.% natural magnetite had even higher Fe# (~0.38) and more variable Cr# (0.42-0.61), but neither series of experiments with magnetite overlaps the Fe# of ROFIS chromite. The only Fe# overlap between experiments with natural magnetite and ROFIS chromite corresponds to the residual magnetite core, which does not reflect a high temperature equilibrium composition.

4.6 Olivine Chemistry

Table 4.6 summarizes the composition of olivine produced in experiments. The forsterite component of the olivine (Fo_n) ranged from 60 to 82, and generally increased with increasing temperature and decreasing Fe content of the melt. Olivine contained between 0.07 and 0.29 wt.% Cr_2O_3, generally increasing with increasing Fo_n.

5.0 DISCUSSION

5.1 Origin of the Variation in CCCS with Melt Composition

Experiments show that the CCCS is inversely correlated with FeO in the melt, and in this section a model that describes this behaviour is explored in the context of the equilibrium constant for chromite dissolution. Results are then used to predict chromite solubility in previous experimental studies, and to assess the role of contamination in the formation of chromitites.

5.1.1 Thermodynamic Basis

The reaction that is the basis of this model describes the dissolution of chromite in silicate melt:

$$\mathrm{FeCr_2O_4^{sp}} = \mathrm{FeCr_2O_4^{melt}} \tag{5.1}$$

in which the subscripts sp and melt refer to the chromite component in spinel and silicate melt, respectively. The equilibrium constant, K_{eq}, for this reaction can be written as:

$$\mathrm{K}_{eq} = \frac{a^{melt}_{FeCr_2O_4}}{a^{sp}_{FeCr_2O_4}} \tag{5.2}$$

in which *a* refers to the activity of the chromite component in the melt and spinel phase. At equilibrium,

$$\Delta \mathrm{G}^{\circ} = -\mathrm{RT}ln(\mathrm{K}_{eq}), \tag{5.3}$$

in which ΔG^o is the change in standard state Gibbs free energy, R is the gas constant, and T is temperature in K. ΔG^o can also be described by the equation:

$$\Delta G^o = \Delta H^o - T\Delta S^o, \tag{5.4}$$

in which ΔH^o and ΔS^o are the change in standard state enthalpy and entropy, respectively. Substituting Equation 5.2 for K_{eq} and Equation 5.4 for ΔG^o into Equation 5.3 yields:

$$ln\left(\frac{a^{melt}_{FeCr_2O_4}}{a^{sp}_{FeCr_2O_4}}\right) = \frac{\Delta H^o}{R}\left(\frac{1}{T}\right) - \frac{\Delta S^o}{R}. \tag{5.5}$$

The chromite components are assumed to be dissolved in the melt according to the homogeneous equilibrium:

$$FeCr_2O_4^{melt} = FeO^{melt} + 2CrO_{1.5}^{melt}. \tag{5.6}$$

Hence, to calculate the activity of chromite in the melt, the activity coefficients for the FeO and $CrO_{1.5}$ species are required. Holzheid et al. (1997) determined that the activity of FeO in silicate melts with MgO contents from 7–27.5 wt.%, between 1300-1600°C and FMQ-1.7 to FMQ-5.7, is approximately 1.7 ± 0.22. Berry et al. (2006) showed that the activity coefficient of $CrO_{1.5}$ in silicate melt is negatively correlated with optical basicity (Eqn 5.9) but becomes a constant value of ~0.015 in ultramafic melts. The activity of chromite in spinel can be calculated following Murck and Campbell (1986), assuming a single-site mixing model in which all FeO and Cr_2O_3 occur in tetrahedral and octahedral sites in the spinel, respectively. Equation 5.5 can therefore be rewritten as:

$$ln\left(\frac{1.7(X^{melt}_{FeO}) * \gamma^{melt}_{CrO_{1.5}}(X^{melt}_{CrO_{1.5}})^2}{Fe\#^{sp} * (Cr/3+^{sp})^2}\right) = \frac{\Delta H^o}{R}\left(\frac{1}{T}\right) - \frac{\Delta S^o}{R}, \tag{5.7}$$

in which X is molar proportion, γ is the activity coefficient, in this case of $CrO_{1.5}$ in silicate melt, $Fe\#^{sp}$ is $Fe^{2+}/(Mg+Fe^{2+})$ (mol.%) of spinel and $Cr/3+^{sp}$ is $Cr/(Cr+Al+Fe^{3+})$ (mol.%) of spinel. A fixed value for $\gamma^{melt}_{CrO1.5}$ of 0.015 is assumed for komatiitic melts, whereas values for basaltic compositions can be determined by the relation:

$$\gamma^{melt}_{CrO_{1.5}} = -0.2942(\mathrm{OB}) + 0.1808 \tag{5.8}$$

in which OB is the optical basicity, defined as:

$$\mathrm{OB} = 0.48(\mathrm{X}_{SiO_2}) + 0.45(\mathrm{X}_{Al_2O_3}) + 0.69(\mathrm{X}_{MgO}) + 1.0(\mathrm{X}_{CaO}), \tag{5.9}$$

which is a simplification of the definition of theoretical optical basicity, as defined by Duffy (1993), used by Berry et al. (2006) for synthetic melt compositions that are comprised of only SiO_2, Al_2O_3, MgO, and CaO. For the purposes of this study, OB was calculated by normalizing the molar proportions of SiO_2, Al_2O_3, MgO, and CaO in experimental melts to 1.

Using the CCCS data from this study, values of ΔH^o and ΔS^o can be determined by plotting ln K_{eq} vs. 1/T, which should yield a straight line of slope $\Delta H^o/R$ and intercept $-\Delta^oS/R$, provided both ΔH^o and ΔS^o are independent of temperature (i.e., $\Delta C_p = 0$). A linear relation is confirmed by the data from this study (Fig. 5.1), and regression of Equation 5.7 yields $\Delta H^o/R$ of 3.5347±0.1211 and $\Delta S^o/R$ of 1.33±0.75. Equation 5.7 can therefore be rearranged as:

$$ln(\mathrm{X}^{melt}_{CrO_{1.5}}) = \frac{1}{2}[-3.5347\left(\frac{10^4}{\mathrm{T}}\right) + 1.33 - [\mathrm{Fe}\#^{sp} * (\mathrm{Cr}/3+^{sp})^2] - ln[1.7(\mathrm{X}^{melt}_{FeO})] - 2ln(\gamma^{melt}_{CrO_{1.5}})] \tag{5.10}$$

which describes the compositional dependence of the CCCS as arising due to contributions from variations in spinel composition and $\gamma_{CrO1.5}$. Importantly, equation 5.10 also provides the thermodynamic basis for the control of melt composition on CCCS, with increases in the melt FeO content and decreases in OB resulting in a lowering of the CCCS. Isolating the effect of melt OB or FeO content is challenging in this context because assimilation of an FeO-rich country rock alters both parameters, and $\gamma_{CrO1.5}$ has not been determined for FeO-containing melts. Figure 5.2 shows the relationship between Cr in the melt and OB for theoretical melts with fixed FeO contents at 1400°C and the FMQ oxygen buffer. At OB<0.57, corresponding to basaltic (<12 wt.% MgO) and picritic (12-18 wt.% MgO) compositions, increases in OB lower CCCS, whereas at OB>0.57, corresponding to komatiitic (>18 wt.% MgO) compositions, changes in OB do not alter CCCS. This is a result of $\gamma_{CrO1.5}$ becoming constant at high OB. Therefore, OB is an important parameter for modelling CCCS in basaltic and picritic compositions, but is not necessary for modelling CCCS in komatiites.

Equation 5.10 does not take into account the effect of pressure on CCCS. This could be accomplished by including the pressure term in Equation 5.4 and including experiments at high pressure to calibrate the model, which was beyond the scope of this study.

5.1.2 Application to Other Datasets

Figure 5.3 shows the results of using Equation 5.10 to predict the chromite solubility data of Murck and Campbell (1986) and Roeder and Reynolds (1991). For

experiments done at FMQ, the values for the FeO content of the melt, OB, and chromite composition were substituted into Equation 5.10 and the modelled and measured CCCS compared. The average absolute magnitude of the difference between the model output and the measured value of $X_{CrO1.5}$ for experiments done at T > 1350ºC is 5.8% relative. Equation 5.10 can therefore be used to model the CCCS in mafic and ultramafic melts at the FMQ buffer and high temperature. In the context of forming monomineralic chromitites by assimilation or magma mixing, the solubility model developed here can be used to explore the effect of changing melt composition (notably the FeO content and optical basicity) to induce chromite saturation, and as well to determine the amount of chromite that can be formed from an unadulterated magma during cooling. Both of these aspects are explored in the context of the ROFIS in the next section.

5.2 Origin of the Variation in the Black Thor Chromite Compositions

Figure 1.3.4 shows that chromites from the Black Thor and Blackbird deposits do not follow the Fe-Ti trend nor the Cr-Al magmatic trends described by Barnes and Roeder (2001). The Fe-Ti and Cr-Al trends reflect changes in the melt composition due to fractional crystallization. The Cr-Al trend is the positive correlation between Fe# and Cr#, which reflects increases in Cr and Fe contents of the melt, as well as decreases in Al and Mg, due to fractional crystallization of olivine and plagioclase (Barnes and Roeder, 2001; Roeder and Reynolds, 1991). The Fe-Ti trend is the positive correlation between Fe^{3+} and Fe# with TiO_2, and reflects increases in the Fe:Mg ratio and Ti content of the melt due to fractional crystallization of olivine. Whereas the range in Cr# for the Black Thor and Blackbird chromitites is similar to that produced in the highest temperature

experiments, all experimental chromites are too poor in FeO compared to the natural samples. It seems clear from the results of fO_2-T estimates of the Black Thor chromitites using olivine-spinel oxybarometry (section 1.3.4) that both the Black Thor and Blackbird chromites represent subsolidus re-equilibration with olivine, a Fe-Mg exchange reservoir, which might explain the shift in Fe# relative to the high temperature experimental chromites seen in Figure 4.5.1. The similarity in Cr# between the Black Thor chromite and the highest temperature (i.e., 1392ºC and above) experimental chromites is consistent with the overall lack of any exchange reservoir for trivalent cations in the natural chromitites, thus preserving the magmatic Cr#, despite subsequent cooling.

The re-equilibration hypothesis to explain the range in Fe# for Black Thor chromitites is tested by calculating the expected chromite composition at different temperatures using the olivine-spinel thermometer (O'Neill and Wall, 1987). This approach assumes that the Cr# of chromite does not change during subsolidus re-equilibration with coexisting silicate phases, and that partitioning of Fe^{2+} and Mg between olivine and orthopyroxene is close to unity (von Seckendorff and O'Neill, 1993). The latter assumption is required so that olivine and orthopyroxene can be considered together as one silicate crystalline Fe^{2+}-Mg reservoir when determining the mass fractions of spinel and silicate crystalline phase, which will be referred to as olivine* for the purposes of this study. The mass fractions must be known so that mass balance of Fe^{2+} and Mg is conserved during recalculation of Fe# at high temperature.

Mass fractions of spinel and olivine* can be determined by the equation

$$\mathrm{Fe}\#^{bulk} = \mathrm{Fe}\#^{sp}\mathrm{X}^{sp} + \mathrm{Fe}\#^{ol*}\mathrm{X}^{ol} \quad (5.11)$$

in which $Fe\#^{bulk}$, $Fe\#^{sp}$, and $Fe\#^{ol*}$ indicate the Fe# of the bulk rock, spinel, and olivine*, respectively, and X^{sp} and X^{ol*} indicate the mass fraction of spinel and olivine*. The sum of X^{sp} and X^{ol*} is assumed to equal 1, so X^{ol*} can be replaced by $1-X^{sp}$ in equation 5.11, and the equation can be solved for X^{sp}:

$$X^{sp} = \frac{Fe\#^{ol*} - Fe\#^{bulk}}{Fe\#^{ol*} - Fe\#^{sp}} \quad (5.12)$$

Once the mass fractions of spinel and olivine* are known, equation 5.11 can be rearranged to calculate how $Fe\#^{sp}$ and $Fe\#^{ol*}$ must vary together to conserve mass:

$$Fe\#^{ol*} = \frac{Fe\#^{bulk} - Fe\#^{sp}X^{sp}}{X^{ol*}} \quad (5.13)$$

Equation 5.13 can then be substituted for $Fe\#^{ol}$ in the O'Neill and Wall (1987) olivine-spinel thermometer which can be solved iteratively by varying $Fe\#^{sp}$ to reach the desired temperature. To calculate the primary Fe# of chromite from the Black Thor deposit, a representative chromite sample with Fe# 0.82 was chosen for which the Fe# of its olivine pair used for oxygen barometry (section 1.3.4) was 0.13, and the $Fe\#^{bulk}$ was estimated to be 0.14 based on whole rock chemistry from the Blackbird deposit (Azar 2010; sample ID 1G65 258) and Fe^{3+}/Fe^{2+} calculated using the method of Kress and Carmichael (1991) at T = 1400ºC and the FMQ oxygen buffer. The average estimated X^{sp} of the Black Thor samples based on Equation 5.12 is 0.14. Compositions were estimated for two scenarios: one in which $X^{sp} = 0.1$, and another in which $X^{sp} = 0.5$. Results of calculating the $Fe\#^{sp}$ of the representative Black Thor chromite at 1400ºC, 1200ºC, 1000ºC, and 800ºC are shown on Figure 5.4, and compared with the measured composition of chromites from the Black Thor deposit, as well as high-temperature (>1392ºC) experimental chromites

from this study. When X^{sp} is low ($X^{sp} = 0.1$), the magnitude of the change in chromite Fe# with increasing temperature is greater than when X^{sp} is high ($X^{sp} = 0.5$). The calculated Fe# of Black Thor chromite at 800ºC, 1000ºC, 1200ºC, and 1400ºC is 0.47, 0.38, 0.32, and 0.26 respectively when $X^{sp} = 0.1$, and is 0.23, 0.22, 0.21, and 0.20 respectively when $X^{sp} = 0.5$. The low-temperature end of the $X^{sp} = 0.1$ range (0.47), which is more applicable to the Black Thor chromite with average X^{sp} ~0.14, overlaps with the Black Thor Fe# (0.46-0.68) and the high-temperature end (0.26) approaches the Fe# of experimental chromite (0.16-0.25), supporting the hypothesis that the range of measured Fe# is due to subsolidus Fe-Mg exchange between chromite and coexisting silicate phases.

The Blackbird chromite dataset lacks the requisite olivine pairs for fO_2 estimation and therefore high-temperature modeling, however the likeness to the Black Thor chromite compositions in terms of clustered Cr# and spread of Fe# indicates that the modeled high-temperature chromite compositions for the Black Thor are likely applicable to the Blackbird chromites as well.

5.3 The Role of Contamination in the Formation of ROFIS Chromitites

Experimental results of this study on the effect of assimilation of Fe-rich rock on CCCS (Fig. 4.3.6) and phase equilibria (Fig. 4.4.1) can be combined and used to predict whether chromite or olivine will be the liquidus phase for a komatiitic melt with a given Cr and FeO content at the FMQ oxygen buffer. This can be done by calculating the CCCS as a function of T for komatiite with fixed FeO content using the model developed

in section 5.1, while at the same time monitoring the olivine-in temperature. Figure 5.5 shows the results of calculations for melts with 10, 12, and 14 wt.% FeO. The crystallization path for an uncontaminated komatiite parental to the ROFIS was modelled by assuming a melt similar to the parental melt composition of Azar (2010) with 12 wt.% FeO. Although the initial Cr content of this parental melt is unknown, a plausible maximum value can be estimated from the correlation between Cr and MgO for the global komatiite database published by Barnes (1998, his Figures 3 and 4). Although there is considerable scatter in the data, the compilation shows that due to differentiation, Cr increases with decreasing MgO to a maximum of ~3000 ppm, interpreted to be the point of chromite saturation and regarded as an upper bound for Cr contents of primitive mantle-derived magmas. A magma with this Cr content cooling from above the liquidus would follow the green dashed line in Fig. 5.4 to point A, and begin to crystallize olivine at 1484ºC. There is no chromite-only crystallization interval in this uncontaminated komatiite scenario because a modeled melt with 12 wt.% FeO and 3000 ppm Cr saturates in chromite at 1472ºC, which is 12ºC cooler than the olivine saturation temperature.

Based on whole rock LREE data from the ROFIS, the magma parental to the ROFIS could have assimilated between 15-44 wt.% country rock. The low end of this estimate corresponds to a scenario in which a komatiite with a flat REE pattern, reflecting concentrations ~5 times higher than chrondrite, assimilates BIF, the country rock with the highest concentration of LREES (Figure 5.5). The high end of this estimate corresponds to a scenario in which a komatiite with a slightly depleted LREE pattern, reflecting concentrations ~3 times higher than chondrite, assimilates metasediment, the country rock with the lowest LREE concentrations. Assimilation of 16 wt.% Cr-free BIF by the

ROFIS parental komatiite would increase the magma FeO content from 12 wt.% to 14 wt.% with a subsequent dilution in Cr content from 3000 to 2520 ppm. Under these conditions, a magma with 2520 ppm Cr cooling from above the liquidus would follow the red dashed line in Fig. 5.3 to point B, and begin to crystallize chromite at 1455ºC. Magma evolution along an FeO isopleth is reasonable because chromite crystallization in geologically relevant amounts will have a negligible effect on melt FeO content. The Cr content of the magma would evolve during cooling along the red dashed line to point C, which is the intersection of the 14 wt.% FeO CCCS curve and the olivine-chromite cotectic, at 1421ºC, at which point olivine would begin to form. After the onset of olivine crystallization, the FeO content of the melt would begin to increase and therefore deviate from the CCCS curve. This would lead to an increase in the amount of chromite crystallized because CCCS decreases with increasing melt FeO. The total chromite-only crystallization interval is 34ºC, with an accompanying change in Cr content of 471 ppm. Using the estimated primary composition of ROFIS chromite, 4500 kg/m^3 as the density of chromite (Marteev and Ballhaus, 2002) and ~3000 kg/m^3 as the density of komatiite (Arndt, 1983), this interval of chromite-only crystallization would produce a layer of chromite ~1.43 cm thick per 1 m column of komatiite, despite the Cr-dilution by the assimilant. Azar (2010) used MELTS to model chromite solubility and found that a column of magma of the composition thought to be parental to the ROFIS would have to be 1.2-4.7 km thick to crystallize only 1 m of chromitite. The results of this study show a column of komatiitic melt 1.2-4.7 km thick that assimilated 16 wt.% BIF would produce a layer of chromite approximately 17.16 to 67.21 m thick before the onset of olivine crystallization. In an open system, such as a magma conduit, continuous replenishment

of Cr by fresh magma could potentially cause a greater amount of chromite to crystallize before olivine saturation.

Another notable feature of Figure 5.5 is the absence of curvature of the olivine-chromite cotectic. If the line were convex, a mixing line between a primitive, FeO-poor melt and an evolved, FeO-rich melt would lie in the olivine-unsaturated field, indicating that magma mixing could cause chromite-only crystallization. The absence of curvature in the olivine-chromite cotectic indicates that mixing of a primitive and evolved melt would not result in chromite-only crystallization, and therefore does not support the model in which mixing of primitive and evolved members of the same magma series would lead to chromite-only crystallization (Irvine, 1977).

The possibility of contamination by FeO-rich country rocks contributing to chromitite formation is not limited to the ROFIS. For example, the Bushveld Complex was emplaced into the Transvaal Supergroup, within which is the Penge formation of the Chuniespoort Group, which is a 640 m thick BIF sequence with minor carbonate interbeds (Eriksson and Reczko, 1995). BIFs up to 150 m thick have also been observed in the contact aureole surrounding the Stillwater Complex in Montana (Page, 1977). The Great Dyke in Zimbabwe intruded the Tokwe terrane, which contains numerous greenstone belts that contain BIFs, including the Bubwa, Mweza, Matsitama, and Belingwe belts (Kusky, 1998). Lastly, the Sukinda Valley chromite deposits in India were emplaced into the Iron Ore Supergroup, which is comprised of cherty quartzite and BIF (Chakraborty and Chakraborty, 1984). In addition, increased chromite crystallization via contamination by FeO-rich country rock is compatible with other mechanisms for significant chromite accumulation, and in fact may be synergistic. Other

processes, such as gravitational settling or mechanical sorting are likely to play a role in the emplacement of stratiform chromitites.

Although it is plausible that contamination by FeO-rich country rock may have contributed to chromitite formation in the ROFIS, the results of this study show that the addition of different contaminant compositions does not drastically alter the major element chemistry of coexisting chromite (e.g., Figure 4.5.1). It is therefore not possible to identify the paragenesis of the contaminant based on the major element chemistry of chromite alone. However, trace element analyses of chromite could help verify the contaminant composition, as potential assimilant types may have anomalous concentrations of certain trace elements relative to typical komatiites, whose signature would be transferred to the crystallizing chromite.

REFERENCES

Arth, J.G., Arndt, N.T., and Naldrett, A.J. 1977. Genesis of Archean komatiites from Munro Township, Ontario: Trace-element evidence. Geology, **5:** 590-594.

Arndt, N.T. 1983. Role of a thin, komatiite-rich oceanic crust in the Archean plate-tectonic process. Geology, **11:** 372-375.

Aubut, A. 2015. Black Thor, Black Label, and Big Daddy chromite deposits, McFaulds lake Area, Ontario, Canada. National Instrument 43-101 Technical Report prepared for Noront Resources Ltd.

Azar, B. 2010. The Blackbird Chromite deposit, James Bay Lowlands of Ontario, Canada: Implications for chromitite genesis in ultramafic conduits and open magmatic systems. MSc thesis, Department of Geology, University of Toronto, Toronto, Ontario.

Barnes, S.J. 1998. Chromite in komatiites 1., Controls on crystallization and composition. Journal of Petrology, **39:** 1689-1720.

Barnes, S.J., and Roeder, P.L. 2001. The range of spinel compositions in terrestrial mafic and ultramafic rocks. Journal of Petrology, **42:** 2279-2302.

Ballhaus, C., Berry, R.F., and Green, D.H. 1991. High pressure experimental calibration of the olivine-orthopyroxene-spinel oxygen geobarometer: implications for the oxidation state of the upper mantle. Contributions to Mineralogy and Petrology, **107:** 27-40.

Berry, A.J., O'Neill, Hugh St.C., Scott, D.R., Foram, G.J., Shelley, J.M.G. The effect of composition on Cr^{2+}/Cr^{3+} in silicate melts. American Mineralogist, **91:** 1901-1908.

Brenan, J.M., Finnigan, C.F., McDonough, W.F., and Homolova, V. 2012. Experimental constraints on the partitioning of Ru, Rh, Ir, Pt and Pd between chromite and silicate melt: The importance of ferric iron. Chemical Geology, **302:** 16-32.

Cameron, E.N. 1980. Evolution of the Lower Critical Zone, Central Sector, Eastern Bushveld Complex, and Its Chromite Deposits. Economic Geology, **75:** 845-871.

Cameron, E.N. 1982. The Upper Critical Zone of the Eastern Bushveld Complex—Precursor of the Merensky Reef. Economic Geology, **77:** 1307-1327.

Cameron, E.N., and Desborough, G.A. 1969. Occurrence and characteristics of chromite deposits—eastern Bushveld Complex. Economic Geology Monograph, **4:** 23-40.

Carmichael, I.S.E. 1981. The redox states of basic and silicic magmas: a reflection of their source regions? Contributions to Mineralogy and Petrology, **126:** 129-141.

Carson, H.J.E., Lesher, M., and Houle, M.G. 2015. Geochemistry and petrogenesis of the Black Thor intrusive complex and associated chromite mineralization, McFaulds Lake greenstone belt, Ontario. *In* Targeted Geoscience Initiative 4: Canadian Nickel-Copper-Platinum Group Element-Chromium Ore Systems – Fertility, Pathfinders, New and

Revised Models (ed.) D.E. Ames and M.G. Houle, Geological Survey of Canada, Open File 7856, 87-102.

Cawthorn, R.G., Barnes, S.J., Ballhaus, C., and Malitch, K.N. 2005. Platinum-group element, chromium, and vanadium deposits in bafic and ultramafic rocks. Economic Geology, **100:** 215-249.

Chakraborty, K.L. and Chakraborty, T.L. 1984. Geological Features and Origin of the Chromite Deposits of Sukinda Valley, Orissa, India. Mineralium Deposita, **19:** 256-265.

Duffy, J.A. 1993. A review of optical basicity and its applications to oxidic systems. Geochimica et Cosmochimica Acta, **57:** 3961-3970.

Eggins S.M., Kinsley L.P.J., & Shelley J.M.M. 1998. Deposition and element fractionation processes during atmospheric pressure laser sampling for analysis by ICPMS. Appl. Surf. Sci, 127-129, 278-286.

Eriksson, P.G. and Reczko, B.F.F. 1995. The sedimentary and tectonic setting of the Transvaal Supergroup floor rocks to the Bushveld complex. Economic Geology, **21:** 487-504.

Finn, C.A., Bedrosian, P.A., Cole, J.C., Khoza, T.D., and Webb, S.J. 2015. Mapping the 3D extent of the Northern Lobe of the Bushveld layered mafic intrusion from geophysical data. Precambrian Research, **268:** 279-294.

Ford, C.E., Biggar, G.M., Humphries, D.J., Wilson, G., Dixon, D., and O'Hara, M.J. 1972. Role of water in the evolution of the lunar crust; an experimental study of samples 14310; an indication of lunar calc-alkaline volcanism. Proceedings of the Third Lunar Science Conference, **1:** 207-229.

Ghiorso, M.S., and Sack, R.O. 1991. Thermochemistry of the oxide minerals. *In* Oxide Minerals: Petrologic and Magnetic Significance. *Edited by* Donald H. Lindsley. Mineralogical Society of North America, Chelsea, Michigan. pp. 221-262.

Holzheid, A., Palme, H, and Chakraborty, S. 1997. The activities of NiO, CoO, and FeO in silicate melts. Chemical Geology, **139:** 21-38.

Huebner J.S. Lipin, B.R., Wiggins, L.B. 1976. Partitioning of chromium between silicate crystals and melts. Proceedings of the Seventh Lunar Science Conference, 1191-1220.

Irvine, T.N. 1965. Chromian spinel as a petrogenetic indicator: Part 1. Theory. Canadian Journal of Earth Sciences, **2(6):** 648-672.

Irvine, T.N. 1975. Crystallization sequences in the Muskox intrusion and other layered intrusions—II. Origin of chromitite layers and similar deposits of other magmatic ores. Geochimica et Cosmochimica Acta, **39:** 991-1020.

Irvine, T.N. 1977. Origin of chromitite layers in the Muskox intrusion and other stratiform intrusions: A new interpretation. Geology, **5:** 273-277.

Jenkins, M.C. and Mungall, J.E. (in press). Genesis of the Peridotite zone, Stillwater Complex, Montana, USA. Journal of Petrology,

Jochum, K.P., Nohl, U., Herwig, K., Lammel, E., Stoll, B., and Hofmann, A.W. 2005. GeoReM: A New Geochemical Database for Reference Materials and Isotopic Standards. Geostandards and Geoanalytical Research, **29:** 333-338.

Kress, V.C. and Carmichael, I.S.E. 1991. The compressibility of silicate liquids containing Fe_2O_3 and the effect of composition, temperature, oxygen fugacity and pressure on their redox states. Contributions to Mineralogy and Petrology, **108:** 82-92.

Kruger, F.J. 2005. Filling the Bushveld Complex magma chamber: lateral expansion, roof and floor interaction, magmatic unconformities, and the formation of giant chromitite, PGE and Ti-V-magnetite deposits. Mineralium Deposita, **40:** 451-472.

Kurepin, V.A. 2005. A thermodynamic model of Fe-Cr spinels. Contributions to Mineralogy and Petrology, **149:** 591-599.

Kusky, T.M. 1998. Tectonic setting and terrane accretion of the Archean Zimbabwe craton. Geology, **26:** 163-166.

Laarman, J.E. 2014. A Detailed Metallogenic Study of the McFaulds Lake Chromite Deposits, Northern Ontario. PhD thesis, The University of Western Ontario, London, Ontario.

Latypov, R., Costin, G., Chistyakova, S., Hunt, E.J., Mukherjee, R., and Naldrett, T. 2018. Platinum-bearing chromite layers are caused by pressure reduction during magma ascent. Nature Communications, **9:** 462.

Lipin, B.R. 1993. Pressure Increases, the Formation of Chromite Seams, and the Development of the Ultramafic Series in the Stillwater Complex, Montana. Journal of Petrology, **34:** 955-976.

Liu, T.C., and Presnall, D.C. 1990. Liquidus phase relationships on the join anorthite-forsterite-quartz at 20 kbar with applications to basalt petrogenesis and igneous sapphirine. Contributions to Mineralogy and Petrology, **104:** 735-742.

Matveev, S., and Ballhaus, C. 2002. Role of water in the origin of podiform chromitite deposits. Earth and Planetary Science Letters, **203:** 235-243.

Metsaranta, R.T., Houle, M.G., McNicoll, V.J., and Kamo, S.L. 2015. Revised geological framework for the McFaulds Lake greenstone belt, Ontario. *In* Targested Geoscience Initiative 4: Canadian Nickel-Copper-Platinum Group Elements-Chromium Ore Systems – Fertility, Pathfinders, New and Revised Models, (ed.) D.E. Ames and M.G. Houle, Geological Survey of Canada, Open File 7856, 61-73.

Mondal, S.K. and Mathez, E.A. 2007. Origin of the UG2 chromitite layer, Bushveld Complex. Journal of Petrology, **48:** 495-510.

Mungall, J.E., Harvey, J.D., Balch, S.J., Azar, B., Atkinson, J., and Hamilton, M.A. 2010. Eagle's Nest: A Magmatic Ni-Sulfide Deposit in the James Bay Lowlands, Ontario, Canada. Society of Economic Geologists, Inc. Special Publication, **15:** 539-557.

Mungall, J.E., Kamo, S.L., and McQuade, S. 2016. U-Pb geochronology documents out-of-sequence emplacement of ultramafic layers in the Bushveld Igneous Complex of South Africa. Nature Communications, **7:** 13385.

Mungall , J.E. and Brenan, J.M. 2014. Partitioning of platinum-group elements and Au between sulfide liquid and basalt and the origins of mantle-crust fractionation of the chalcophile elements. Geochimica et Cosmochimica Acta, **125:** 265-289.

Murck, B.W. and Campbell, I.H. 1986. The effects of temperature, oxygen fugacity and melt composition on the behaviour of chromium in basic and ultrabasic melts. Geochimica et Cosmochimica Acta, **50:** 1871-1887.

Murthy, Y.R., Tripathy, S.K., and Kumar, C.R. 2011. Chrome ore beneficiation challenges & opportunities – A review. Minerals Engineering, **24:** 375-380.

Nicholson, D.M. and Mathez, E.A. 1991. Petrogenesis of the Merensky Reef in the Rustenburg section of the Bushveld Complex. Contributions to Mineralogy and Petrology, **107:** 293-309.

Nikolaev, G.S., Ariskin, A.A., and Barmina, G.S. 2018. SPINMELT-2.0: Simulation of Spinel-Melt Equilibrium in Basaltic Systems under Pressures up to 15 Kbar: I. Model Formulation, Calibration, and Tests. Geochemistry International, **56:** 24-45.

O'Neil, M.J. (ed). 2001. The Merck Index – An encyclopedia of Chemicals, Drugs, and Biologicals. 13th Edition, Whitehouse Station, NJ: Merck and Co, Inc. pp. 5804.

O'Neill, H. StC. 1987. The quartz-fayalite-iron and quartz-fayalite-magnetite equilibria and the free energies of formation of fayalite (Fe_2SiO_4) and magnetite (Fe_3O_4). American Mineralogist, **72:** 67-75.

O'Neill, H. StC., and Wall, V.J. 1987. The olivine-orthopyroxene-spinel oxygen geobarometer, the nickel precipitation curve, and the oxygen fugacity of the Earth's upper mantle. Journal of Petrology, **28:** 1169-1191.

Page, N.J. 1977. Stillwater Complex, Montana: Rock Succession, Metamorphism and Structure of the Complex and Adjacent Rocks. No. 999, US Govt. Print. Off.

Parkinson, I.J., and Arculus, R.J. 1999. The redox state of subduction zones: insights from arc-peridotites. Chemical Geology, **160:** 409-423.

Pearce, N.J.G., Perkins, W.T., Westgate, J.A., et al. 1997. A compilation of new and published major and trace element data for NIST SRM 610 and NIST SRM 612 glass reference materials. Geostandards Newsletter, vol 21, pp 115-144.

Pollard, D.D., Delaney, P.T., Duffield, W.A., Endo, E.T., and Okamura, A.T. 1983. Surface deformation in volcanic rift zones. Developments in Geotectonics, **19:** 541-84.

Rayner, N., and Stott, G.M. 2005. Discrimination of Archean domains in the Sachigo Subprovince: a progress report on the geochronology. Summary of Field Work and Other Activities, **10:** 1.

Roeder, P.L. and Reynolds, I. 1991. Crystallization of Chromite and Chromium Solubility in Basaltic Melts. Journal of Petrology, **32:** 909-934.

Sisson, T.W. and Grove, T.L. 1993. Experimental investigations of the role of H_2O in calc-alkaline differentiation and subduction zone magmatism. Contributions to Mineralogy and Petrology, **113:** 143-166.

Stowe, C.W. 1994. Compositions and tectonic settings of chromite deposits through time. Economic Geology, **89:** 528-546.

Spandler, C., Mavrogenes, J., and Arculus, R. 2005. Origin of chromitites in layered intrusions: Evidence from chromite-osted melt inclusions from the Stillwater Complex. Geology, **33:** 893-896.

Taylor, J.R., Wall, V.J., Pownceby, M.I. 1992. The calibration and application of accurate redox sensors. American Mineralogist, **77:** 284-295.

U.S. Geological Survey, 2018. Mineral commodity summaries 2018. https://doi.org/10.3133/70194932.

von Seckendorff, V., and O'Neill, Hugh St.C. 1993. An experimental study of Fe-Mg partitioning between olivine and orthopyroxene at 11723 1273, and 1423 K and 1.6 GPa. Contributions to Mineralogy and Petrology, **113:** 196-207.

Waychunas, G.A. 1991. Crystal chemistry of oxides and oxyhydroxides. *In* Oxide minerals: petrologic and magnetic significance. *Edited by* Donald H. Lindsley. Mineralogical Association of America, Chelsea, Michigan. pp. 11-61.

Zeh, A., Ovtcharova, M., Wilson, A.H., and Schaltegger, U. 2015. The Bushveld Complex was emplaced and cooled in less than one million years – results of zirconology, and geotectonic implications. Earth and Planetary Science Letters, **418:** 103-114.

Table 1.3. Black Thor chromite compositions used to estimate the fO_2 of the ROFIS.

Sample ID	Fe# (sp)	Cr/3+ (sp)	Fe/3+ (sp)	Al/3+ (sp)	Ti/4O (sp)	Fe# (ol)	$K_D^{sp\text{-}ol}$ (Mg)[1]	T(ºC)	log fO_2	ΔFMQ
221-2-1a	0.60	0.58	0.07	0.36	0.015	0.10	13.45	607	-18.40	1.33
221-2-1b	0.60	0.57	0.07	0.36	0.015	0.10	12.60	623	-17.82	1.41
221-2-1c	0.62	0.57	0.07	0.36	0.016	0.11	13.61	602	-18.65	1.26
221-2-2a	0.46	0.60	0.06	0.35	0.014	0.10	7.59	783	-14.22	0.81
221-2-2b	0.47	0.60	0.05	0.34	0.013	0.10	7.95	767	-14.70	0.70
221-2-2c	0.48	0.60	0.06	0.34	0.013	0.10	8.23	756	-14.83	0.81
221-2-3a	0.64	0.58	0.06	0.36	0.012	0.10	15.30	572	-19.65	1.27
221-2-4a	0.52	0.62	0.06	0.32	0.011	0.11	9.08	738	-15.38	0.70
221-2-4b	0.53	0.57	0.07	0.36	0.011	0.11	9.38	699	-15.93	1.13
221-2-5a	0.60	0.58	0.06	0.36	0.014	0.10	13.81	596	-18.95	1.14
221-2-5b	0.61	0.57	0.06	0.37	0.014	0.09	15.29	573	-19.38	1.49
264-4-1a	0.67	0.52	0.09	0.39	0.021	0.11	15.61	561	-19.43	1.86
264-4-1b	0.68	0.52	0.11	0.37	0.018	0.11	16.79	559	-19.22	2.18
264-4-1c	0.66	0.51	0.09	0.40	0.014	0.13	13.24	578	-19.15	1.56
264-4-2b	0.75	0.53	0.13	0.34	0.013	0.13	19.61	544	-19.72	2.20
264-4-3a	0.65	0.55	0.09	0.36	0.017	0.13	11.95	641	-17.27	1.42
264-4-3b	0.64	0.56	0.08	0.36	0.018	0.14	11.25	650	-17.28	1.14
264-4-4a	0.78	0.53	0.11	0.35	0.018	0.14	21.03	518	-21.06	1.90
251-2-1a	0.58	0.57	0.07	0.35	0.018	0.11	11.57	653	-16.99	1.34
251-2-1b	0.70	0.56	0.08	0.35	0.017	0.09	24.05	498	-21.65	2.12
251-2-1c	0.63	0.57	0.07	0.36	0.016	0.03	48.85	383	-25.70	3.85
251-2-2a	0.65	0.61	0.07	0.31	0.016	0.12	13.06	644	-17.45	1.13
251-2-2b	0.67	0.63	0.07	0.30	0.015	0.12	15.11	620	-18.13	1.19
251-2-3a	0.61	0.56	0.08	0.36	0.015	0.11	13.27	612	-18.01	1.57
202.5-5a	0.80	0.65	0.09	0.26	0.008	0.13	25.94	522	-21.28	1.49
209-1-2a	0.56	0.59	0.06	0.36	0.009	0.09	12.26	625	-18.07	1.09
209-1-2b	0.58	0.58	0.06	0.37	0.009	0.03	40.78	395	-25.44	3.41
209-1-2c	0.55	0.56	0.06	0.38	0.009	0.10	11.61	623	-18.02	1.22
209-1-1a	0.69	0.58	0.07	0.35	0.013	0.04	46.78	396	-25.54	3.28
209-1-1b	0.68	0.57	0.07	0.36	0.013	0.09	21.25	510	-21.42	1.84
209.5-2b	0.83	0.59	0.12	0.29	0.012	0.14	28.92	495	-21.93	1.99
209.5-2c	0.80	0.56	0.11	0.33	0.013	0.16	21.68	516	-21.32	1.69
209.5-2d	0.82	0.58	0.11	0.31	0.012	0.13	29.87	474	-22.89	1.95
209.5-3b	0.83	0.65	0.09	0.26	0.008	0.16	25.92	513	-21.98	1.16
202.5-1a*	0.84	0.64	0.08	0.29	0.010	0.15	29.61	477	-23.58	1.11
202.5-2a*	0.94	0.64	0.34	0.01	0.042	0.17	84.74	508	-19.99	3.35
202.5-4a*	0.87	0.65	0.10	0.26	0.016	0.19	27.90	499	-22.63	1.09
202.5-4b*	0.95	0.61	0.38	0.01	0.039	0.17	96.60	493	-20.49	3.51
202.5-4c*	0.98	0.15	0.85	0.00	0.010	0.14	310.01	408	-22.88	5.23
202.5-5b*	0.98	0.27	0.73	0.00	0.016	0.18	183.15	443	-21.72	4.58
202.5-5c*	0.97	0.41	0.59	0.01	0.024	0.13	197.54	434	-22.04	4.70
209.5-1a*	0.96	0.53	0.45	0.01	0.038	0.14	143.85	458	-21.42	4.15
209.5-1b*	0.86	0.62	0.07	0.31	0.011	0.17	29.47	460	-24.63	0.84
209.5-1c*	0.95	0.57	0.42	0.01	0.040	0.16	110.03	483	-20.65	3.75
209.5-2a*	0.97	0.36	0.63	0.01	0.028	0.13	207.05	436	-21.82	4.80
209.5-3a*	0.88	0.66	0.10	0.24	0.015	0.15	40.11	460	-23.95	1.52

Sample ID	Fe# (sp)	Cr/3+ (sp)	Fe/3+ (sp)	Al/3+ (sp)	Ti/4O (sp)	Fe# (ol)	$K_D^{sp\text{-}ol}$ (Mg)[1]	T(ºC)	log fO_2	ΔFMQ
209.5-3c*	0.96	0.54	0.44	0.01	0.031	0.15	139.99	452	-21.89	3.96

1. The partition coefficient for Mg between olivine and spinel. 2. Asterisks indicate that sample has been disturbed by metamorphic processes. See section 1.3.4 for discussion.

Table 2.1. Synthetic starting material compositions.

Analyte (Wt.%)	Komatiite 1 (K1) *(n=15)*	Komatiite 2 (K2) *(n=8)*	Banded iron formation (BIF) *(n=15)*	Granodiorite (GD) *(n=15)*	Metasediment (MS) *(n=5)*
SiO_2	44.26	44.12	44.18	76.22	56.15
	0.21	*0.27*	*0.19*	*0.39*	*0.30*
TiO_2	0.45	0.44	2.91	0.24	0.76
	0.04	*0.02*	*0.07*	*0.05*	*0.03*
Al_2O_3	9.07	8.69	15.64	14.47	15.20
	0.09	*0.05*	*0.11*	*0.18*	*0.09*
FeO	12.21	12.53	23.34	2.45	9.77
	0.15	*0.22*	*0.14*	*0.06*	*0.08*
MnO	0.22	0.21	0.30	0.03	0.15
	0.02	*0.03*	*0.02*	*0.02*	*0.03*
MgO	23.55	22.73	3.57	1.05	3.93
	0.09	*0.07*	*0.05*	*0.04*	*0.07*
CaO	8.82	9.07	5.46	1.66	9.11
	0.10	*0.18*	*0.06*	*0.06*	*0.10*
Na_2O	0.50	0.44	2.26	4.48	3.48
	0.02	*0.02*	*0.04*	*0.08*	*0.08*
K_2O	0.78	0.76	1.13	0.78	0.14
	0.04	*0.03*	*0.03*	*0.02*	*0.01*
P_2O_5	-	0.00	1.07	0.00	0.00
	-	*0.02*	*0.07*	*0.03*	*0.03*
Cr (ppm)	2187	2121	-	-	-
	35	*29*	-	-	-
Total	99.86	98.99	99.87	101.37	98.69

Major element data obtained by EMPA analysis; Cr data obtained by LA-ICPMS. *n* = number of EPMA analyses. Small italicized numbers indicate 1 standard deviation. Dashes indicate analytes that were not measured. Chromium content is based on 5 analyses on each sample.

Table 2.2. External standard analyses compared to Georem accepted values.

Analyte	BHVO-1 Georem	BHVO-1 EPMA *(n=58)*[1]	BHVO-1 LA-ICPMS *(n=46)*	BIR-1 Georem	BIR-1 EPMA *(n=63)*	BIR-1 LA-ICPMS *(n=44)*
SiO_2	49.79	49.88	-[2]	47.79	47.78	-
	0.12	*0.77*	-	*0.16*	*0.6*	-
TiO_2	2.74	2.56	-	0.96	0.9	-
	0.01	*0.4*	-	*0.01*	*0.06*	-
Al_2O_3	13.69	13.63	-	15.51	15.25	-
	0.05	*0.62*	-	*0.07*	*0.52*	-
Cr_2O_3	0.042	0.036	-	0.057	0.06	-
	0.001	*0.023*	-	*0.001*	*0.023*	-
Cr (ppm)	288	-	291	393	-	384
	4	-	*13*	*4*	-	*13*
FeO	11.09	10.87	-	10.26	10.2	-
	0.04	*0.27*	-	*0.04*	*0.2*	-
MnO	0.169	0.167	-	0.173	0.164	-
	0.001	*0.027*	-	*0.002*	*0.026*	-
MgO	7.21	7.39	-	9.69	9.76	-
	0.03	*0.6*	-	*0.05*	*0.23*	-
CaO	11.43	11.57	-	13.29	13.58	-
	0.04	*0.55*	-	*0.06*	*0.3*	-
Na_2O	2.31	2.19	-	1.83	1.74	-
	0.02	*0.19*	-	*0.02*	*0.037*	-
K_2O	0.526	0.494	-	0.029	0.037	-
	0.005	*0.109*	-	*0.003*	*0.011*	-
P_2O_5	0.277	0.245	-	0.03	0.023	-
	0.002	*0.071*	-	*0.004*	*0.026*	-
Total	99.27	99.03	-	99.62	99.49	-

All oxide values are wt.%. 1. *n*= number of analyses. 2. Dashes indicate analytes that were not measured. Italicized numbers indicate 1 standard deviation.

Table 3.1. Results of Y-doped thermocouple calibration experiments.

Experiment	Wt.% NiO	Wt.% MnO	Total	X_{NiO}	log fO_2 from X_{NiO}	log fO_2 from sensor	Difference
Ni in F1	35.88	62.82	98.70	0.348	-8.34 *(0.01)*	-8.34	0.00
(n=10)[1]	*(0.11)*	*(0.24)*		*(0.001)*			
NiO in F1	34.07	64.21	98.28	0.334	-8.36 *(0.01)*	-8.34	-0.02
(n=8)	*(0.18)*	*(0.11)*		*(0.001)*			
Ni in F2	35.96	62.30	98.26	0.351	-8.34 *(0.01)*	-8.34	0.00
(n=9)	*(0.41)*	*(0.40)*		*(0.004)*			
NiO in F2	34.15	64.27	98.42	0.332	-8.36 *(0.01)*	-8.34	-0.02
(n=6)	*(0.21)*	*(0.15)*		*(0.002)*			

1. *n* = number of analyses. Small italicized numbers in brackets indicate 1 standard deviation.

Table 4.3. Summary of major and trace element composition of run-product glasses.

Sample	T (ºC)	ΔFMQ	t (h)[1]	Cont.[2]	%[3]	SiO_2	TiO_2	Al_2O_3	FeO	MgO	MnO	CaO	Na_2O	K_2O	P_2O_5	Cr (ppm)	Total
S1b_0	1192	0.16	48	-[5]	0	49.23	0.80	13.89	9.15	8.70	0.22	12.86	0.99	1.38	0.02	262	97.45
n=8[4]						*0.71*	*0.04*	*0.24*	*0.62*	*0.08*	*0.03*	*0.24*	*0.04*	*0.11*	*0.02*	*2*	*0.49*
S1b_20	1192	0.16	48	BIF	20	47.09	1.33	13.50	12.43	8.54	0.24	11.33	1.21	1.05	0.29	253	97.27
n=7						*0.29*	*0.05*	*0.21*	*0.52*	*0.35*	*0.02*	*0.29*	*0.04*	*0.05*	*0.04*	*2*	*0.46*
S1b_50	1192	0.16	48	BIF	50	47.16	1.95	13.29	15.09	8.20	0.26	8.07	1.64	1.07	0.50	175	97.50
n=5						*0.15*	*0.01*	*0.11*	*0.10*	*0.03*	*0.01*	*0.08*	*0.02*	*0.01*	*0.04*	*2*	*0.24*
S2a_0	1192	0.17	96	-	0	51.62	1.55	14.70	10.48	6.64	0.20	11.11	1.17	2.30	0.00	-[6]	100.01
n=15						*1.01*	*0.12*	*0.99*	*0.76*	*0.64*	*0.02*	*0.95*	*0.08*	*0.23*	*0.00*	*-*	*0.53*
S2a_20	1192	0.17	96	BIF	20	49.44	1.94	14.50	11.68	7.05	0.24	12.53	1.39	1.47	0.00	286	100.49
n=15						*0.82*	*0.14*	*0.19*	*0.66*	*0.13*	*0.03*	*0.16*	*0.05*	*0.10*	*0.00*	*45*	*0.43*
S2a_50	1192	0.17	96	BIF	50	47.80	2.49	15.35	15.21	6.34	0.26	9.16	1.79	1.32	0.00	119	99.97
n=15						*0.68*	*0.14*	*0.17*	*0.37*	*0.18*	*0.03*	*0.17*	*0.08*	*0.06*	*0.00*	*12*	*0.48*
S3a_0	1292	0.04	48	-	0	47.82	1.19	13.56	11.60	12.80	0.27	11.33	0.88	0.78	0.18	860	100.70
n=8						*0.46*	*0.03*	*0.04*	*0.38*	*0.22*	*0.02*	*0.18*	*0.03*	*0.03*	*0.04*	*6*	*0.29*
S4a_0	1392	0.48	48	-	0	45.92	0.57	11.28	11.76	17.04	0.24	11.92	0.20	0.23	0.03	1960	99.61
n=13						*0.35*	*0.05*	*0.15*	*0.28*	*0.31*	*0.02*	*0.19*	*0.02*	*0.02*	*0.03*	*27*	*0.34*
S4b_5	1393	-0.01	48	BIF	5	46.90	0.02	11.17	11.98	17.90	0.23	11.08	0.23	0.29	0.03	1923	100.27
n=9						*0.17*	*0.02*	*0.10*	*0.10*	*0.22*	*0.03*	*0.15*	*0.02*	*0.02*	*0.03*	*14*	*0.22*
S4b_10	1393	-0.01	48	BIF	10	46.99	0.01	11.24	12.00	17.71	0.23	10.56	0.26	0.33	0.04	1871	99.82
n=6						*0.25*	*0.02*	*0.17*	*0.18*	*0.52*	*0.02*	*0.23*	*0.02*	*0.02*	*0.02*	*11*	*0.37*
S4a_20	1392	0.48	48	BIF	20	46.08	1.03	11.37	13.35	16.77	0.24	9.49	0.32	0.31	0.09	1623	99.48
n=14						*0.17*	*0.05*	*0.11*	*0.21*	*0.14*	*0.02*	*0.13*	*0.02*	*0.02*	*0.03*	*16*	*0.29*
S5_0	1192	0.17	48	-	0	48.10	0.77	13.63	11.18	9.00	0.23	14.73	0.85	1.19	0.01	263	99.95
n=6						*0.71*	*0.02*	*0.14*	*0.23*	*0.06*	*0.04*	*0.43*	*0.04*	*0.03*	*0.02*	*11*	*0.19*
S5_5	1192	0.17	48	GD	5	51.24	0.71	13.97	8.60	8.59	0.19	13.87	1.34	1.28	0.02	343	100.04
n=7						*0.84*	*0.03*	*0.12*	*0.74*	*0.09*	*0.02*	*0.24*	*0.07*	*0.10*	*0.03*	*41*	*0.29*
S5_10	1192	0.17	48	GD	10	51.85	0.67	13.41	8.97	8.45	0.20	13.18	1.58	1.11	0.01	378	99.64
n=7						*0.31*	*0.04*	*0.11*	*0.28*	*0.05*	*0.03*	*0.15*	*0.04*	*0.04*	*0.02*	*6*	*0.16*

Sample	T (ºC)	ΔFMQ	t (h)	Cont.	%	SiO_2	TiO_2	Al_2O_3	FeO	MgO	MnO	CaO	Na_2O	K_2O	P_2O_5	Cr (ppm)	Total
S5a_0	1192	0.17	96	-	0	49.14	0.87	15.41	9.63	8.31	0.22	14.56	0.94	1.30	0.02	321	100.61
n=10						*0.45*	*0.05*	*0.13*	*0.31*	*0.05*	*0.03*	*0.22*	*0.06*	*0.06*	*0.03*	*11*	*0.31*
S5a_5	1192	0.17	96	GD	5	51.05	0.78	15.43	8.66	8.28	0.20	13.57	1.31	1.18	0.02	344	100.69
n=10						*0.64*	*0.04*	*0.25*	*0.75*	*0.08*	*0.04*	*0.36*	*0.06*	*0.09*	*0.02*	*17*	*0.31*
S5a_10	1192	0.17	96	GD	10	53.72	0.67	15.10	7.54	7.95	0.18	12.29	1.70	1.20	0.02	339	100.53
n=10						*0.87*	*0.05*	*0.20*	*0.54*	*0.20*	*0.02*	*0.27*	*0.07*	*0.07*	*0.03*	*15*	*0.42*
S6_5	1292	0.05	48	GD	5	50.19	0.63	11.98	9.18	13.38	0.23	12.28	0.87	0.84	0.01	1065	99.90
n=10						*0.19*	*0.04*	*0.07*	*0.10*	*0.10*	*0.02*	*0.09*	*0.01*	*0.03*	*0.02*	*25*	*0.28*
S6_10	1292	0.05	48	GD	10	51.43	0.58	11.83	8.86	13.22	0.21	11.30	1.09	0.84	0.01	1063	99.65
n=8						*0.25*	*0.04*	*0.20*	*0.16*	*0.42*	*0.01*	*0.18*	*0.02*	*0.02*	*0.01*	*35*	*0.32*
S7_5	1392	0.05	48	GD	5	49.02	0.51	10.00	10.00	19.62	0.24	9.64	0.27	0.27	0.01	2078	100.03
n=10						*0.18*	*0.03*	*0.09*	*0.26*	*0.44*	*0.02*	*0.18*	*0.01*	*0.01*	*0.02*	*31*	*0.22*
S7_10	1392	0.05	48	GD	10	50.88	0.44	9.69	8.93	20.80	0.22	8.54	0.19	0.15	0.01	1860	100.29
n=8						*0.12*	*0.02*	*0.07*	*0.06*	*0.04*	*0.02*	*0.17*	*0.01*	*0.01*	*0.02*	*28*	*0.31*
S8_K	1391	0.02	3	NM[7]	62	19.20	0.88	3.24	65.06	8.30	0.17	3.68	0.28	0.01	0.23	65	101.58
n=3						*0.90*	*0.07*	*0.20*	*0.86*	*0.31*	*0.01*	*0.16*	*0.03*	*0.01*	*0.02*	*5*	*0.33*
S8_1	1391	0.02	3	NM*[8]	65	21.29	0.80	3.28	61.51	9.42	0.19	3.95	0.25	0.03	0.23	126	101.46
n=3						*0.33*	*0.05*	*0.26*	*0.34*	*0.66*	*0.01*	*0.22*	*0.02*	*0.04*	*0.01*	*22*	*0.60*
S8_2	1391	0.02	3	NM*	59	22.21	0.78	3.77	59.32	8.84	0.20	4.76	0.32	0.03	0.31	182	101.10
n=3						*3.66*	*0.16*	*0.59*	*5.38*	*1.09*	*0.07*	*0.99*	*0.09*	*0.03*	*0.08*	*9*	*0.33*
S9_5	1192	0.24	48	MS	5	48.75	1.10	14.50	10.97	7.16	0.22	13.84	1.18	1.29	0.02	-	99.27
n=11						*0.25*	*0.10*	*0.17*	*0.28*	*0.14*	*0.02*	*0.25*	*0.04*	*0.06*	*0.02*	*-*	*0.32*
S9_10	1192	0.24	48	MS	10	49.84	1.02	14.57	10.73	7.03	0.20	12.98	1.39	1.14	0.02	319	99.15
n=11						*0.32*	*0.11*	*0.13*	*0.29*	*0.08*	*0.03*	*0.23*	*0.07*	*0.04*	*0.02*	*18*	*0.37*
S10_0	1292	0.02	48	-	0	47.34	0.68	13.46	10.84	11.38	0.23	14.10	0.47	0.69	0.03	-	99.52
n=13						*0.32*	*0.03*	*0.31*	*0.23*	*0.56*	*0.03*	*0.31*	*0.03*	*0.03*	*0.04*	*-*	*0.34*
S10_5	1292	0.03	48	MS	5	48.73	0.70	13.81	9.16	12.72	0.24	13.56	0.74	0.82	0.02	968	100.78
n=5						*0.15*	*0.01*	*0.16*	*0.19*	*0.07*	*0.05*	*0.16*	*0.03*	*0.02*	*0.02*	*48*	*0.37*
S10_10	1292	0.03	48	MS	10	49.28	0.67	13.80	9.31	12.59	0.24	13.14	0.86	0.82	0.02	948	101.03
n=5						*0.24*	*0.01*	*0.08*	*0.29*	*0.09*	*0.02*	*0.14*	*0.02*	*0.02*	*0.02*	*39*	*0.23*
S11_0	1392	0.08	48	-	0	46.27	0.57	11.34	11.24	17.37	0.24	11.79	0.53	0.32	0.02	1758	100.09
n=14						*0.15*	*0.04*	*0.10*	*0.11*	*0.13*	*0.03*	*0.14*	*0.02*	*0.02*	*0.02*	*16*	*0.33*
S11_5	1392	0.08	48	MS	5	46.68	0.58	11.25	10.98	17.43	0.24	11.58	0.54	0.32	0.02	1837	100.04
n=14						*0.35*	*0.04*	*0.12*	*0.33*	*0.27*	*0.03*	*0.20*	*0.03*	*0.02*	*0.02*	*7*	*0.35*

Sample	T (ºC)	ΔFMQ	t (h)	Cont.	%	SiO_2	TiO_2	Al_2O_3	FeO	MgO	MnO	CaO	Na_2O	K_2O	P_2O_5	Cr (ppm)	Total
S11_10	1392	0.08	48	MS	10	47.04	0.59	11.23	11.37	17.18	0.22	11.01	0.60	0.35	0.01	1837	100.02
n=11						*0.19*	*0.03*	*0.11*	*0.36*	*0.27*	*0.03*	*0.10*	*0.02*	*0.03*	*0.02*	*8*	*0.34*
S12_K	1412	0.11	48	-	0	47.47	0.53	10.92	10.53	19.58	0.22	11.01	0.22	0.32	0.02	2168	101.31
n=5						*0.44*	*0.05*	*0.10*	*0.17*	*0.08*	*0.04*	*0.09*	*0.01*	*0.02*	*0.02*	*46*	*0.48*
S12_B	1412	0.11	48	BIF	10	46.95	0.80	10.95	11.81	19.30	0.22	9.98	0.25	0.35	0.03	2035	101.08
n=5						*0.14*	*0.04*	*0.13*	*0.07*	*0.09*	*0.02*	*0.11*	*0.02*	*0.01*	*0.03*	*15*	*0.28*
S12_G	1412	0.11	48	GD	10	50.33	0.46	10.46	9.31	20.14	0.19	9.04	0.40	0.51	0.04	2058	101.32
n=4						*0.29*	*0.01*	*0.06*	*0.21*	*0.16*	*0.03*	*0.04*	*0.01*	*0.02*	*0.02*	*21*	*0.42*
S13_K	1422	0.04	48	-	0	47.31	0.51	10.59	10.46	20.08	0.22	10.72	0.13	0.21	0.01	2260	100.71
n=6						*0.04*	*0.04*	*0.06*	*0.14*	*0.11*	*0.04*	*0.12*	*0.01*	*0.02*	*0.02*	*18*	*0.33*
S13_B	1422	0.04	48	BIF	10	47.00	0.77	10.75	11.55	19.98	0.25	9.76	0.15	0.23	0.02	2142	100.92
n=6						*0.09*	*0.06*	*0.11*	*0.11*	*0.15*	*0.04*	*0.08*	*0.02*	*0.02*	*0.02*	*3*	*0.16*
S13_G	1422	0.04	48	GD	10	49.79	0.48	10.30	9.42	20.63	0.20	9.28	0.20	0.32	0.01	2139	101.06
n=5						*0.17*	*0.04*	*0.15*	*0.11*	*0.08*	*0.03*	*0.07*	*0.02*	*0.02*	*0.02*	*11*	*0.25*
S14_K	1293	0.04	96	-	0	49.30	0.69	13.44	8.92	16.85	0.22	13.61	0.49	0.82	0.02	1002	100.57
n=5						*0.14*	*0.04*	*0.13*	*0.08*	*0.26*	*0.08*	*0.03*	*0.13*	*0.02*	*0.03*	*7*	*0.01*
S14_B	1293	0.04	96	BIF	20	48.67	1.22	13.62	11.22	15.93	0.24	11.20	0.71	0.85	0.13	880	100.65
n=6						*0.46*	*0.07*	*0.15*	*0.05*	*0.33*	*0.05*	*0.01*	*0.08*	*0.03*	*0.02*	*8*	*0.03*
S14_G	1293	0.04	96	GD	10	52.49	0.57	13.12	8.38	16.52	0.20	11.63	0.87	0.97	0.02	1038	101.08
n=5						*0.29*	*0.02*	*0.07*	*0.11*	*0.90*	*0.04*	*0.04*	*0.08*	*0.03*	*0.01*	*17*	*0.02*
S15_0.5	1392	0.11	48	*	0	48.57	0.61	11.58	9.99	17.22	0.26	11.75	0.30	0.37	0.01	1826	101.08
n=5						*0.16*	*0.07*	*0.06*	*0.12*	*0.13*	*0.02*	*0.14*	*0.02*	*0.03*	*0.02*	*12*	*0.30*
S15_1	1392	0.11	48	*	0	48.04	0.58	11.49	9.50	17.58	0.25	11.62	0.30	0.35	0.01	1853	100.11
n=5						*0.30*	*0.03*	*0.18*	*0.22*	*0.20*	*0.03*	*0.11*	*0.02*	*0.02*	*0.01*	*30*	*0.32*
S15_2	1392	0.11	48	*	0	48.35	0.60	11.32	10.51	17.26	0.21	11.69	0.30	0.35	0.01	1855	101.01
n=5						*0.35*	*0.04*	*0.13*	*0.09*	*0.14*	*0.03*	*0.06*	*0.02*	*0.01*	*0.01*	*29*	*0.28*
S16_B	1392	0.08	48	BIF*	10	47.44	0.85	11.34	11.21	18.70	0.25	10.26	0.27	0.34	0.02	1872	101.13
n=5						*0.20*	*0.02*	*0.04*	*0.03*	*0.05*	*0.02*	*0.15*	*0.02*	*0.03*	*0.02*	*9*	*0.30*
S16_M	1392	0.08	48	MS*	10	49.11	0.56	11.22	9.51	19.14	0.21	10.58	0.29	0.34	0.01	2001	101.43
n=5						*0.09*	*0.04*	*0.07*	*0.09*	*0.08*	*0.04*	*0.11*	*0.02*	*0.01*	*0.02*	*6*	*0.14*
S16_G	1392	0.08	48	GD*	10	50.81	0.47	10.82	8.77	19.37	0.20	9.45	0.40	0.47	0.02	2212	101.23
n=6						*0.26*	*0.03*	*0.06*	*0.14*	*0.08*	*0.02*	*0.09*	*0.02*	*0.01*	*0.02*	*34*	*0.43*
S17_K	1392	-0.06	48	SM[9]	10	45.00	0.52	10.51	15.61	17.01	0.20	10.63	0.15	0.28	0.01	1727	100.39
n=6						*0.47*	*0.05*	*0.21*	*0.28*	*0.29*	*0.02*	*0.09*	*0.01*	*0.02*	*0.02*	*12*	*0.34*

Sample	T (ºC)	ΔFMQ	t (h)	Cont.	%	SiO_2	TiO_2	Al_2O_3	FeO	MgO	MnO	CaO	Na_2O	K_2O	P_2O_5	Cr (ppm)	Total
S17_0.5	1392	-0.06	48	SM*	10	44.73	0.53	10.50	16.38	16.65	0.22	10.82	0.14	0.25	0.00	1637	100.70
n=5						*0.30*	*0.05*	*0.10*	*0.26*	*0.12*	*0.02*	*0.06*	*0.03*	*0.01*	*0.01*	*20*	*0.21*
S18_K	1462	0.14	17	-	0	46.63	0.53	9.90	10.61	21.93	0.22	10.11	0.28	0.39	0.03	2296	101.10
n=6						*0.16*	*0.03*	*0.09*	*0.13*	*0.07*	*0.02*	*0.11*	*0.01*	*0.01*	*0.03*	*10*	*0.39*
S18_B	1462	0.14	17	BIF	10	46.47	0.74	9.97	11.26	21.80	0.24	9.04	0.32	0.40	0.03	2021	100.70
n=5						*0.25*	*0.04*	*0.13*	*0.12*	*0.07*	*0.02*	*0.11*	*0.03*	*0.02*	*0.02*	*45*	*0.58*
S18_G	1462	0.14	17	GD	10	48.95	0.44	9.83	9.60	22.18	0.20	8.68	0.44	0.50	0.03	1994	101.28
n=6						*0.20*	*0.03*	*0.07*	*0.12*	*0.10*	*0.03*	*0.09*	*0.02*	*0.02*	*0.02*	*13*	*0.29*
KGW	1450	-0.96	16	*	0	47.93	0.51	9.97	9.66	21.93	0.20	10.14	0.06	0.14	0.01	3798	101.16
n=6						*0.15*	*0.04*	*0.07*	*0.10*	*0.09*	*0.01*	*0.13*	*0.00*	*0.02*	*0.01*	*33*	*0.25*
S19_1	1293	0.96	48	*	0	50.71	0.71	13.23	7.48	13.17	0.23	13.77	0.67	0.94	0.00	871	101.24
n=5						*0.40*	*0.08*	*0.07*	*0.21*	*0.10*	*0.02*	*0.14*	*0.03*	*0.04*	*0.01*	*20*	*0.22*
S19_Mt	1293	0.96	48	SM*	10	44.32	0.66	11.68	17.74	11.63	0.19	12.34	0.44	0.66	0.01	553	100.18
n=6						*0.36*	*0.03*	*0.07*	*0.27*	*0.22*	*0.02*	*0.13*	*0.02*	*0.03*	*0.01*	*35*	*0.32*
S20_1	1392	1.08	48	*	0	48.32	0.58	11.09	9.16	19.03	0.22	11.45	0.17	0.35	0.02	1679	100.85
n=6						*0.21*	*0.03*	*0.08*	*0.12*	*0.08*	*0.02*	*0.06*	*0.02*	*0.01*	*0.01*	*43*	*0.20*
S20_Mt	1392	1.08	48	SM*	10	44.84	0.54	10.26	14.97	17.69	0.22	10.70	0.09	0.17	0.02	1433	100.01
n=5						*0.24*	*0.06*	*0.08*	*0.27*	*0.10*	*0.03*	*0.12*	*0.02*	*0.02*	*0.02*	*24*	*0.31*
S21_B30	1392	0.05	48	BIF	30	46.68	1.20	11.64	12.95	18.45	0.28	8.45	0.34	0.11	0.28	1565	100.79
n=5						*0.07*	*0.06*	*0.11*	*0.10*	*0.07*	*0.02*	*0.07*	*0.02*	*0.03*	*0.02*	*7*	*0.21*
S21_B40	1392	0.05	48	BIF	40	46.72	1.47	12.18	14.14	16.77	0.26	7.89	0.50	0.11	0.41	1295	100.85
n=5						*0.12*	*0.03*	*0.11*	*0.13*	*0.11*	*0.01*	*0.07*	*0.02*	*0.04*	*0.03*	*6*	*0.15*
S21_G30	1392	0.05	48	GD*	30	55.55	0.39	10.87	7.89	17.09	0.16	6.89	1.16	0.02	0.74	2241	101.25
n=5						*0.12*	*0.06*	*0.04*	*0.11*	*0.05*	*0.03*	*0.05*	*0.03*	*0.02*	*0.03*	*15*	*0.19*
S22_20	1422	0.21	48	BIF*	20	49.40	1.02	11.22	8.42	21.12	0.25	8.94	0.18	0.06	0.19	2415	101.30
n=4						*0.20*	*0.01*	*0.09*	*0.17*	*0.14*	*0.02*	*0.10*	*0.01*	*0.05*	*0.02*	*16*	*0.20*
S22_30	1422	0.21	48	BIF*	30	48.75	1.24	11.76	11.29	18.55	0.27	8.30	0.23	0.04	0.23	2309	101.17
n=5						*0.15*	*0.03*	*0.12*	*0.09*	*0.10*	*0.02*	*0.12*	*0.03*	*0.03*	*0.02*	*13*	*0.27*
S22_40	1422	0.21	48	BIF*	40	47.08	1.49	12.28	14.49	16.03	0.25	7.80	0.27	0.06	0.33	2153	100.60
n=4						*0.24*	*0.03*	*0.16*	*0.14*	*0.08*	*0.04*	*0.09*	*0.03*	*0.01*	*0.01*	*10*	*0.50*
S23_1	1192	0.23	24	*	0	49.25	0.88	15.34	10.53	7.95	0.19	13.98	1.25	0.01	1.18	337	100.81
n=5						*0.40*	*0.09*	*0.09*	*0.15*	*0.08*	*0.03*	*0.20*	*0.04*	*0.01*	*0.02*	*55*	*0.25*
S23_B	1192	0.23	24	BIF*	20	48.01	1.53	15.02	12.37	7.86	0.20	12.58	1.33	0.39	1.21	292	100.76
n=5						*0.75*	*0.09*	*0.29*	*0.38*	*0.09*	*0.02*	*0.25*	*0.01*	*0.04*	*0.11*	*44*	*0.15*

Sample	T (ºC)	ΔFMQ	t (h)	Cont.	%	SiO_2	TiO_2	Al_2O_3	FeO	MgO	MnO	CaO	Na_2O	K_2O	P_2O_5	Cr (ppm)	Total
S23_G	1192	0.23	24	GD*	10	53.39	0.69	14.84	8.89	7.60	0.16	12.03	1.98	0.03	1.15	355	100.96
n=5						*1.52*	*0.05*	*0.27*	*0.96*	*0.18*	*0.02*	*0.55*	*0.15*	*0.03*	*0.17*	*21*	*0.32*
S24_5	1391	0.06	3	NM*	5	43.44	0.65	10.23	18.60	15.63	0.22	10.21	0.61	0.02	0.79	1303	100.86
n=5						*0.13*	*0.04*	*0.06*	*0.14*	*0.10*	*0.02*	*0.10*	*0.03*	*0.02*	*0.04*	*36*	*0.28*
S24_10	1391	0.06	3	NM*	10	40.15	0.69	9.89	23.75	14.55	0.24	9.91	0.55	0.03	0.72	1137	100.97
n=5						*0.25*	*0.03*	*0.13*	*0.46*	*0.72*	*0.02*	*0.25*	*0.05*	*0.02*	*0.02*	*17*	*0.26*
S25_40	1393	0.05	48	BIF*	40	49.11	1.54	12.79	11.12	16.79	0.25	8.17	0.25	0.08	0.28	2065	100.84
n=5						*0.31*	*0.03*	*0.12*	*0.13*	*0.08*	*0.03*	*0.08*	*0.02*	*0.05*	*0.02*	*17*	*0.41*
S26_20	1291	-0.13	48	BIF	20	47.75	1.26	13.89	11.61	12.50	0.26	11.06	0.89	0.28	0.89	857	100.68
n=5						*0.25*	*0.06*	*0.08*	*0.17*	*0.09*	*0.02*	*0.05*	*0.02*	*0.06*	*0.04*	*14*	*0.46*
S26_50	1291	-0.13	48	BIF	50	46.76	1.88	13.75	15.08	12.19	0.28	8.01	1.09	0.38	0.81	755	100.54
n=5						*0.14*	*0.08*	*0.21*	*0.20*	*0.10*	*0.01*	*0.05*	*0.04*	*0.03*	*0.04*	*4*	*0.37*
S26_D50	1291	-0.13	48	BIF*	50	47.00	1.91	13.44	14.81	12.22	0.25	7.82	1.19	0.42	0.82	804	100.19
n=4						*0.18*	*0.03*	*0.12*	*0.16*	*0.09*	*0.01*	*0.04*	*0.03*	*0.04*	*0.02*	*3*	*0.36*
S27_1	1422	0.08	24	*	0	48.06	0.57	10.61	9.18	20.15	0.21	10.86	0.17	0.01	0.31	2354	100.59
n=4						*0.18*	*0.06*	*0.23*	*0.19*	*0.04*	*0.01*	*0.26*	*0.02*	*0.01*	*0.01*	*10*	*0.54*
S27_10	1422	0.08	24	BIF*	10	47.54	0.91	10.95	10.56	19.98	0.24	9.53	0.19	0.03	0.31	2304	100.75
n=5						*0.10*	*0.04*	*0.14*	*0.12*	*0.11*	*0.02*	*0.12*	*0.02*	*0.03*	*0.03*	*5*	*0.24*

1. t (h) indicates experiment duration. 2. Cont. indicates contaminant composition. 3. % indicates weight percentage added contaminant. 4. *n* = number of analyses. 5. Dashes in Cont. column indicate no contaminant was added. 6. Dashes in Cr (ppm) column indicate samples that did not have areas of melt large enough for LA-ICPMS analysis. 7. NM = natural magnetite. 8. Asterisks indicate added synthetic chromite. 9. SM = synthetic magnetite. Small italicised numbers indicate 1 standard deviation.

Table 4.5. Summary of major element composition of run-product chromites.

Code	T (°C)	ΔFMQ	Cont.[1]	%[2]	SiO_2	TiO_2	Al_2O_3	Cr_2O_3	FeO	MnO	MgO	Total	Cr/3+[3]	Fe/3+[4]	Al/3+[5]	Cr#[7]	Fe#[8]
S3a_0	1292	0.04	-[10]	0	0.22	0.74	27.31	33.26	18.05	0.25	16.75	96.58	0.40	0.10	0.49	0.45	0.25
n=5[9]					*0.01*	*0.03*	*1.33*	*1.81*	*0.15*	*0.00*	*0.02*						
S3a_20	1292	0.04	BIF	20	0.22	0.92	26.50	34.06	19.52	0.27	15.97	97.45	0.42	0.10	0.48	0.46	0.29
n=6					*0.02*	*0.07*	*1.68*	*1.67*	*0.34*	*0.01*	*0.33*						
S4b_5	1393	-0.01	BIF	5	0.46	0.36	18.85	46.03	15.30	0.25	18.60	99.84	0.55	0.11	0.34	0.62	0.17
n=3					*0.21*	*0.01*	*0.56*	*0.87*	*0.07*	*0.02*	*1.11*						
S4b_10	1393	-0.01	BIF	10	0.22	0.44	19.27	46.01	15.51	0.25	17.49	99.18	0.56	0.09	0.35	0.62	0.21
n=5					*0.01*	*0.02*	*0.30*	*0.56*	*0.08*	*0.02*	*0.38*						
S5_0	1192	0.17	-	0	0.41	0.69	19.22	15.83	44.11	0.28	13.44	93.99	0.21	0.42	0.37	0.36	0.36
n=5					*0.23*	*0.03*	*0.29*	*1.14*	*1.65*	*0.02*	*0.40*						
S5_5	1192	0.17	GD	5	2.08	0.48	25.45	31.55	21.40	0.27	15.63	96.87	0.39	0.14	0.47	0.45	0.28
n=4					*2.09*	*0.03*	*0.84*	*0.28*	*2.20*	*0.02*	*0.15*						
S6_0	1292	0.05	-	0	0.41	0.38	27.01	38.62	11.47	0.29	19.43	97.60	0.46	0.07	0.47	0.49	0.14
n=5					*0.31*	*0.06*	*1.85*	*2.68*	*0.45*	*0.02*	*0.34*						
S6_5	1292	0.05	GD	5	0.34	0.39	21.09	42.40	15.96	0.27	16.23	96.69	0.53	0.08	0.39	0.57	0.25
n=4					*0.16*	*0.02*	*1.01*	*1.34*	*0.18*	*0.02*	*0.21*						
S6_10	1292	0.05	GD	10	0.43	0.39	20.36	43.23	16.06	0.27	16.34	97.07	0.54	0.09	0.38	0.59	0.24
n=4					*0.14*	*0.04*	*1.58*	*2.27*	*0.39*	*0.01*	*0.21*						
S7_0	1392	0.05	-	0	0.26	0.29	20.90	47.01	9.37	0.25	19.73	97.82	0.56	0.06	0.37	0.60	0.11
n=4					*0.06*	*0.03*	*0.95*	*1.04*	*0.08*	*0.01*	*0.38*						
S7_5	1392	0.05	GD	5	0.26	0.29	17.60	48.11	13.28	0.24	17.23	97.01	0.60	0.08	0.33	0.65	0.20
n=5					*0.08*	*0.02*	*0.26*	*0.32*	*0.05*	*0.02*	*0.27*						
S8_K	1391	0.02	NM	0	0.35	1.93	5.09	0.27	80.53	0.08	5.90	94.16	0.00	0.88	0.11	0.03	0.70
n=5					*0.02*	*0.05*	*0.21*	*0.10*	*0.14*	*0.02*	*0.07*						
S8_1	1391	0.02	NM*	0	0.28	1.95	5.31	1.09	79.50	0.08	6.00	94.20	0.02	0.87	0.12	0.12	0.70
n=5					*0.02*	*0.10*	*0.28*	*0.71*	*1.10*	*0.03*	*0.06*						
S8_2	1391	0.02	NM*	0	0.29	1.99	5.40	0.55	79.47	0.07	6.42	94.20	0.01	0.87	0.12	0.06	0.68
n=4					*0.02*	*0.06*	*0.07*	*0.10*	*0.46*	*0.01*	*0.07*						

Code	T (°C)	ΔFMQ	Cont.	%	SiO_2	TiO_2	Al_2O_3	Cr_2O_3	FeO	MnO	MgO	Total	Cr/3+	Fe/3+	Al/3+	Cr#	Fe#
S11_0	1392	0.08	-	0	0.26	0.32	19.56	45.98	14.66	0.25	16.98	98.02	0.56	0.08	0.36	0.61	0.22
n=5					*0.06*	*0.02*	*0.11*	*0.30*	*0.08*	*0.01*	*0.25*						
S11_5	1392	0.08	MS	5	0.37	0.35	19.68	46.59	14.09	0.25	17.29	98.61	0.57	0.07	0.36	0.61	0.21
n=7					*0.23*	*0.04*	*0.20*	*0.54*	*0.19*	*0.03*	*0.17*						
S11_10	1392	0.08	MS	10	0.33	0.33	19.12	46.15	14.75	0.24	16.58	97.50	0.57	0.08	0.35	0.62	0.23
n=6					*0.08*	*0.01*	*0.57*	*0.82*	*0.10*	*0.03*	*0.04*						
S12_K	1412	0.11	-	0	0.28	0.32	18.50	48.17	13.59	0.23	17.93	99.01	0.58	0.08	0.33	0.64	0.19
n=4					*0.04*	*0.03*	*0.31*	*0.26*	*0.28*	*0.01*	*0.10*						
S13_K	1422	0.04	-	0	0.22	0.32	19.32	47.47	13.39	0.23	17.99	98.94	0.57	0.08	0.35	0.62	0.19
n=4					*0.02*	*0.05*	*1.22*	*1.50*	*0.03*	*0.00*	*0.31*						
S13_B	1422	0.04	BIF	10	0.22	0.43	18.46	47.10	14.30	0.24	17.76	98.51	0.58	0.09	0.34	0.63	0.19
n=3					*0.05*	*0.03*	*0.46*	*0.72*	*0.03*	*0.03*	*0.38*						
S14_K	1293	0.04	-	0	0.23	0.40	22.85	43.08	15.65	0.26	16.85	99.32	0.52	0.07	0.41	0.56	0.25
n=4					*0.04*	*0.03*	*1.15*	*1.51*	*0.12*	*0.01*	*0.26*						
S14_B	1293	0.04	BIF	10	0.39	0.82	24.34	38.56	18.61	0.25	15.93	98.90	0.47	0.09	0.44	0.52	0.29
n=4					*0.29*	*0.03*	*1.50*	*1.76*	*0.10*	*0.01*	*0.33*						
S14_G	1293	0.04	GD	10	0.68	0.36	17.63	48.64	15.46	0.28	16.52	99.56	0.60	0.08	0.32	0.65	0.24
n=4					*0.31*	*0.04*	*0.61*	*0.70*	*0.11*	*0.02*	*0.90*						
S15_0.5	1392	0.11	*	0	0.29	0.33	18.86	48.18	14.26	0.25	18.37	100.54	0.58	0.09	0.34	0.63	0.18
n=3					*0.09*	*0.05*	*0.28*	*0.87*	*0.10*	*0.03*	*0.25*						
S15_1	1392	0.11	*	0	0.18	0.34	18.47	48.63	13.30	0.28	18.13	99.33	0.59	0.08	0.33	0.64	0.18
n=3					*0.02*	*0.03*	*0.67*	*0.55*	*0.13*	*0.03*	*0.15*						
S15_2	1392	0.11	*	0	0.22	0.35	18.09	48.35	14.58	0.26	17.33	99.38	0.59	0.08	0.33	0.64	0.21
n=4					*0.07*	*0.03*	*0.41*	*0.36*	*0.13*	*0.01*	*0.22*						
S16_B	1392	0.08	BIF*	10	0.33	0.46	18.86	46.65	14.54	0.23	17.30	98.38	0.57	0.08	0.35	0.62	0.21
n=4					*0.02*	*0.03*	*0.59*	*0.80*	*0.10*	*0.04*	*0.23*						
S16_M	1392	0.08	MS*	10	0.26	0.30	18.33	49.13	12.68	0.26	18.26	99.22	0.59	0.08	0.33	0.64	0.17
n=3					*0.03*	*0.02*	*0.70*	*1.36*	*0.11*	*0.02*	*0.04*						
S17_K	1392	-0.06	-	0	0.29	0.46	23.68	36.91	20.20	0.19	16.02	97.77	0.45	0.12	0.43	0.51	0.28
n=4					*0.13*	*0.02*	*0.48*	*0.72*	*0.16*	*0.03*	*0.13*						
S17_0.5	1392	-0.06	SM*	0	0.25	0.45	22.23	37.77	21.58	0.21	15.51	98.00	0.46	0.13	0.41	0.53	0.29
n=4					*0.13*	*0.06*	*0.38*	*0.73*	*0.36*	*0.02*	*0.19*						
S17_1	1392	-0.06	SM*	0	0.26	0.44	21.92	38.83	20.47	0.20	15.71	97.83	0.48	0.12	0.40	0.54	0.28
n=4					*0.08*	*0.03*	*1.26*	*2.35*	*0.17*	*0.01*	*0.18*						

Code	T (°C)	ΔFMQ	Cont.	%	SiO_2	TiO_2	Al_2O_3	Cr_2O_3	FeO	MnO	MgO	Total	Cr/3+	Fe/3+	Al/3+	Cr#	Fe#
KGW	1450	-0.96	*	0	0.23	0.32	17.11	53.02	10.67	0.23	18.01	99.60	0.64	0.05	0.31	0.68	0.18
n=6					*0.08*	*0.06*	*1.81*	*2.63*	*0.07*	*0.02*	*0.29*						
S19_1	1293	0.96	*	0	0.22	0.62	23.21	40.35	15.91	0.26	17.88	98.46	0.49	0.10	0.42	0.54	0.21
n=5					*0.10*	*0.11*	*1.32*	*2.12*	*0.45*	*0.03*	*0.30*						
S19_Mt	1293	0.96	SM*	10	0.20	0.67	19.32	27.58	36.99	0.19	12.05	97.00	0.35	0.28	0.37	0.49	0.43
n=6					*0.03*	*0.03*	*0.99*	*1.72*	*0.49*	*0.03*	*0.19*						
S20_1	1392	1.08	*	0	0.26	0.37	20.18	44.22	14.93	0.23	18.52	98.72	0.53	0.11	0.36	0.60	0.17
n=5					*0.14*	*0.03*	*1.78*	*2.41*	*0.21*	*0.01*	*0.33*						
S20_Mt	1392	1.08	SM*	10	0.25	0.42	18.64	37.41	25.33	0.22	15.77	98.04	0.46	0.19	0.34	0.57	0.27
n=6					*0.04*	*0.03*	*0.70*	*1.21*	*0.18*	*0.04*	*0.13*						
S22_20	1422	0.21	BIF*	20	0.25	0.53	17.03	51.85	10.42	0.27	18.64	98.99	0.63	0.06	0.31	0.67	0.16
n=5					*0.03*	*0.03*	*1.14*	*1.22*	*0.11*	*0.02*	*0.14*						
S22_30	1422	0.21	BIF*	30	0.18	0.69	17.54	49.53	14.00	0.27	16.82	99.03	0.61	0.06	0.32	0.65	0.23
n=5					*0.02*	*0.04*	*0.63*	*1.02*	*0.11*	*0.02*	*0.26*						
S23_1	1192	0.23	*	0	0.21	1.87	17.14	31.33	33.35	0.27	11.65	95.82	0.42	0.23	0.35	0.55	0.45
n=5					*0.02*	*0.16*	*2.49*	*1.20*	*2.55*	*0.02*	*0.66*						
S23_B	1192	0.23	BIF*	20	0.30	3.33	23.57	21.70	34.22	0.28	12.44	95.85	0.29	0.23	0.48	0.38	0.45
n=3					*0.11*	*0.38*	*6.15*	*5.42*	*1.28*	*0.02*	*1.00*						
S23_G	1192	0.23	GD*	10	0.38	2.65	20.91	22.70	35.89	0.24	12.29	95.06	0.31	0.27	0.42	0.42	0.44
n=5					*0.20*	*0.43*	*2.71*	*3.23*	*2.87*	*0.04*	*0.71*						
S24_5	1391	0.06	NM*	5	0.25	0.59	14.88	34.23	33.29	0.22	13.01	96.46	0.45	0.27	0.29	0.61	0.38
n=2					*0.01*	*0.08*	*2.22*	*2.36*	*3.91*	*0.03*	*0.38*						
S24_10	1391	0.06	NM*	10	0.34	1.15	22.82	24.73	34.08	0.20	13.32	96.62	0.31	0.25	0.43	0.42	0.39
n=3					*0.06*	*0.44*	*2.51*	*7.59*	*4.18*	*0.03*	*0.27*						
S25_20	1393	0.05	BIF*	20	0.34	0.25	10.72	31.83	35.10	0.24	16.38	94.87	0.41	0.38	0.21	0.67	0.20
n=4					*0.04*	*0.03*	*0.25*	*0.53*	*1.03*	*0.03*	*0.66*						
S25_40	1393	0.05	BIF*	40	0.30	0.94	20.24	45.51	14.46	0.25	16.57	98.27	0.57	0.06	0.38	0.60	0.25
n=5					*0.07*	*0.08*	*1.70*	*2.22*	*0.20*	*0.03*	*0.17*						
S26_20	1291	-0.13	BIF	20	0.64	0.82	25.10	37.61	17.44	0.27	15.68	97.57	0.46	0.08	0.46	0.50	0.29
n=4					*0.19*	*0.05*	*1.62*	*1.24*	*0.10*	*0.02*	*0.41*						
S26_50	1291	-0.13	BIF	50	0.29	1.36	27.89	31.16	21.31	0.25	14.43	96.68	0.39	0.09	0.52	0.43	0.36
n=5					*0.03*	*0.05*	*0.84*	*1.28*	*0.12*	*0.02*	*0.23*						
S27_1	1422	0.08	*	0	0.33	0.36	18.33	49.46	11.73	0.25	18.29	98.74	0.60	0.07	0.33	0.64	0.17
n=4					*0.11*	*0.04*	*2.14*	*2.89*	*0.02*	*0.02*	*0.38*						

Code	T (°C)	ΔFMQ	Cont.	%	SiO_2	TiO_2	Al_2O_3	Cr_2O_3	FeO	MnO	MgO	Total	Cr/3+	Fe/3+	Al/3+	Cr#	Fe#
S27_10	1422	0.08	BIF*	10	0.20	0.53	17.70	49.69	12.96	0.24	17.49	98.81	0.61	0.06	0.32	0.65	0.20
n=4					*0.02*	*0.06*	*1.05*	*1.45*	*0.07*	*0.03*	*0.17*						

1. Cont. indicates the composition of added contaminant. 2. % indicates the weight percentage of contaminant added. dashes indicate no contaminant was added; NM indicates natural magnetite; SM indicates synthetic magnetite; asterisks indicate added synthetic chromite.. 3. $Cr/3+ = Cr/(Cr+Al+Fe^{3+})$. 4. $Fe/3+ = Fe^{3+}/(Cr+Al+Fe^{3+})$. 5. $Al/3+ = Al/(Cr+Al+Fe^{3+})$. 6. $Mg\# = Mg/(Mg+Fe^{2+})$. 7. $Cr\# = Cr/(Cr+Al)$. 8. $Fe\# = Fe^{2+}/(Mg+Fe^{2+})$. 9. *n* = number of analyses. 10. Dashes indicate no contaminant added. Small italicized numbers indicate 1 standard deviation.

Table 4.6. Summary of major element composition of run-product olivines.

Code	T (ºC)	ΔFMQ	Cont.[1]	%[2]	SiO_2	Al_2O_3	Cr_2O_3	MgO	FeO	MnO	CaO	Total	Fo_n[3]
S3a_0	1292	0.04	-[5]	0	40.50	0.08	0.10	47.20	11.76	0.24	0.36	100.25	69
n=9[4]					*0.18*	*0.02*	*0.02*	*0.17*	*0.14*	*0.02*	*0.02*		
S4a_0	1392	0.48	-	0	41.16	0.08	0.12	49.71	8.98	0.19	0.36	100.61	76
n=5					*0.08*	*0.02*	*0.01*	*0.19*	*0.06*	*0.01*	*0.01*		
S4b_5	1393	-0.01	BIF	5	40.93	0.08	0.15	49.04	9.34	0.18	0.33	100.04	75
n=5					*0.19*	*0.01*	*0.02*	*0.14*	*0.09*	*0.01*	*0.01*		
S4b_10	1393	-0.01	BIF	10	40.96	0.09	0.17	48.90	9.44	0.18	0.30	100.04	74
n=5					*0.17*	*0.01*	*0.03*	*0.20*	*0.07*	*0.03*	*0.03*		
S6_5	1292	0.05	GD	5	40.78	0.06	0.11	48.68	9.81	0.22	0.41	100.07	74
n=8					*0.24*	*0.01*	*0.03*	*0.28*	*0.10*	*0.02*	*0.01*		
S6_10	1292	0.05	GD	10	40.86	0.05	0.13	49.19	9.49	0.21	0.35	100.27	74
n=10					*0.17*	*0.01*	*0.04*	*0.30*	*0.15*	*0.01*	*0.01*		
S7_5	1392	0.05	GD	5	41.13	0.07	0.15	50.57	7.89	0.16	0.30	100.29	78
n=3					*0.32*	*0.01*	*0.04*	*0.16*	*0.06*	*0.02*	*0.03*		
S7_10	1392	0.05	GD	10	41.44	0.07	0.18	51.36	7.13	0.14	0.25	100.57	80
n=5					*0.25*	*0.00*	*0.02*	*0.16*	*0.05*	*0.01*	*0.01*		
S10_0	1292	0.02	-	0	40.50	0.07	0.07	47.34	11.62	0.23	0.52	100.36	70
n=10					*0.21*	*0.01*	*0.02*	*0.15*	*0.09*	*0.02*	*0.03*		
S10_5	1292	0.03	MS	5	40.73	0.07	0.10	48.70	9.95	0.23	0.44	100.23	73
n=5					*0.24*	*0.03*	*0.03*	*0.17*	*0.08*	*0.02*	*0.03*		
S10_10	1292	0.03	MS	10	40.57	0.28	0.41	48.34	10.12	0.21	0.43	100.36	73
n=4					*0.63*	*0.49*	*0.64*	*0.73*	*0.35*	*0.01*	*0.02*		
S11_0	1392	0.08	-	0	41.25	0.09	0.16	49.83	8.66	0.18	0.38	100.56	76
n=5					*0.08*	*0.01*	*0.01*	*0.16*	*0.05*	*0.01*	*0.02*		
S11_5	1392	0.08	MS	5	41.11	0.08	0.19	50.14	8.40	0.19	0.38	100.48	77
n=4					*0.14*	*0.01*	*0.04*	*0.12*	*0.04*	*0.02*	*0.03*		
S11_10	1392	0.08	MS	10	41.12	0.09	0.16	49.89	8.68	0.18	0.36	100.48	76
n=5					*0.16*	*0.02*	*0.02*	*0.15*	*0.08*	*0.02*	*0.01*		
S12_K	1412	0.11	-	0	40.75	0.11	0.20	50.14	8.10	0.15	0.37	99.82	78
n=6					*0.16*	*0.01*	*0.01*	*0.18*	*0.10*	*0.01*	*0.02*		
S12_B	1412	0.11	BIF	10	41.25	0.11	0.20	50.14	8.91	0.16	0.30	101.07	76
n=6					*0.10*	*0.05*	*0.08*	*0.16*	*0.09*	*0.01*	*0.02*		

Code	T (ºC)	ΔFMQ	Cont.	%	SiO_2	Al_2O_3	Cr_2O_3	MgO	FeO	MnO	CaO	Total	Fo_n
S12_G	1412	0.11	GD	10	41.71	0.08	0.18	51.48	7.38	0.14	0.25	101.23	80
n=6					*0.08*	*0.02*	*0.02*	*0.13*	*0.09*	*0.01*	*0.02*		
S13_K	1422	0.04	-	0	40.93	0.08	0.15	50.30	8.00	0.16	0.33	99.96	78
n=3					*0.22*	*0.02*	*0.01*	*0.11*	*0.11*	*0.01*	*0.01*		
S13_B	1422	0.04	BIF	10	40.38	0.08	0.17	49.71	8.70	0.16	0.30	99.49	76
n=3					*0.17*	*0.01*	*0.01*	*0.13*	*0.01*	*0.01*	*0.01*		
S14_K	1293	0.04	-	0	41.21	0.08	0.15	49.21	9.74	0.22	0.43	101.03	74
n=6					*0.18*	*0.05*	*0.09*	*0.08*	*0.14*	*0.01*	*0.01*		
S14_B	1293	0.04	BIF	20	40.75	0.08	0.08	47.15	12.06	0.22	0.33	100.68	69
n=6					*0.10*	*0.03*	*0.02*	*0.28*	*0.11*	*0.01*	*0.02*		
S14_G	1293	0.04	GD	10	41.36	0.05	0.11	49.38	9.63	0.20	0.33	101.06	74
n=6					*0.25*	*0.01*	*0.02*	*0.18*	*0.10*	*0.03*	*0.01*		
S15_0.5	1392	0.11	*[6]	0	40.58	0.09	0.18	49.13	8.69	0.19	0.35	99.21	76
n=3					*0.29*	*0.02*	*0.04*	*0.12*	*0.07*	*0.01*	*0.01*		
S15_1	1392	0.11	*	0	40.38	0.07	0.18	49.49	8.08	0.16	0.38	98.74	77
n=3					*0.02*	*0.02*	*0.03*	*0.19*	*0.04*	*0.01*	*0.02*		
S15_2	1392	0.11	*	0	40.09	0.08	0.18	48.75	9.07	0.16	0.36	98.70	75
n=3					*0.19*	*0.02*	*0.02*	*0.08*	*0.11*	*0.01*	*0.01*		
S16_B	1392	0.08	BIF*	10	40.28	0.10	0.16	49.31	8.93	0.18	0.29	99.23	76
n=3					*0.19*	*0.02*	*0.01*	*0.09*	*0.04*	*0.00*	*0.01*		
S16_M	1392	0.08	MS*	10	41.57	0.08	0.20	51.40	7.49	0.16	0.30	101.20	79
n=6					*0.13*	*0.02*	*0.04*	*0.14*	*0.04*	*0.02*	*0.01*		
S16_G	1392	0.08	GD*	10	41.78	0.08	0.22	51.46	7.07	0.13	0.24	100.98	80
n=6					*0.25*	*0.01*	*0.03*	*0.31*	*0.07*	*0.01*	*0.01*		
S17_K	1392	-0.06	SM[7]	10	39.65	0.11	0.17	46.15	12.55	0.13	0.38	99.15	67
n=3					*0.04*	*0.02*	*0.02*	*0.09*	*0.09*	*0.01*	*0.01*		
S17_0.5	1392	-0.06	SM*	10	39.55	0.09	0.15	45.68	13.37	0.15	0.40	99.39	66
n=6					*0.31*	*0.02*	*0.02*	*0.21*	*0.12*	*0.01*	*0.03*		
S18_K	1462	0.14	-	0	41.57	0.10	0.19	51.44	7.00	0.14	0.34	100.77	80
n=6					*0.12*	*0.01*	*0.03*	*0.18*	*0.09*	*0.02*	*0.02*		
KGW	1450	-0.96	*	0	41.60	0.10	0.29	51.06	7.02	0.14	0.33	100.53	80
n=6					*0.14*	*0.02*	*0.04*	*0.07*	*0.10*	*0.02*	*0.01*		
S19_1	1293	0.96	*	0	41.58	0.07	0.13	50.26	7.78	0.22	0.41	100.45	78
n=6					*0.19*	*0.03*	*0.06*	*0.15*	*0.08*	*0.02*	*0.02*		

Code	T (ºC)	ΔFMQ	Cont.	%	SiO_2	Al_2O_3	Cr_2O_3	MgO	FeO	MnO	CaO	Total	Fo_n
S19_Mt	1293	0.96	SM*	10	39.83	0.20	0.08	43.14	16.34	0.19	0.47	100.25	60
n=6					*0.24*	*0.32*	*0.02*	*0.28*	*0.08*	*0.01*	*0.04*		
S20_1	1392	1.08	*	0	41.65	0.09	0.15	51.51	6.53	0.16	0.31	100.39	82
n=6					*0.09*	*0.02*	*0.03*	*0.06*	*0.05*	*0.02*	*0.03*		
S20_Mt	1392	1.08	SM*	10	40.94	0.09	0.12	48.27	10.44	0.16	0.34	100.36	72
n=6					*0.10*	*0.02*	*0.01*	*0.25*	*0.11*	*0.01*	*0.02*		

1. Cont. indicates the composition of added contaminant. 2. % indicates the weight percentage of contaminant added. 3. Fo_n indicates the fortersite component of the olivine. 4. *n* = number of analyses. 5. Dashes indicate no contaminant was added. 6. Asterisks indicate added synthetic chromite. 7. SM indicates synthetic magnetite. Small italicized numbers indicate 1 standard deviation.

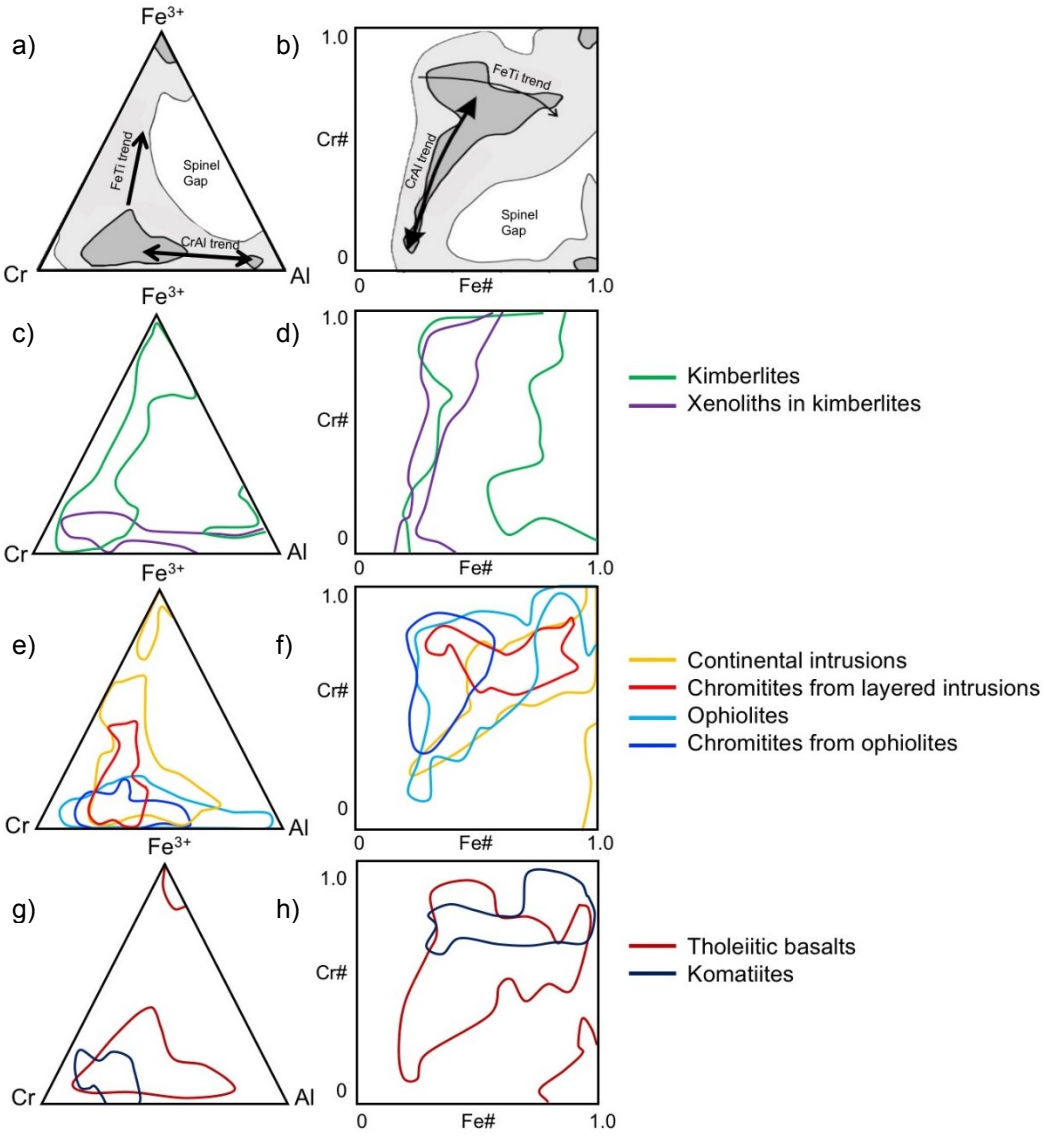

Figure 1.1. Ternary Cr-Al-Fe^{3+} and Cr# vs. Fe# diagrams depicting spinel chemistry of different rock types. Data from Barnes and Roeder (2001) and references therein. **(a)** Trivalent cation spinel chemistry from the entire global dataset. Dark and light grey contours are 95% and 50% percentiles, respectively. **(b)** Cr# vs. Fe# of spinel from the entire global dataset. Dark and light grey contours are 95% and 50% percentiles, respectively. **(c)** Trivalent cation spinel chemistry from kimberlitic chromite and chromite from kimberlitic xenoliths. **(d)** Cr# vs. Fe# of spinel from kimberlitic chromite and chromite from kimberlitic xenoliths. **(e)** Trivalent cation spinel chemistry from continental intrusions, chromitites from layered intrusions, ophiolites, and chromitites from ophiolites. **(f)** Cr# vs. Fe# of spinel from continental intrusions, chromitites from layered intrusions, ophiolites, and chromitites from ophiolites. **(g)** Trivalent cation spinel chemistry from tholeiitic basalts and komatiites. **(h)** Cr# vs. Fe# of spinel from tholeiitic basalts and komatiites.

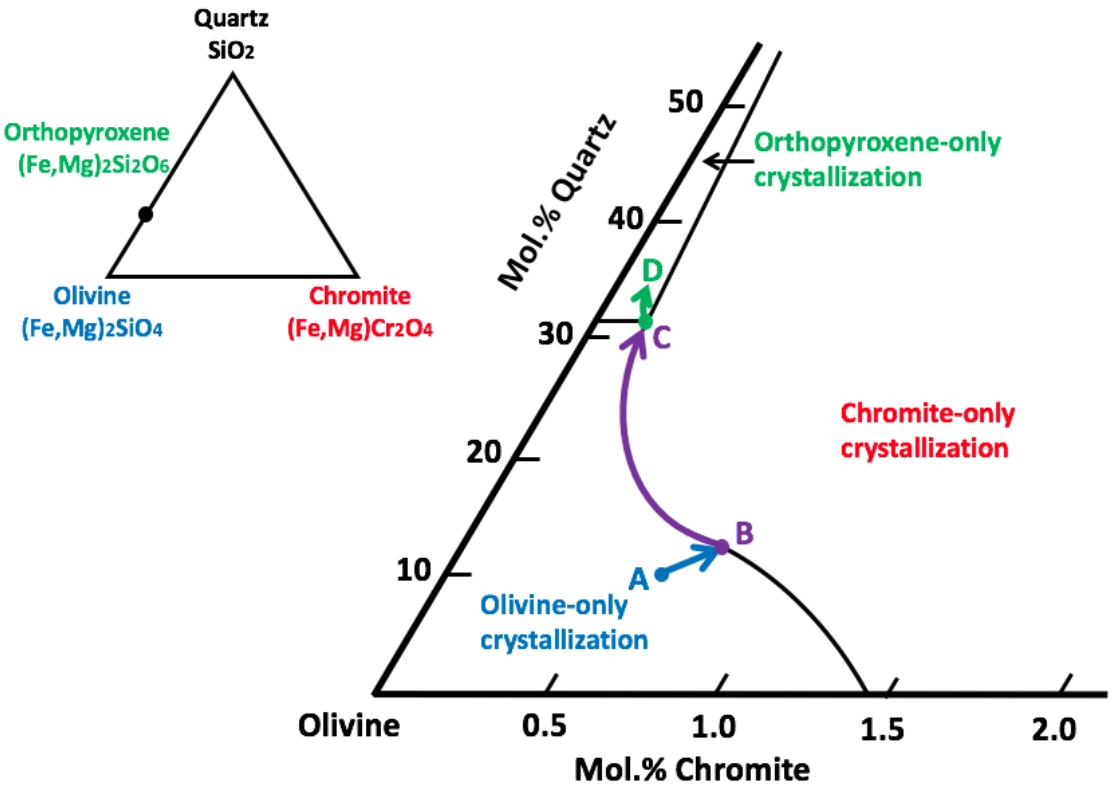

Figure 1.2.1. Schematic phase relations in the olivine-quartz-chromite ternary system, modified after Irvine (1977). The composition of a komatiite would plot in the olivine-only crystallization field, for example at point A. As olivine crystallized, the melt would evolve toward the cotectic between olivine and chromite (point B). Olivine and chromite would begin to crystallize and the melt would evolve along the cotectic until the distribution point C, when both olivine and chromite would cease to crystallize and orthopyroxene would crystallize alone. Blue lines indicate olivine-only crystallization, purple lines indicate olivine and chromite crystallization, and green lines indicate orthopyroxene crystallization. The horizontal scale (mol.% chromite) is exaggerated in order to show the curved nature of the cotectic.

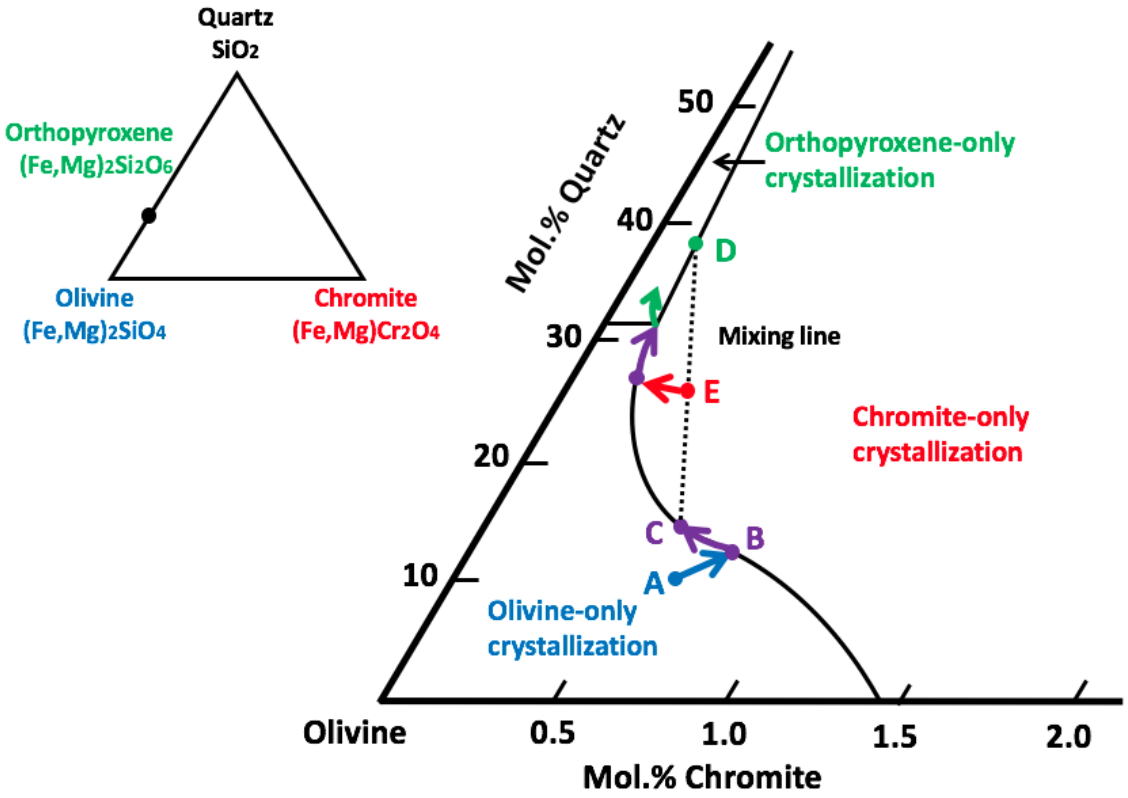

Figure 1.2.2. Schematic phase relations in the olivine-quartz-chromite ternary system, illustrating the magma mixing hypothesis, modified after Irvine (1977). A relatively primitive komatiite, such as a composition at point C, mixes with a more evolved komatiite of a composition at point D. The resulting melt would lie along the black dashed mixing line. If the melts mixed in equal proportions, the resulting composition would lie at point E, in the chromite-only crystallization field. That composition would crystallize chromite and evolve until it intersects the olivine-chromite cotectic, at which point it would resume the path of crystallization as described in Fig. 1.2.4. Blue lines indicate olivine-only crystallization, red lines indicate chromite-only crystallization, purple lines indicate olivine and chromite crystallization, and green lines indicate orthopyroxene crystallization. The horizontal scale (mol.% chromite) is exaggerated in order to show the curved nature of the cotectic.

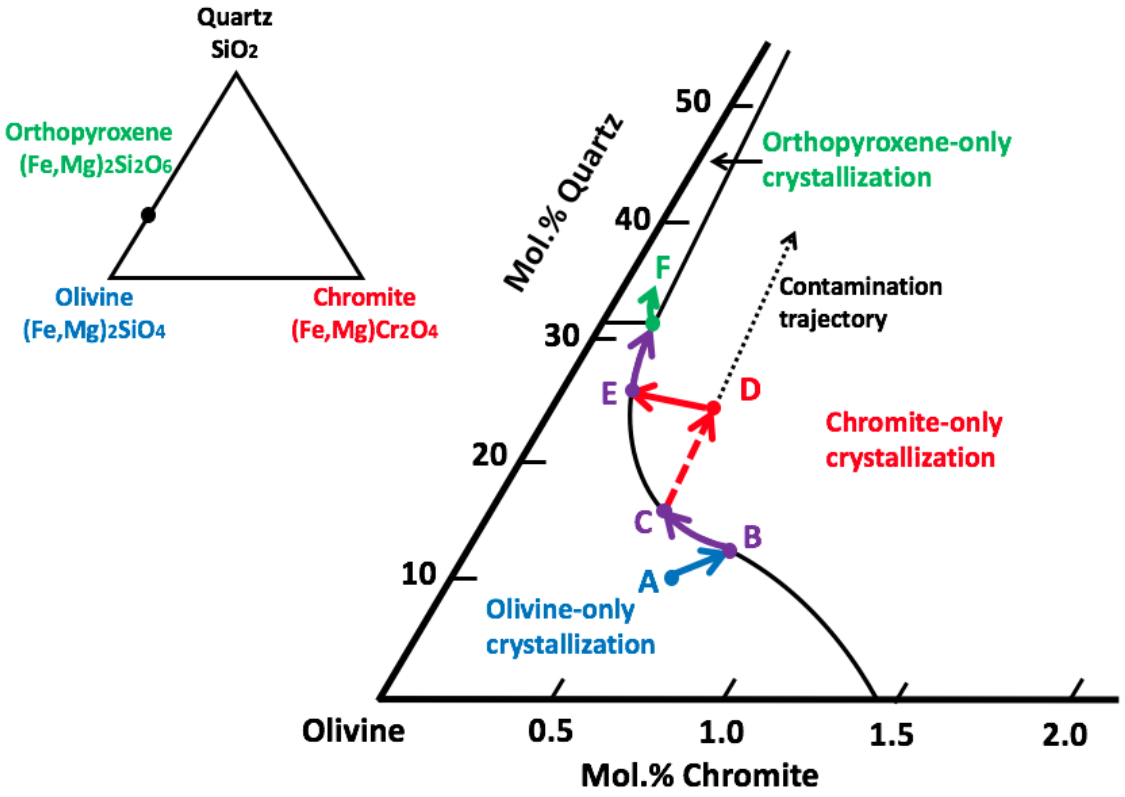

Figure 1.2.3. Schematic phase relations in the olivine-quartz-chromite ternary system, illustrating the contamination hypothesis, modified after Irvine (1977). A relatively primitive komatiite, such as a composition at point C, is contaminated by a much more siliceous country rock with a composition near the quartz apex. The contaminated melt composition would lie along the black dashed contamination trajectory. After an arbitrary amount of contamination, the melt would plot at point D, in the chromite-only crystallization field. It would crystallize chromite and evolve until it intersects the olivine-chromite cotectic (point E), at which point it would resume the crystallization path as described in Fig. 1.2.4. Blue lines indicate olivine-only crystallization, red lines indicate chromite-only crystallization, purple lines indicate olivine and chromite crystallization, and green lines indicate orthopyroxene crystallization. The horizontal scale (mol.% chromite) is exaggerated in order to show the curved nature of the cotectic.

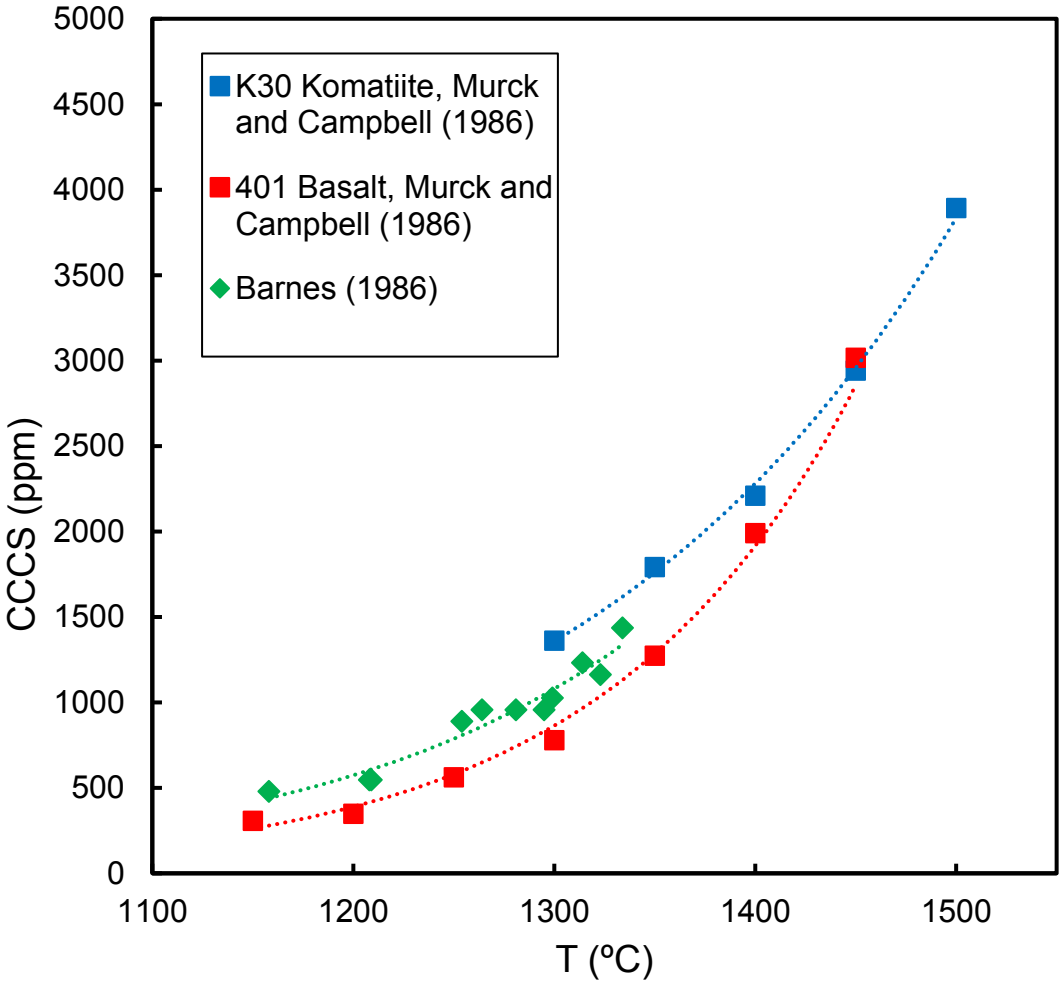

Figure 1.2.4. CCCS as a function of T(ºC). Data are shown for experiments involving basaltic (Barnes, 1986) and komatiitic (Murck and Campbell, 1986; Roeder and Reynolds, 1991) compositions at the temperatures indicated. Blue squares, red squares, and green diamonds indicate data from Murck and Campbell (1986), Roeder and Reynolds (1991), and Barnes (1986), respectively.

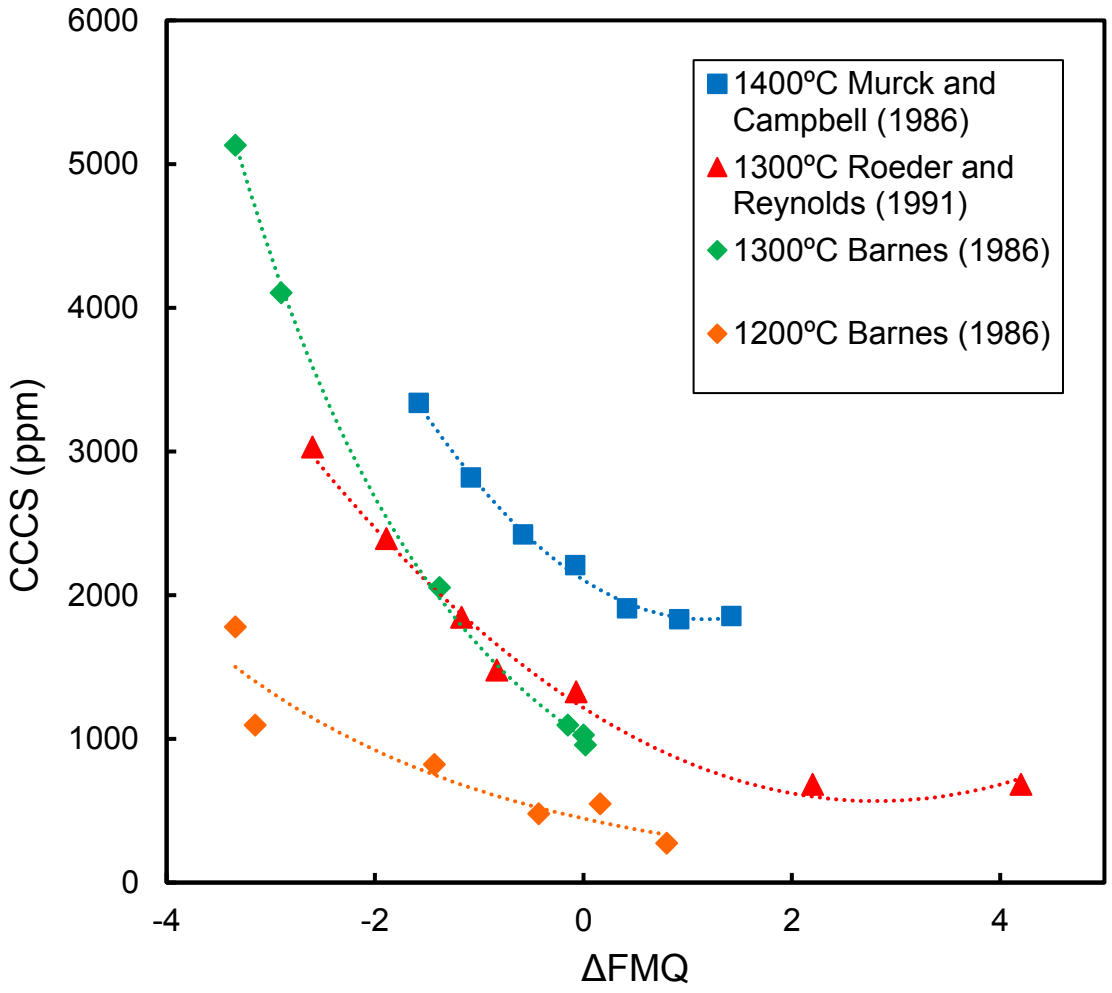

Figure 1.2.5. CCCS as a function of fO_2. Data are shown for experiments involving basaltic compositions (Barnes, 1986) and komatiitic compositions (Murck and Campbell, 1986; Roeder and Reynolds, 1991). Blue squares indicate data from Murck and Campbell (1986), red triangles indicate data from Roeder and Reynolds (1991), and diamonds indicate data from Barnes (1986).

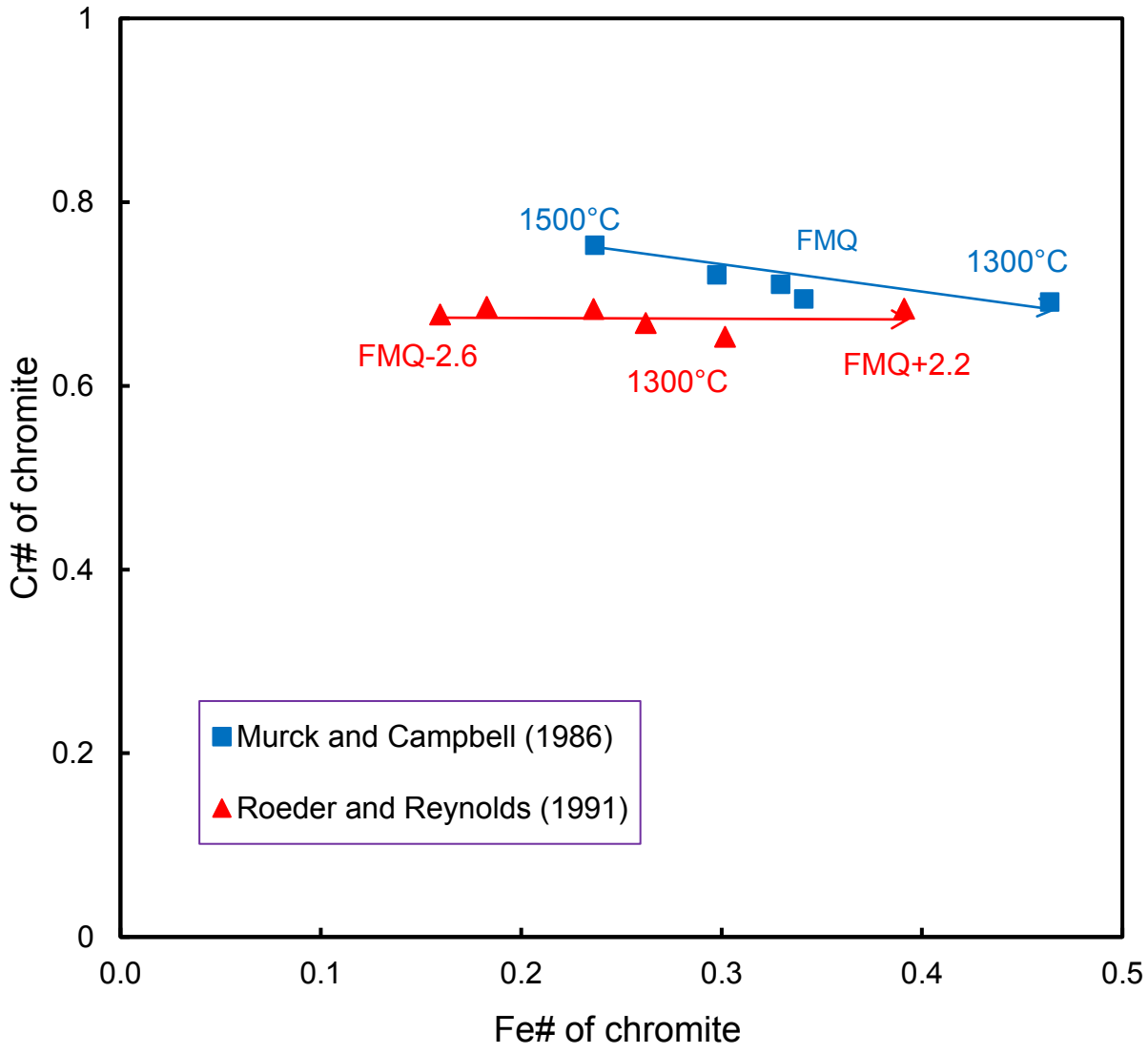

Figure 1.2.6. Cr# as a function of Fe# for chromites grown in komatiite compositions at various fO_2 and temperatures. The data show that Cr# decreases and Fe# increases with falling temperature. At a constant temperature of 1300ºC, results show that Fe# increases with increasing fO_2, but Cr# stays constant.

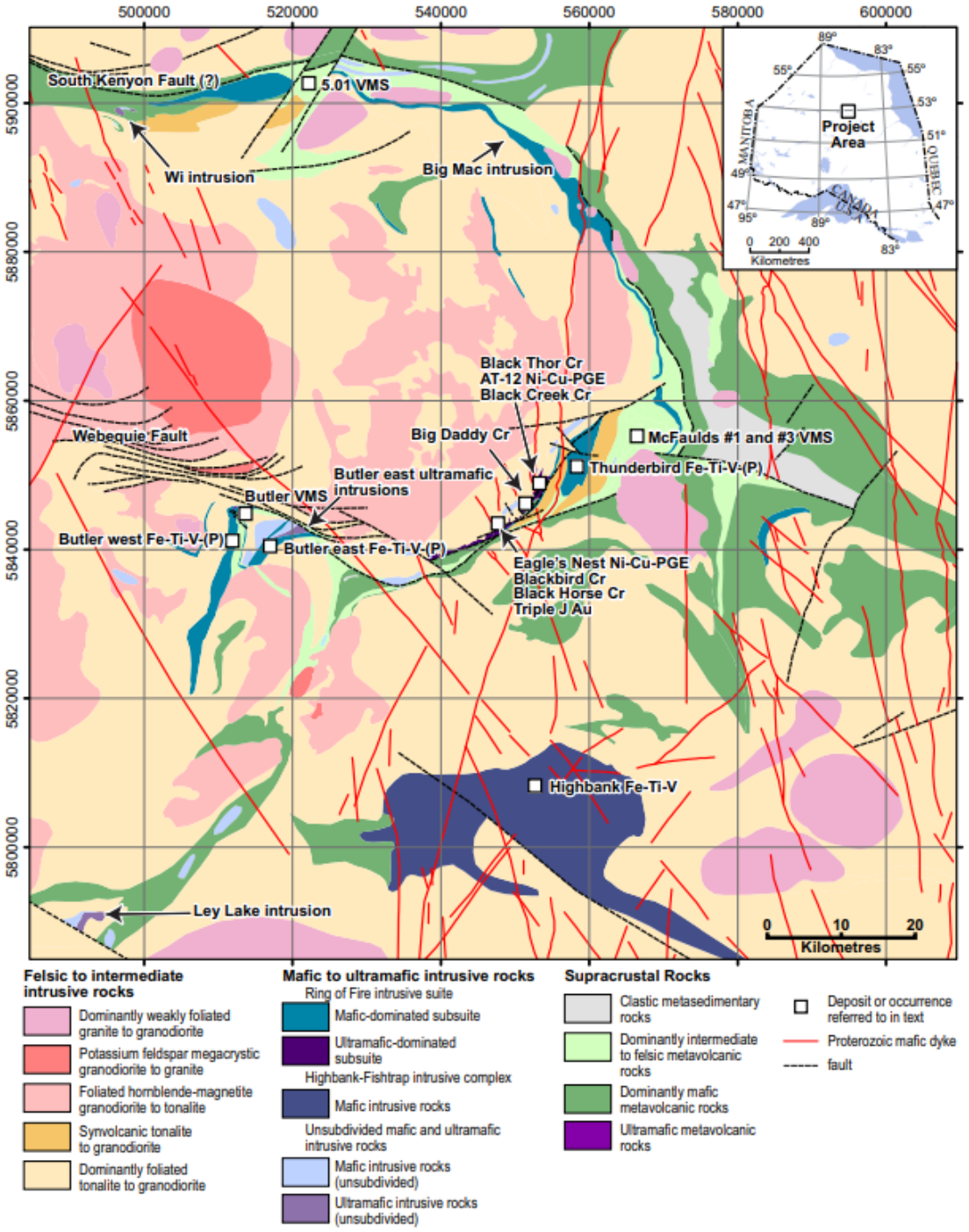

Figure 1.3.1. Geological map showing the spatial distribution of lithologies corresponding to the ROFIS and host rocks. Colours and symbols are explained in the legend. Metsaranta et al. (2015).

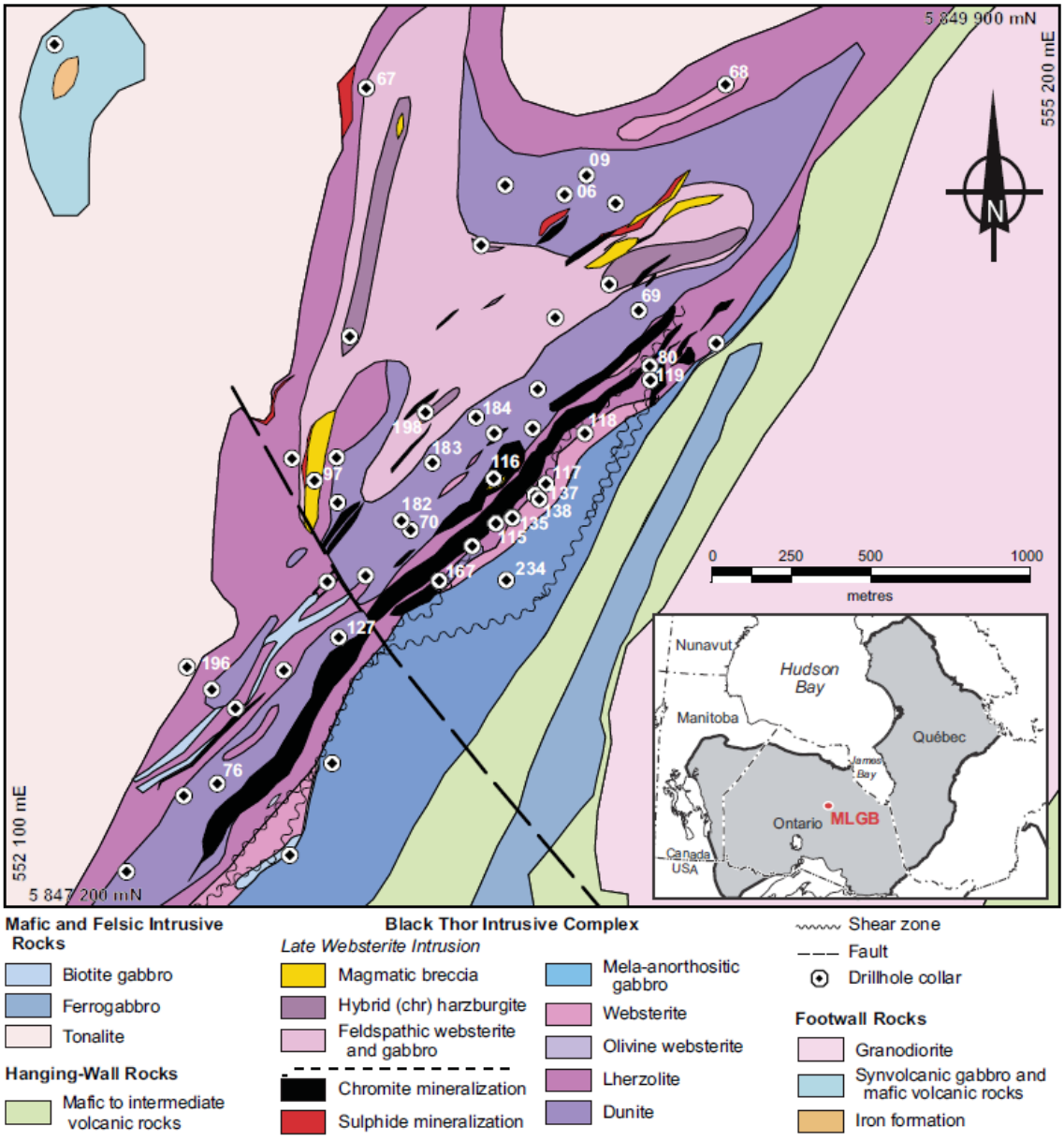

Figure 1.3.2. Geological map depicting the distribution of the Black Thor chromite deposit and associated country rocks. Colours and symbols are explained in the legend. Carson et al. (2015).

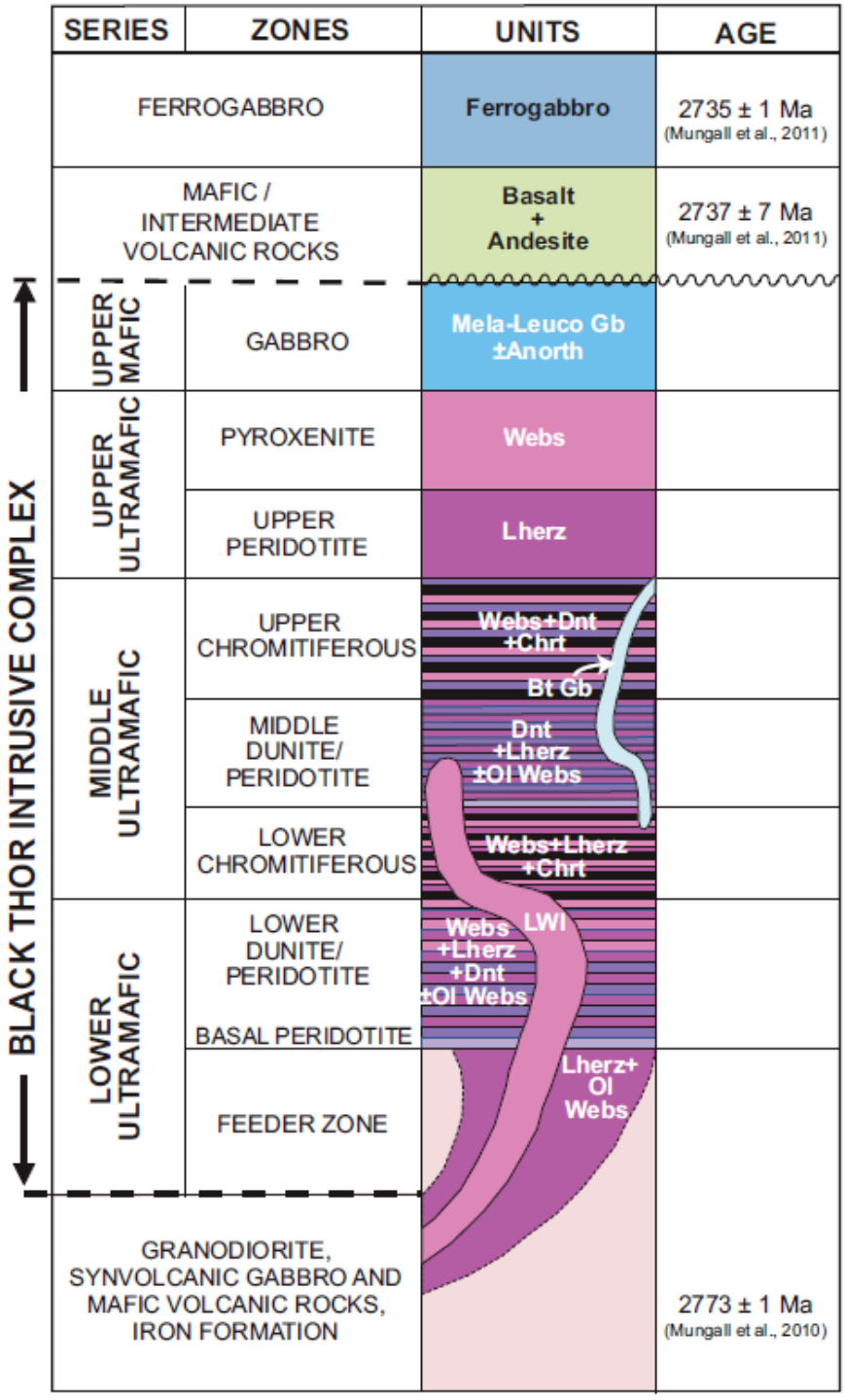

Figure 1.3.3. Generalized stratigraphy of the Black Thor chromite deposit. Carson et al. (2015).

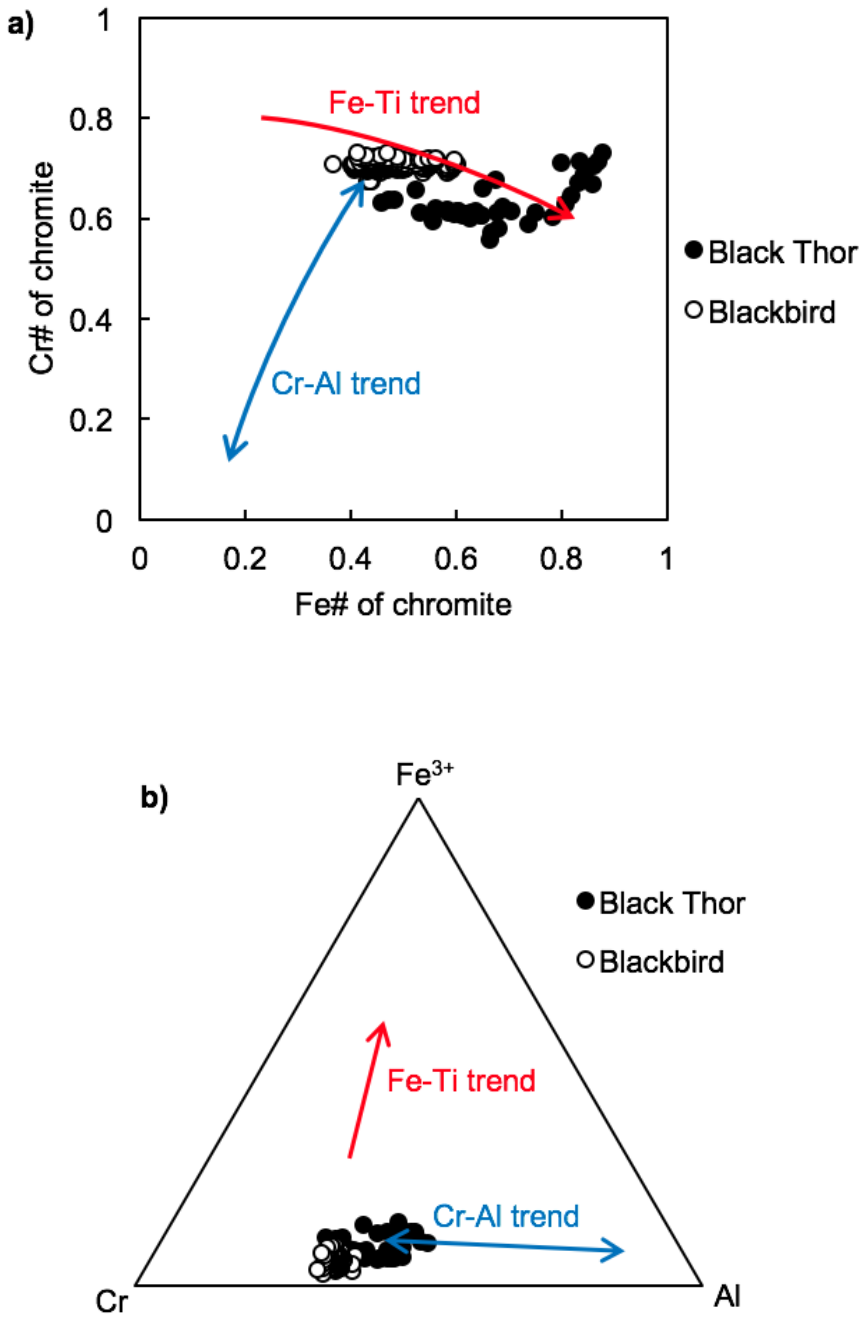

Figure 1.3.4. Chromite chemistry from the Blackbird and Black Thor deposits. a) Cr# vs. Fe# of chromite from the Blackbird and Black Thor deposits. Cr# clusters around 0.69. Fe# varies from 0.37-0.88 due to subsolidus re-equilibration with olivine. b) Trivalent cation plot showing a weak Cr-Al trend and an absence of the Fe-Ti trend. Red and blue lines indicate the Fe-Ti and Cr-Al magmatic trends, respectively, as described by Barnes and Roeder (2001). The Blackbird and Black Thor chromites do not follow either trend because their compositions reflect subsolidus Fe-Mg exchange with olivine.

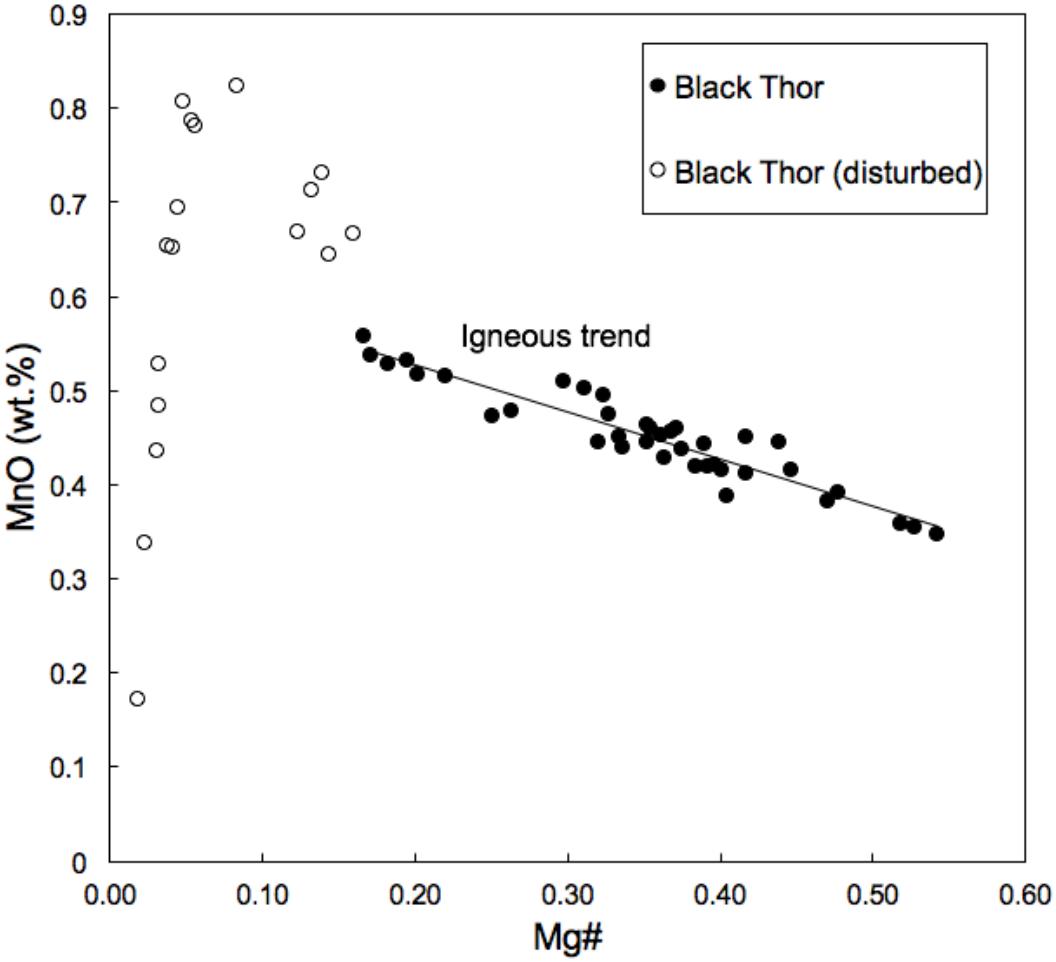

Figure 1.3.5. MnO as a function of Mg# of chromite from the Black Thor deposit. The relationship between chromite Mg# and wt.% MnO is used to distinguish between primary chromite compositions (solid circles), and those modified by metamorphism and alteration (open circles). The uniform MnO-Mg# slope exhibited by the igneous trend is consistent with chromite-olivine equilibrium for fixed $D^{chromite/olivine}$ of Mn at the magmatic stage (Barnes, 1998).

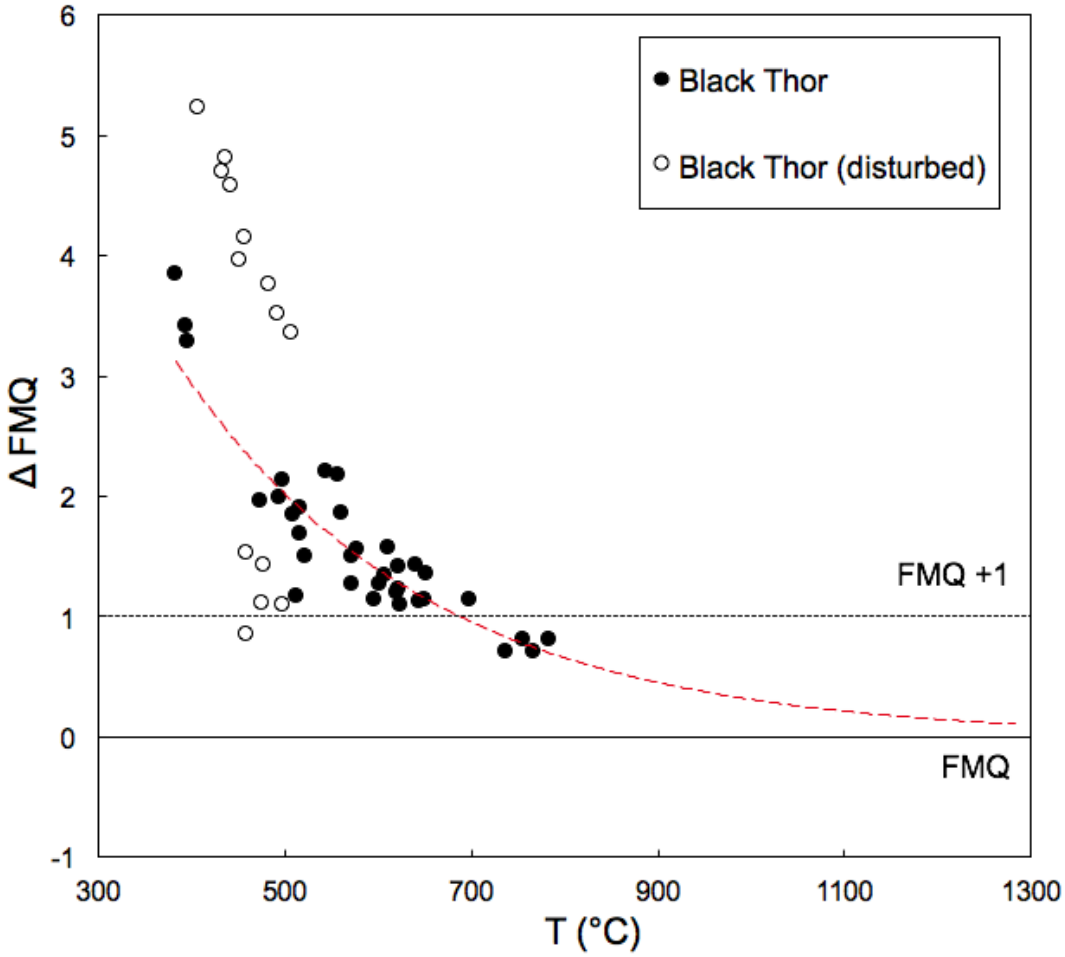

Figure 1.3.6. Variation in calculated oxygen fugacity and temperature for chromite-olivine pairs from the Black Thor deposit. Solid line indicates the FMQ buffer, dotted line indicates FMQ+1, solid circles indicate undisturbed chromites, and open circles indicate chromites that have been disturbed by metamorphic processes. Red dashed line indicates the projection of a best-fit line through the Black Thor dataset to higher temperatures.

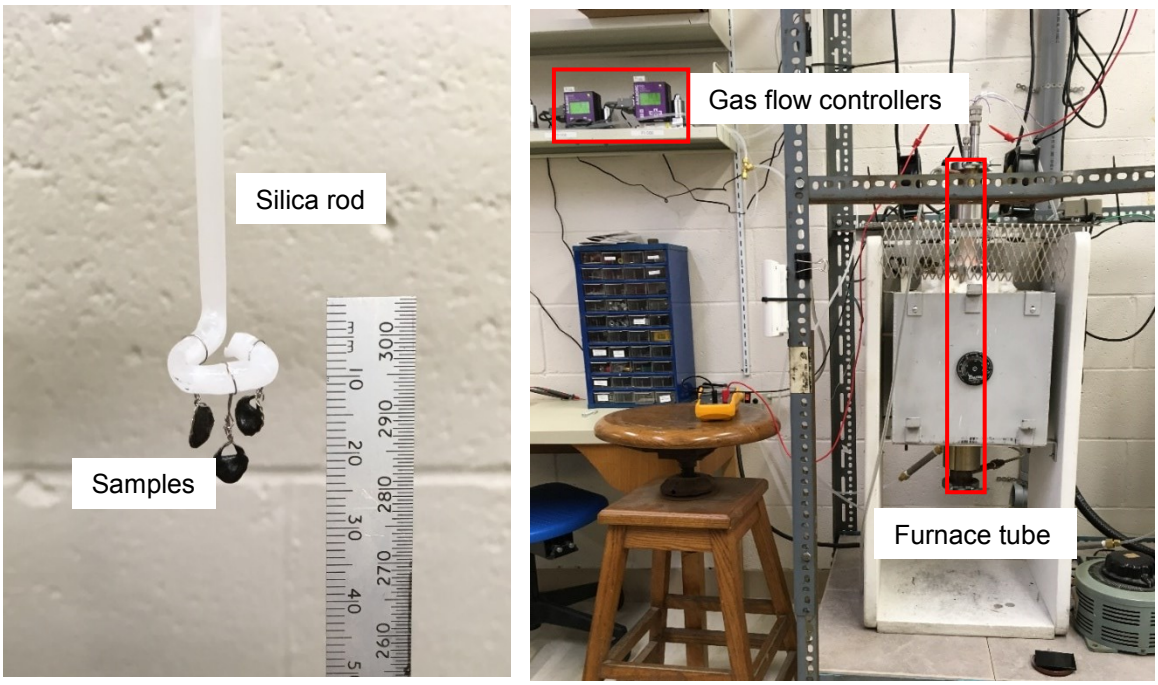

Figure 2.1. Images portraying aspects of the experiment configuration and laboratory apparatus. (a) Three samples attached to Pt loops and suspended from a fused silica rod. (b) One of the vertical tube gas mixing furnaces used in this study, indicating the gas flow controllers and the position of the furnace tube.

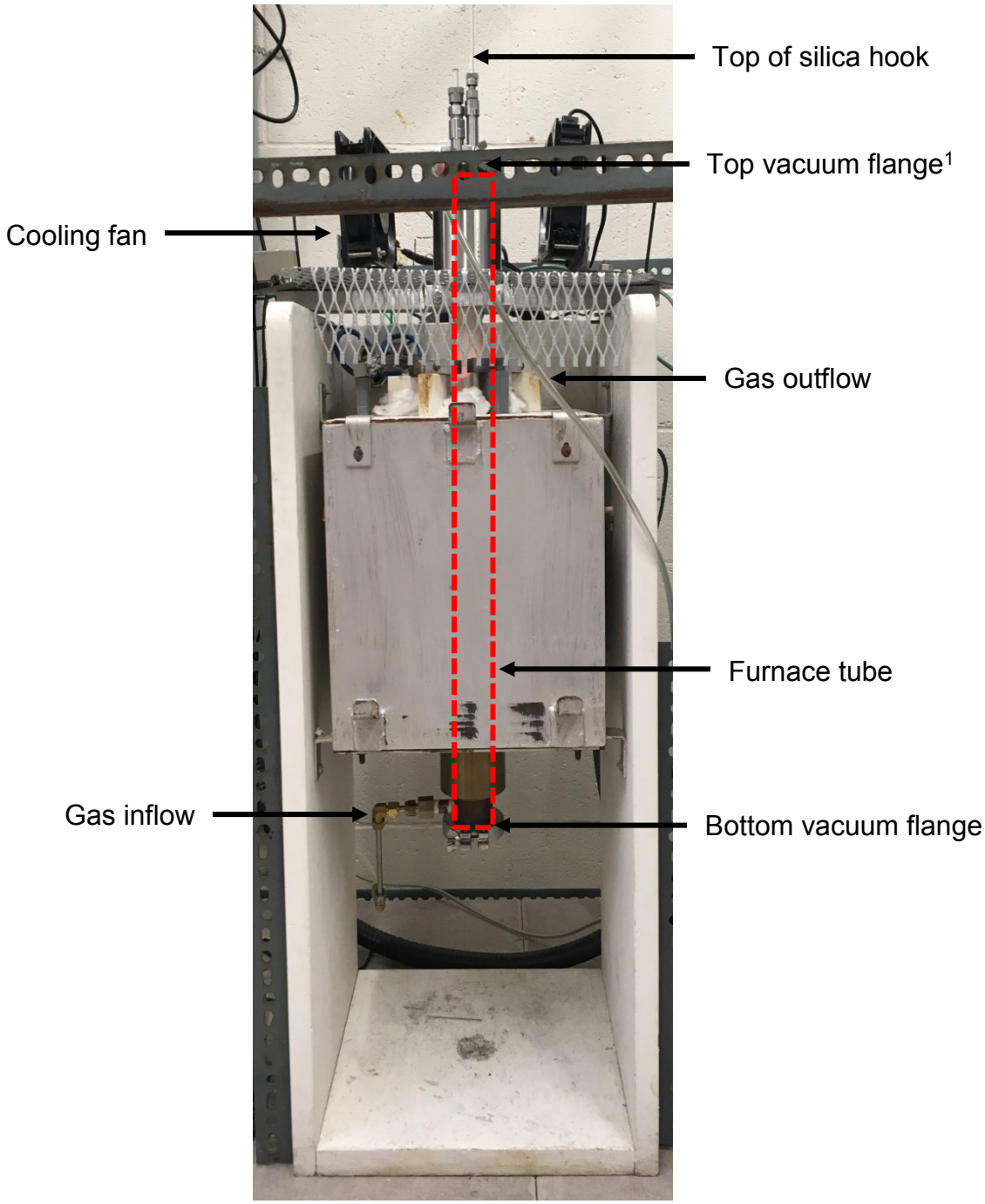

Figure 3.1. Picture of one of the Dalhousie vertical tube gas-mixing furnaces. Red dashed line indicates the position of the furnace tube. 1. Sealed top vacuum flange with swage-lock fitting to allow for gas-tight insertion of thermocouple and silica rod.

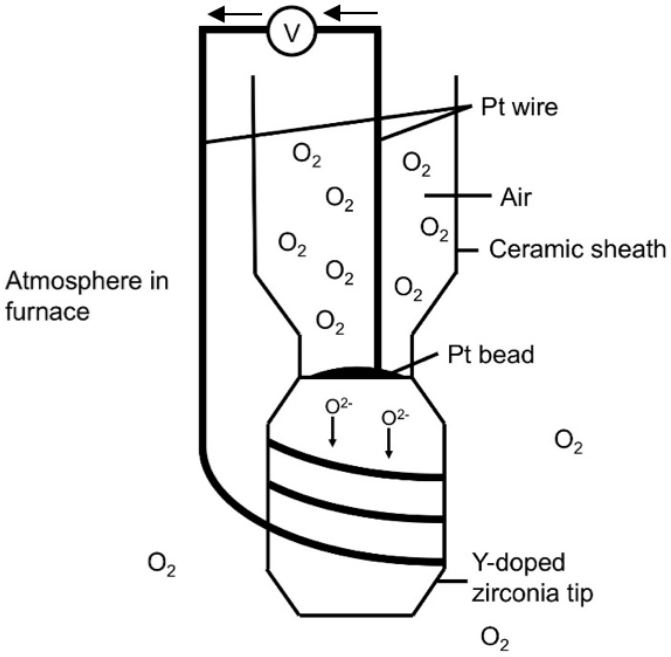

Figure 3.2. (a) Schematic of the Y-doped zirconia sensor showing the generation of electric potential by the oxygen gradient between the reference gas inside the sensor and the furnace atmosphere outside the sensor. Not to scale. (b) Photo of the sensor.

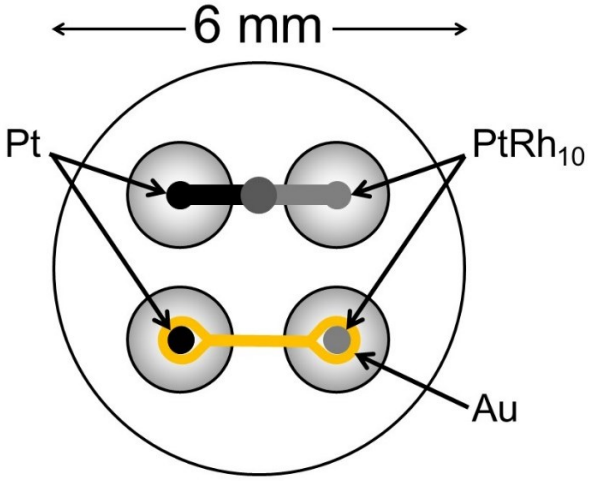

Figure 3.3. Schematic of the bottom view of the Au calibration experiment assembly. The large white circle depicts the alumina rod with 4 bore holes to prevent the wires from touching each other. The top set of Pt-$PtRh_{10}$ wires make up the thermocouple used during experiments. The bottom set of Pt-$PtRh_{10}$ wires connected by Au wire make up the Au wire circuit used in the temperature calibration experiment decribed in section 3.2.

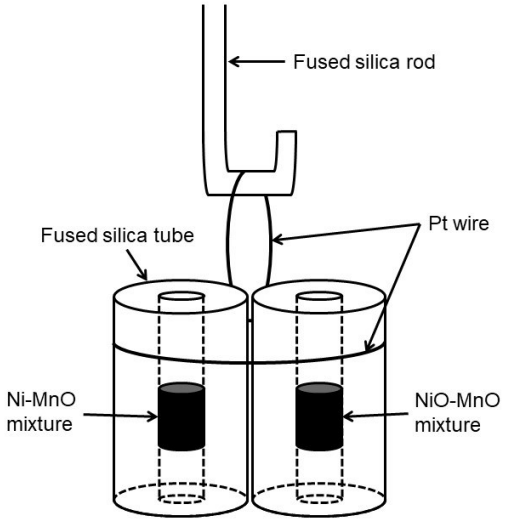

Figure 3.4. Schematic of the sliding sensor experiment assembly. Ni-MnO and NiO-MnO mixtures are cold-pressed into two thick-walled fused silica tubes that are held together by Pt wire to ensure they are suspended at the same height in the furnace during the experiment. The tubes are then suspended from a fused silica rod by Pt wire.

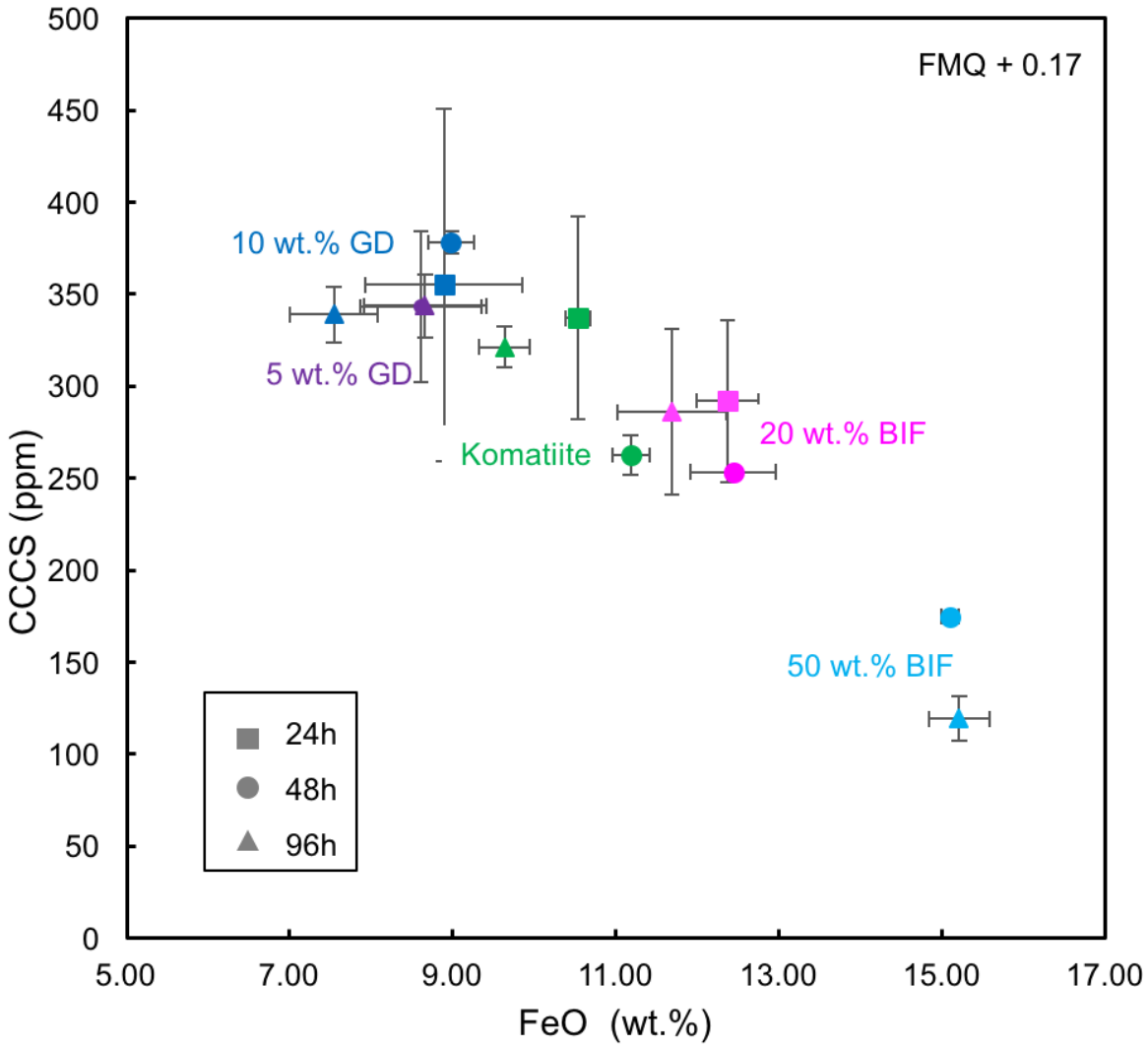

Figure 4.1.1. FeO vs CCCS of run product melt. Error bars represent 1 standard deviation; in some cases, the error bar is smaller than the size of the symbol. Square represent 24 h experiments; circles represent 48 h experiments; triangles represent 96 h experiments. Green indicates uncontaminated komatiite; pink indicates 20 wt.% BIF; cyan indicates 50 wt.% BIF; purple indicates 5 wt.% GD; blue represents 10 wt.% GD. The large error bars on the 24h 10 wt.% GD and K1 samples is due to difficulty finding areas of glass large enough for LA-ICPMS analysis.

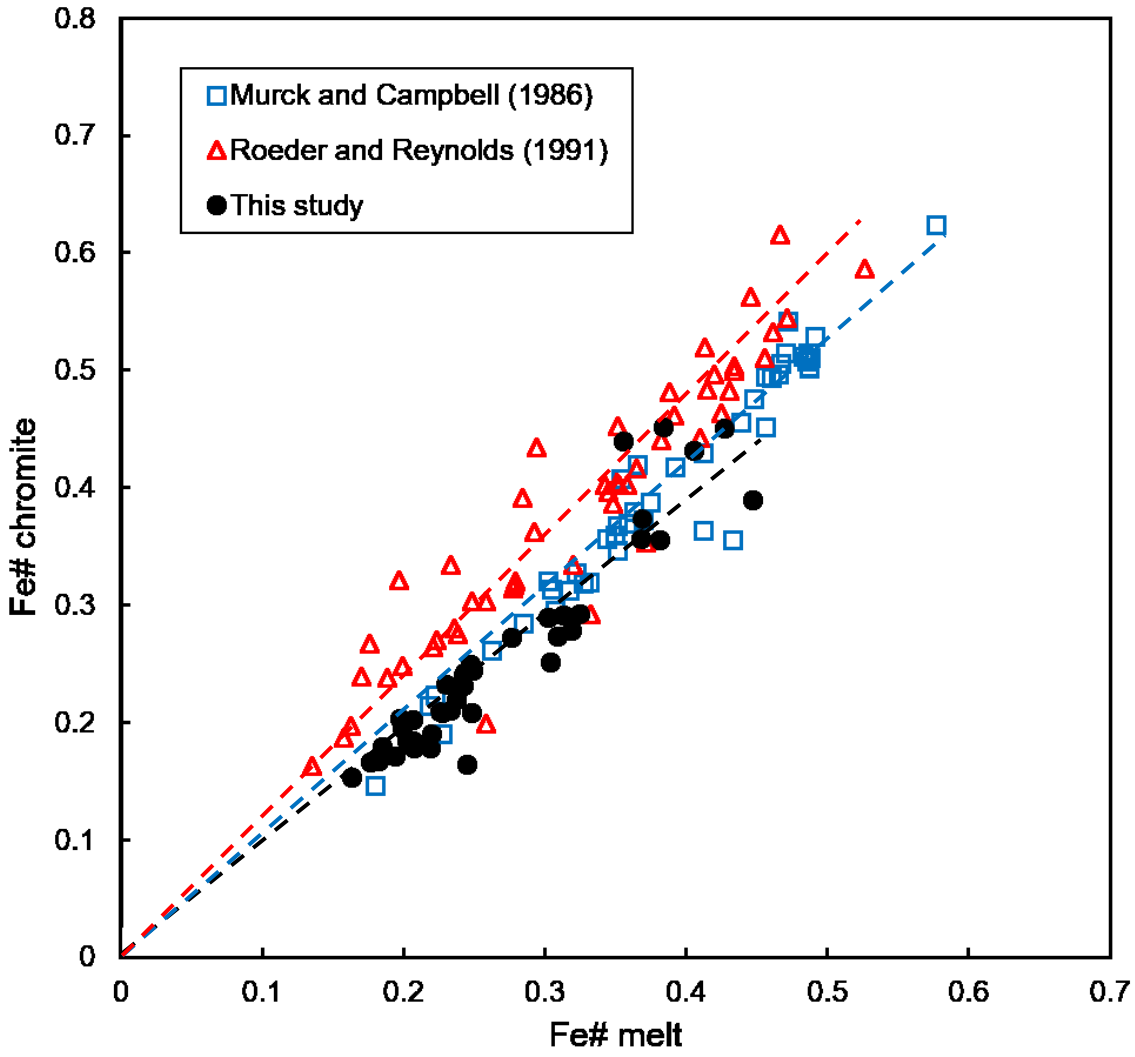

Figure 4.1.2. Fe# of melt vs. Fe# of chromites comparing data produced in this study with Murck and Campbell (1986) and Roeder and Reynolds (1991). The slopes of the unweighted best fit lines for the data from this study, Murck and Campbell (1986), and Roeder and Reynolds (1991) are 0.98±0.06, 1.05±0.04, and 1.18±0.05, respectively. The Fe^{2+} content of the melt was calculated using the calibration of Kress and Carmichael (1991) and the Fe^{2+} content of chromite was calculated from mineral stoichiometry after the method of Barnes and Roeder (2001).

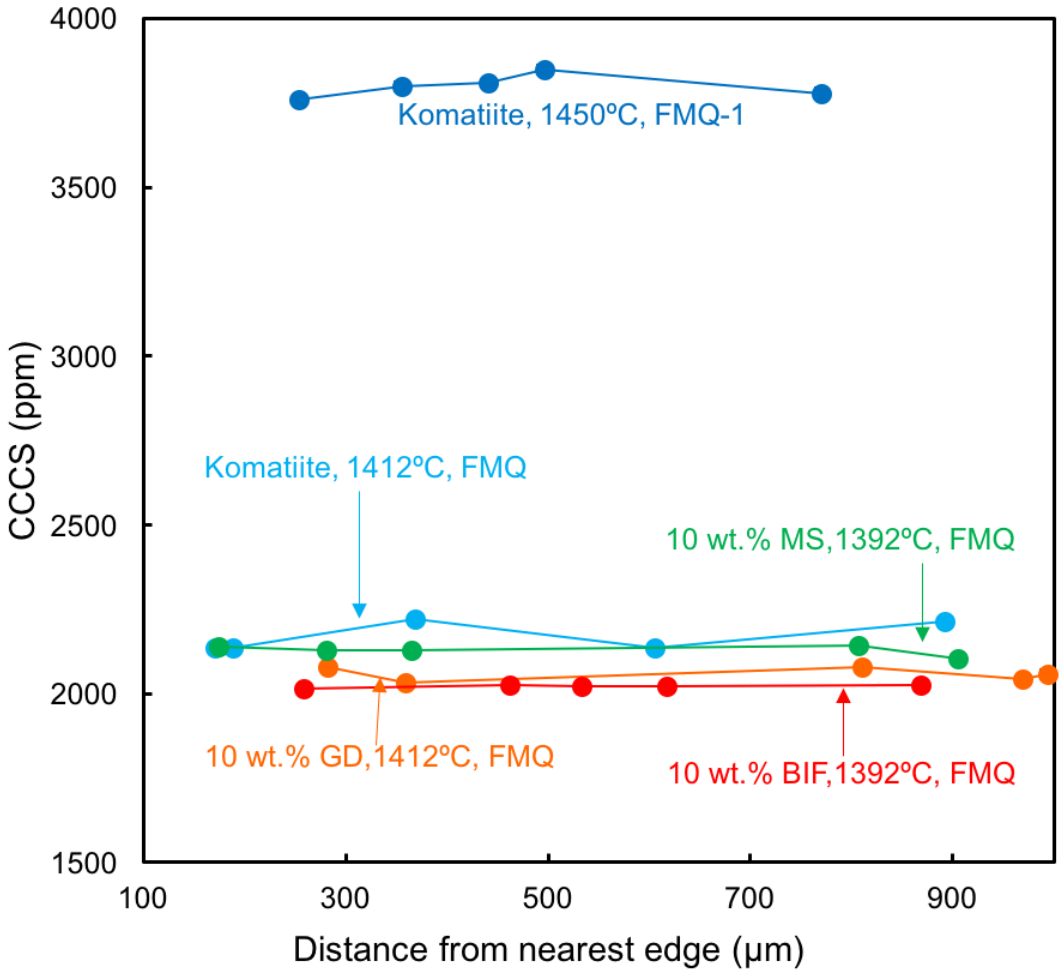

Figure 4.1.3. CCCS as a function of distance across glass beads produced in chromite solubility experiments. There is no systematic change in Cr content with increased distance from the edge of the sample, indicating that glass compositions are homogenous. Error bars represent 1 standard deviation and are often smaller than the symbols.

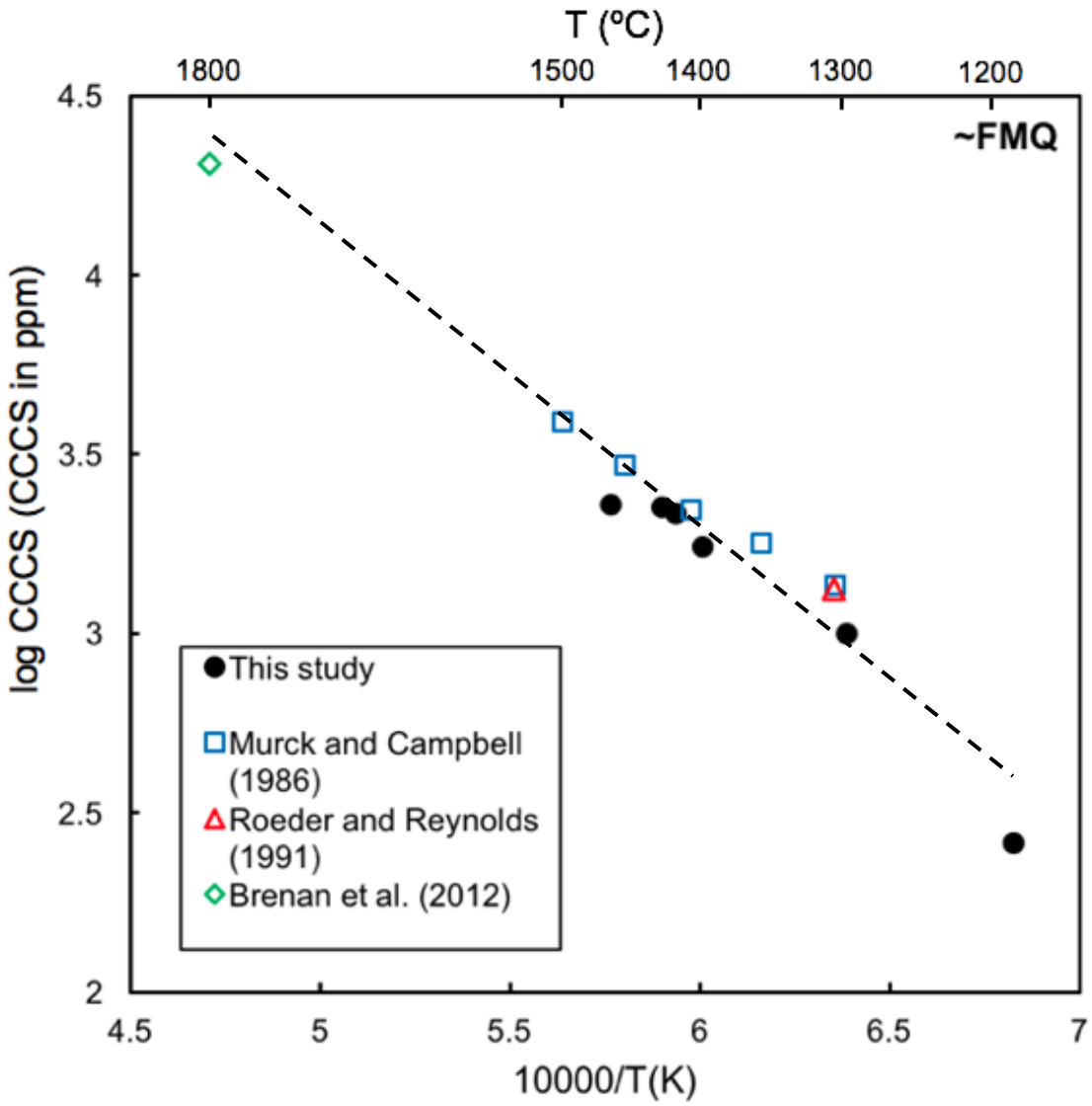

Figure 4.3.1. Log CCCS (CCCS in ppm) as a function of inverse absolute temperature. Data are for chromite solubility experiments involving komatiite compositions. Circles indicate data from this study, squares indicate data from Murck and Campbell (1986), triangles indicate data from Roeder and Reynolds (1991), and diamonds indicate data from Brenan et al. (2012). The equation of the unweighted best fit line is $y = -0.853(\pm0.055)x + 8.40(\pm0.33)$.

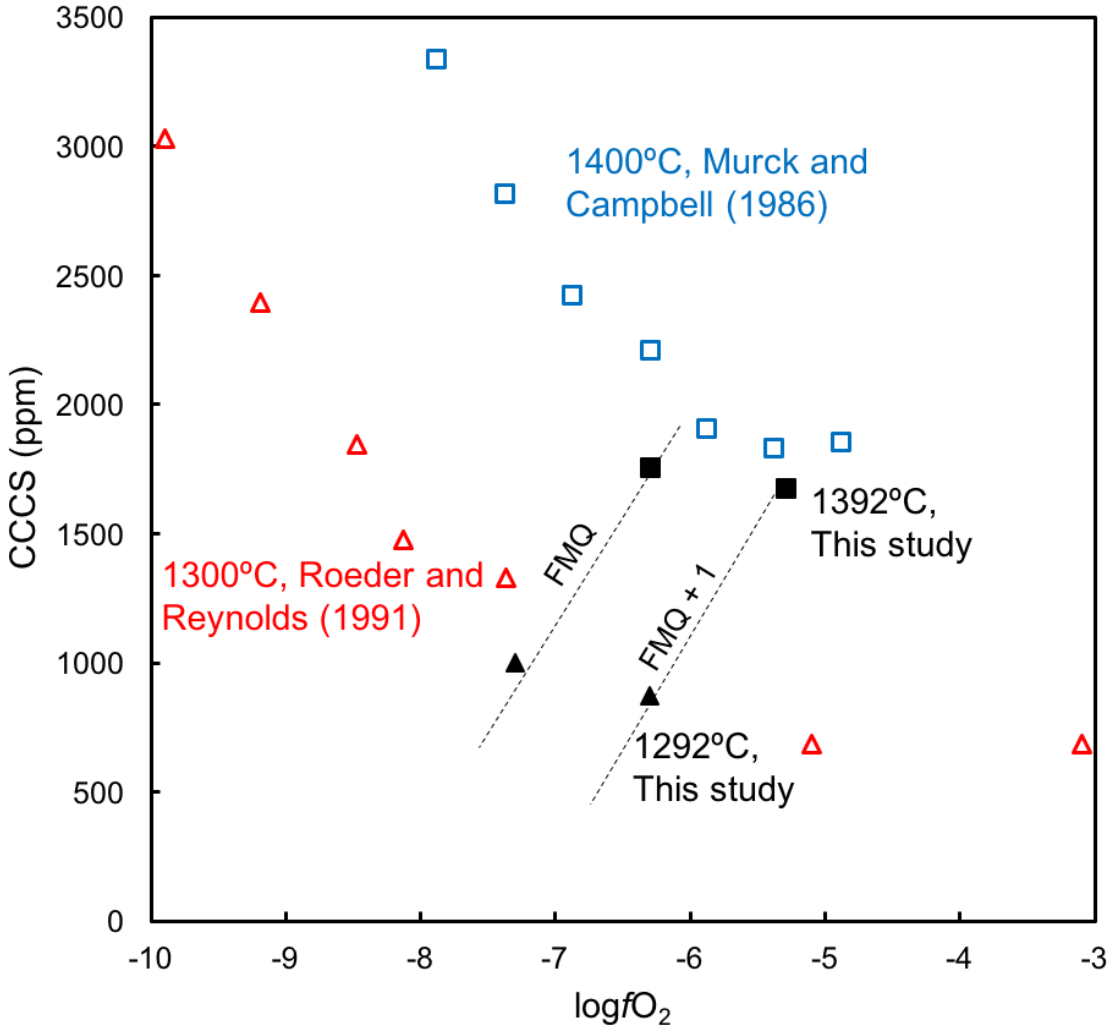

Figure 4.3.2. CCCS as a function of fO_2 for experiments involving komatiite compositions. Solid squares and triangles, indicate data at 1400ºC from Murck and Campbell (1986) and at 1300ºC from Roeder and Reynolds (1991) respectively. Open circles and triangles indicate data at 1292ºC and 1392ºC respectively from this study. The dashed line indicates the log fO_2 of the FMQ oxygen buffer at the temperatures indicated.

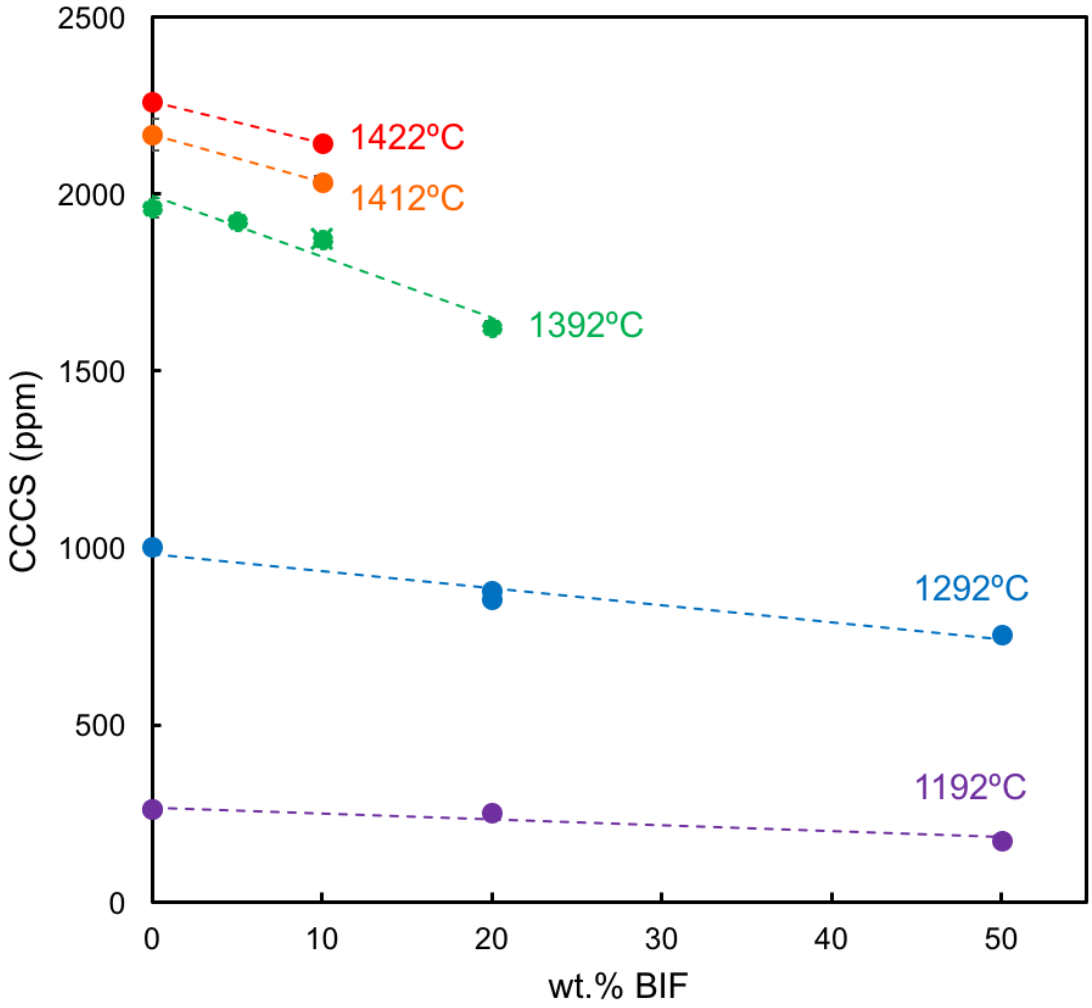

Figure 4.3.3. CCCS as a function of wt.% BIF added to experiments. Circles indicate experiments done using komatiite with 2187 ppm Cr; the X indicates an experiment that was doped with 1 wt.% synthetic chromite. All experiments were done at the FMQ oxygen buffer. Error bars indicate 1 standard deviation and are often smaller than the symbol.

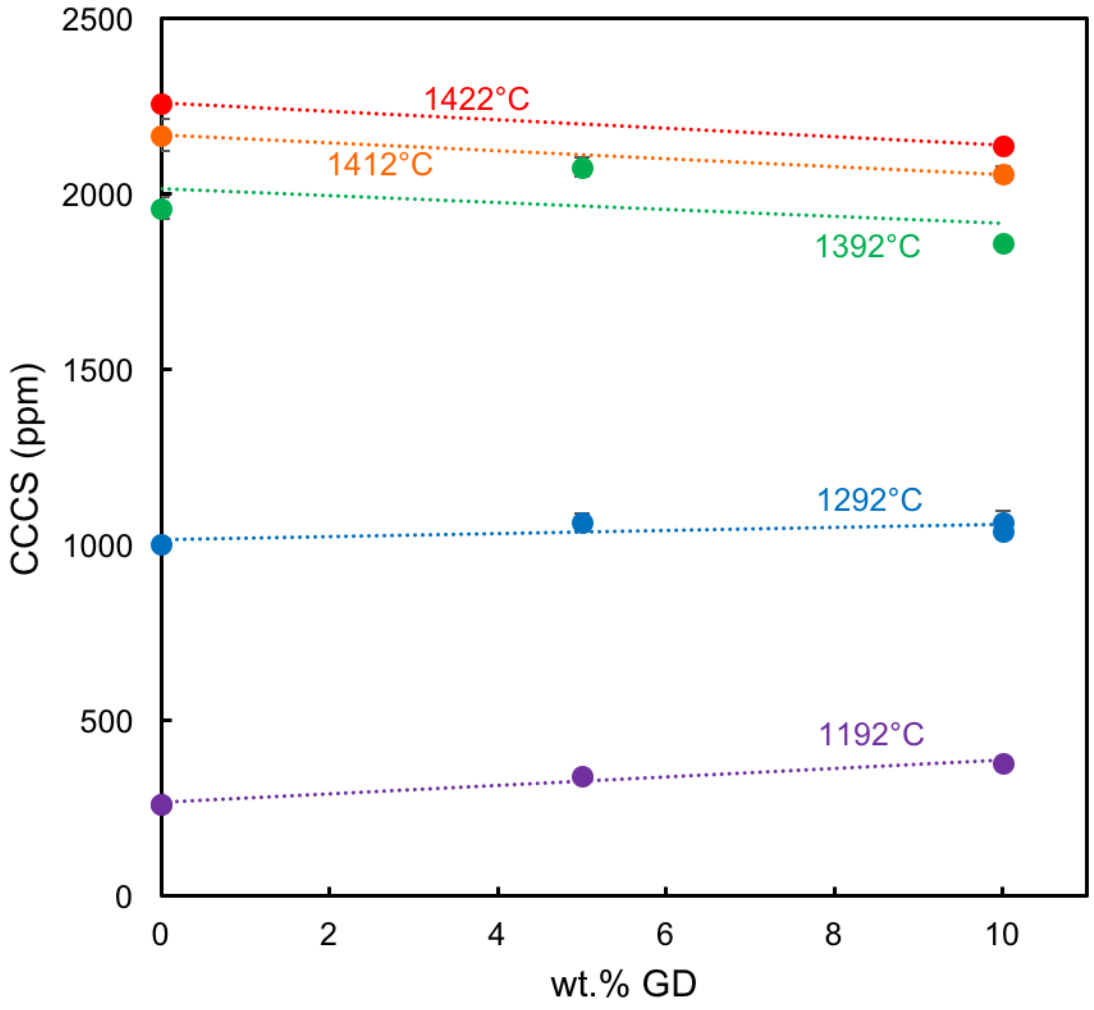

Figure 4.3.4. CCCS as a function of wt.% granodiorite added to experiments. All experiments done at the FMQ oxygen buffer. Error bars indicate 1 standard deviation and are often smaller than the symbol.

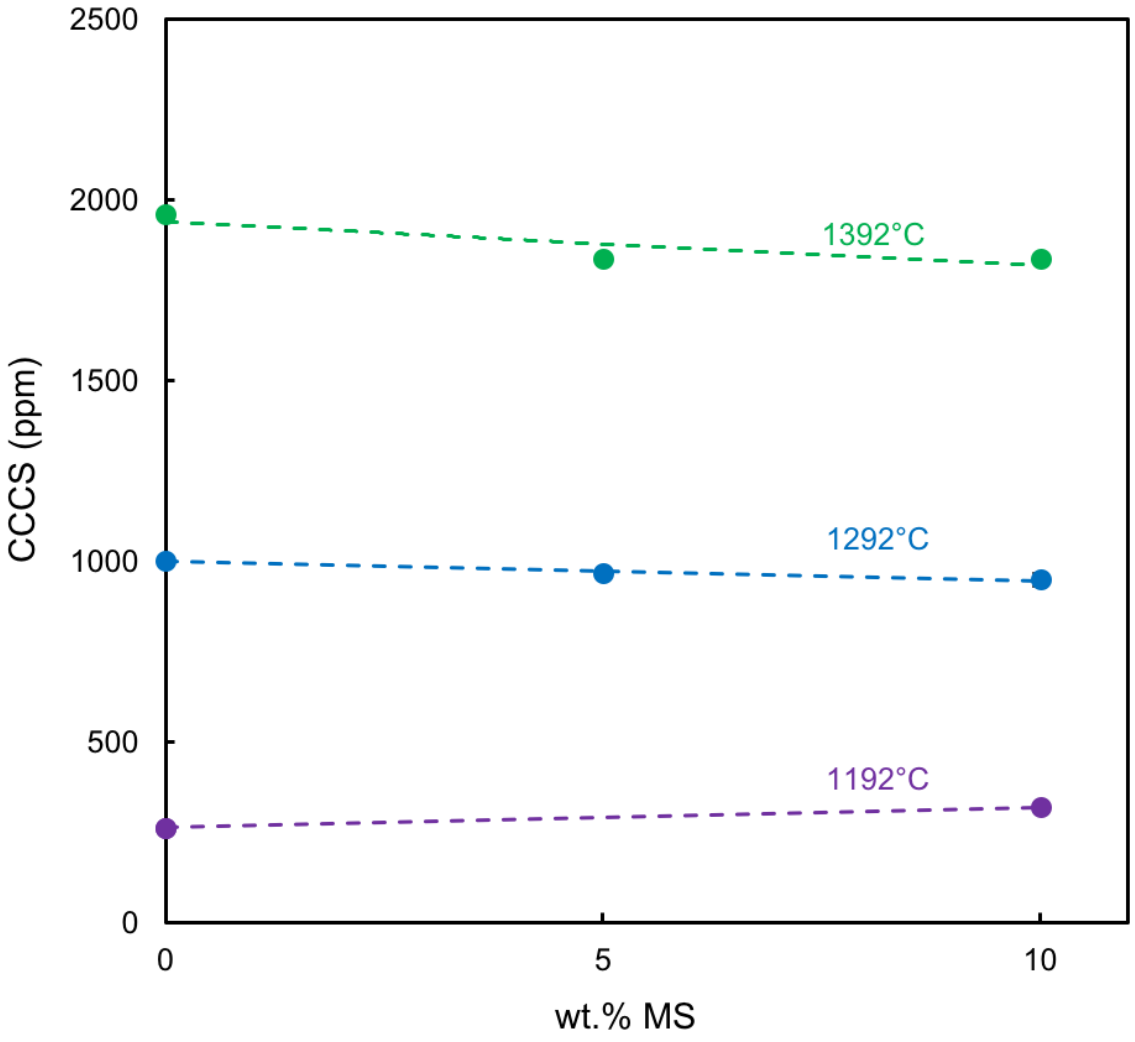

Figure 4.3.5. CCCS as a function of wt.% metasediment added to experiments. All experiments done at the FMQ oxygen buffer. Error bars indicate 1 standard deviation and are often smaller than the symbol.

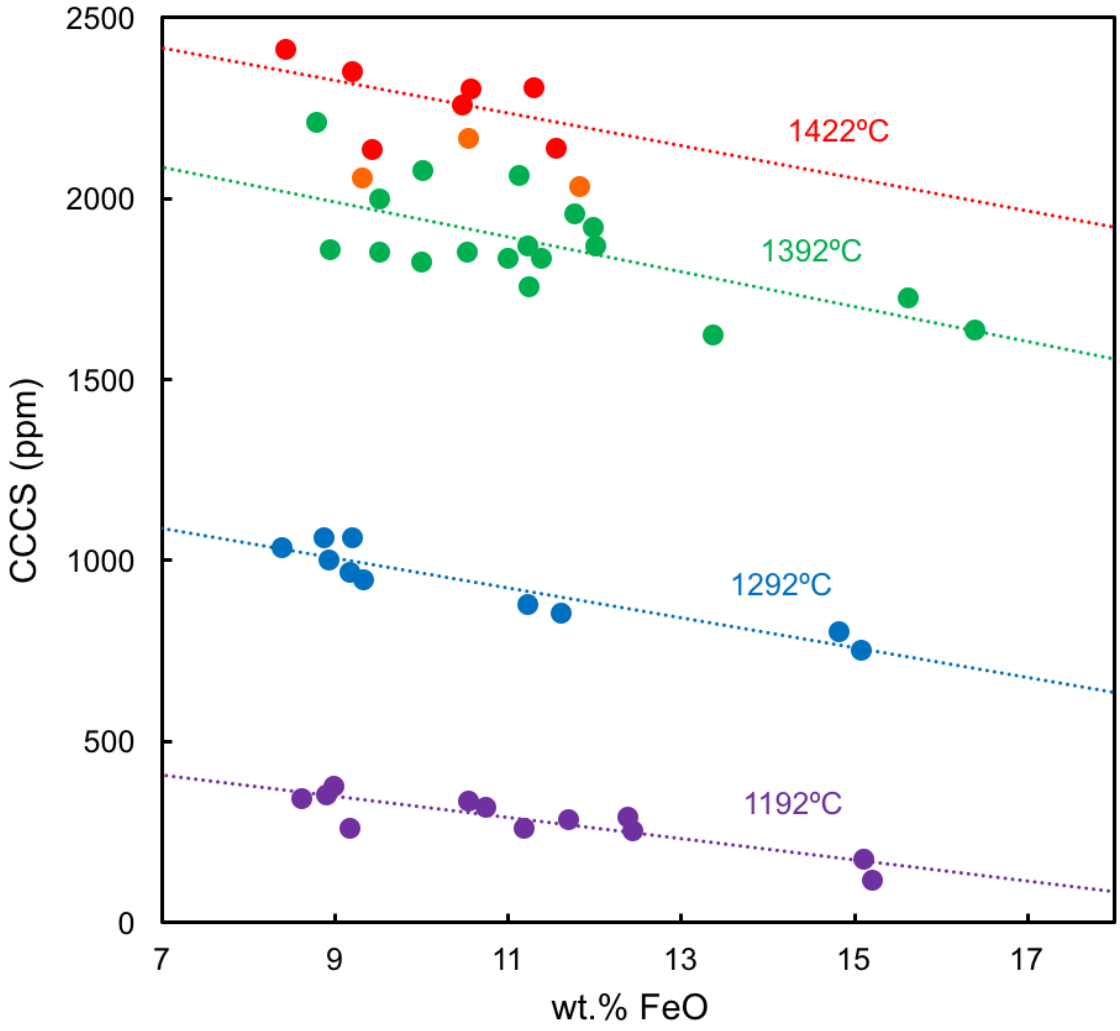

Figure 4.3.6. CCCS as a function of wt.% FeO of the melt. By considering mass balance, data was filtered to exclude any samples that had lost Fe to the Pt loop. Purple = 1192ºC, blue = 1292ºC, green = 1392ºC, orange = 1412ºC, and red = 1422ºC. All experiments done at the FMQ oxygen buffer. Dotted lines indicate lines of best fit through the data set at each temperature.

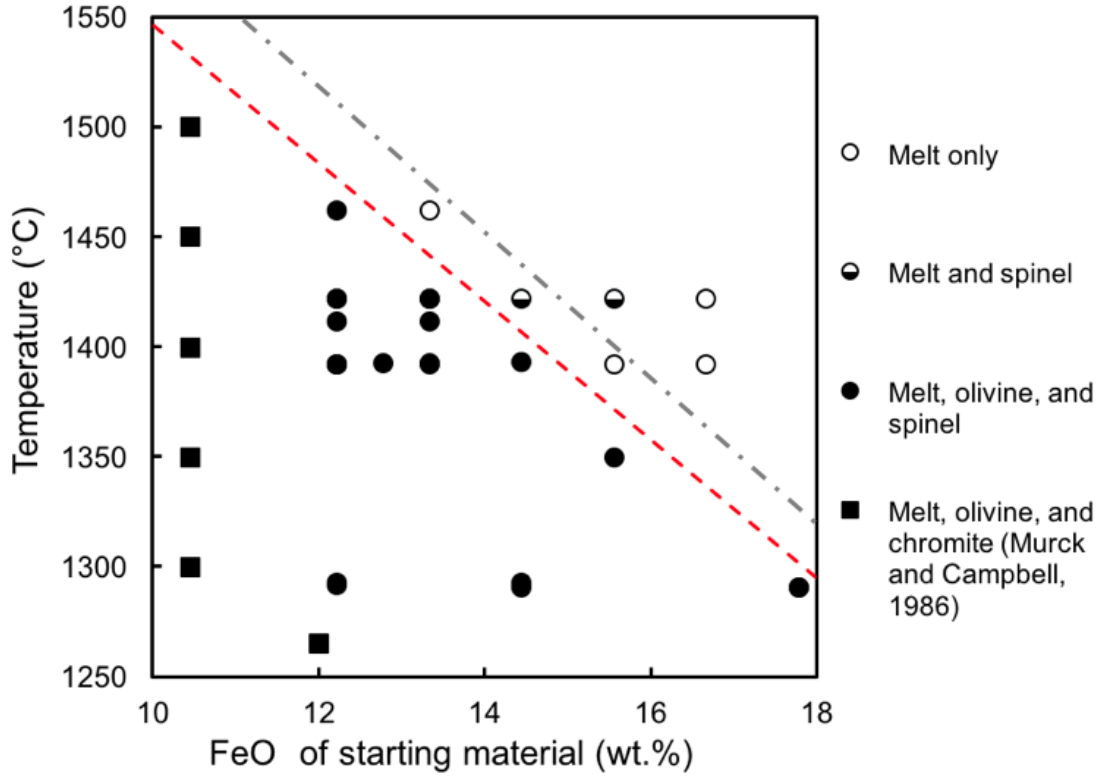

Figure 4.4.1. Phase equilibria for komatiite with increasing FeO content. Open circles indicate experiments with melt only; half-open circles indicate experiments with melt + chromite; solid circles indicate experiments with melt + olivine + chromite. The dashed red line indicates the approximate liquidus inferred from experimental phase equilibria; the grey dashed line indicates the liquidus modelled using MELTS. Dataset includes komatiite with 2187 ppm and komatiite doped with 1 wt.% chromite.

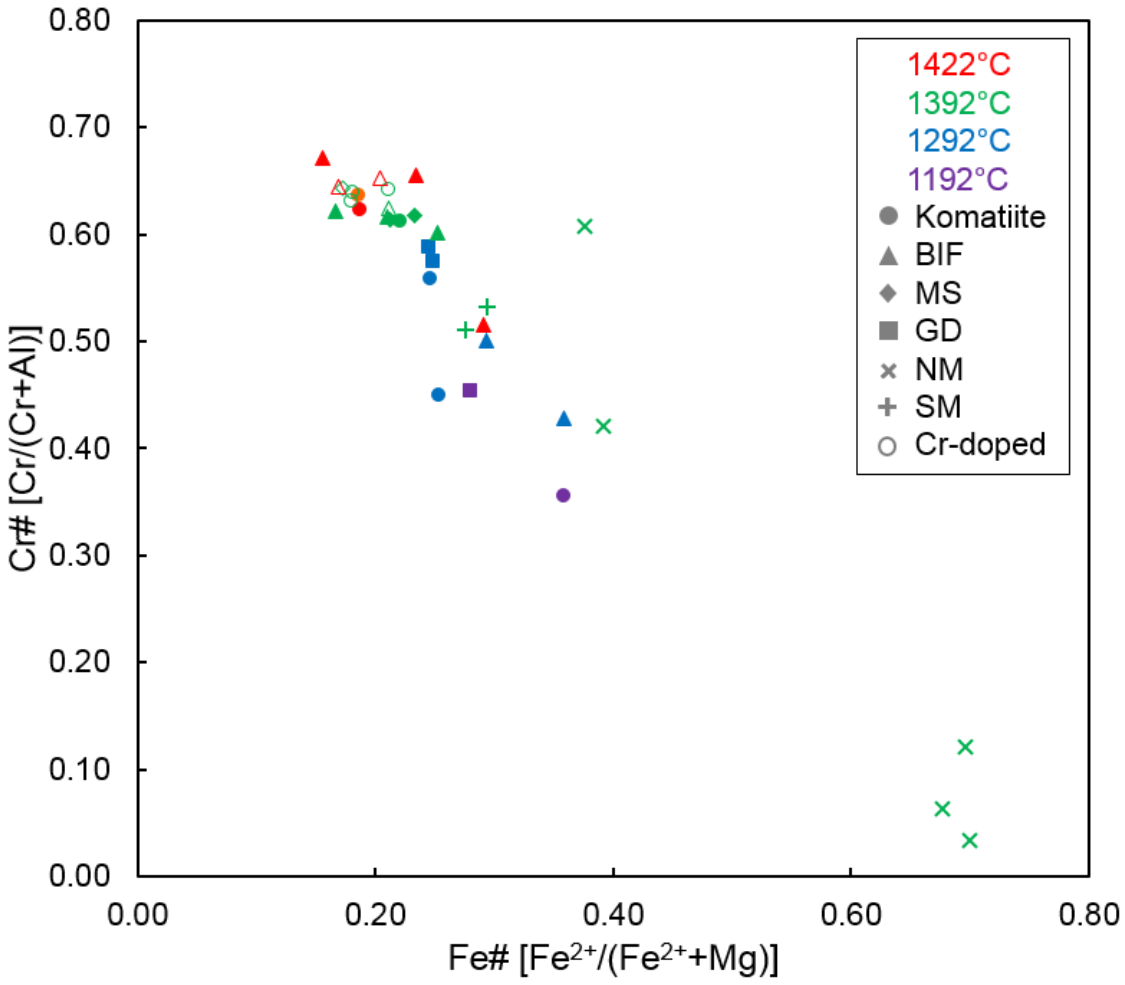

Figure 4.5.1. Summary of Fe# vs. Cr# for experimental chromite. Symbols are explained in the legend; colour indicates temperature, shape indicates contaminant composition, and open symbols indicate experiments that were doped with synthetic chromite.

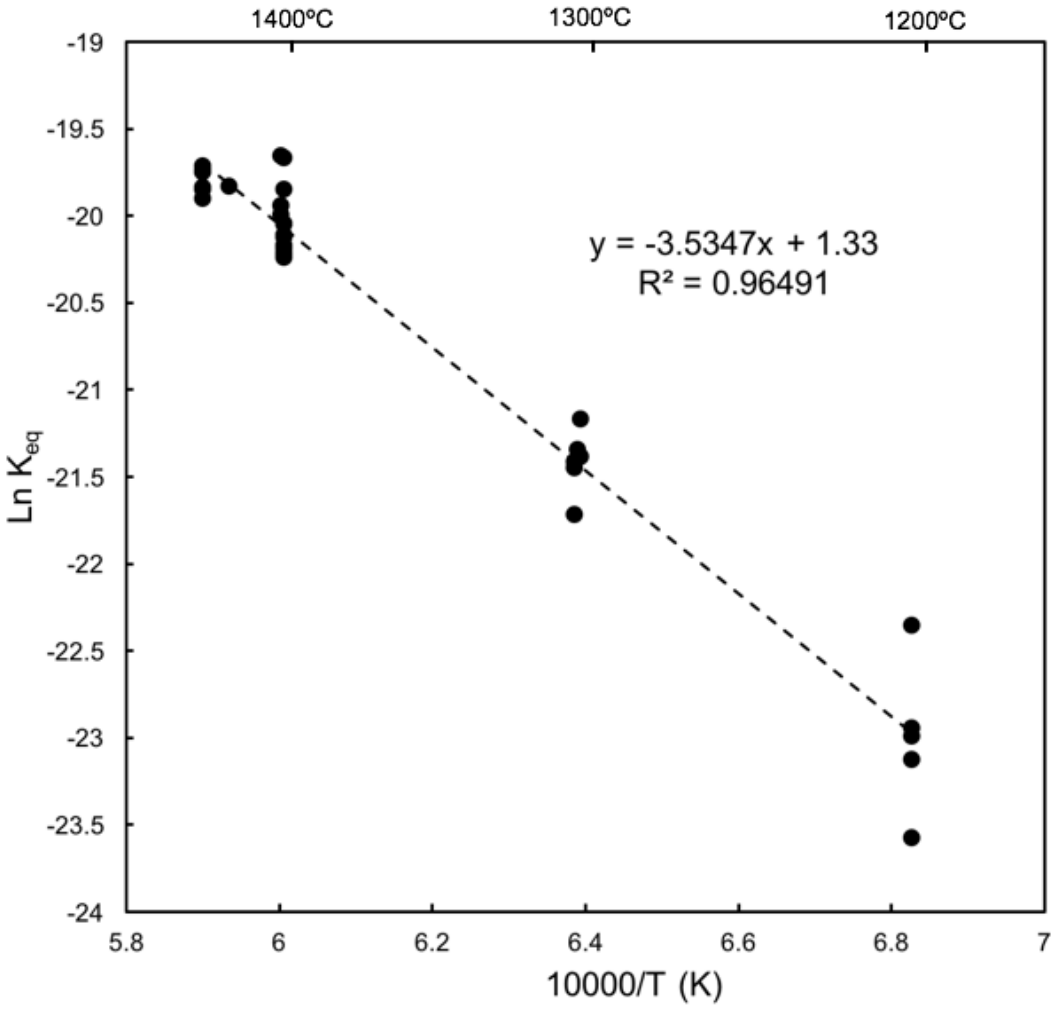

Figure 5.1. Ln(K_{eq}) as a function of 10000/T, where T is in K. The slope of the best fit line (R^2 = 0.96491) through the data is -3.5347±0.1211, which corresponds to the ΔH/R term in Equation 3.6. The intercept of the best fit line through the data is 1.33±0.75, which corresponds to the ΔS/R term in Equation 3.6.

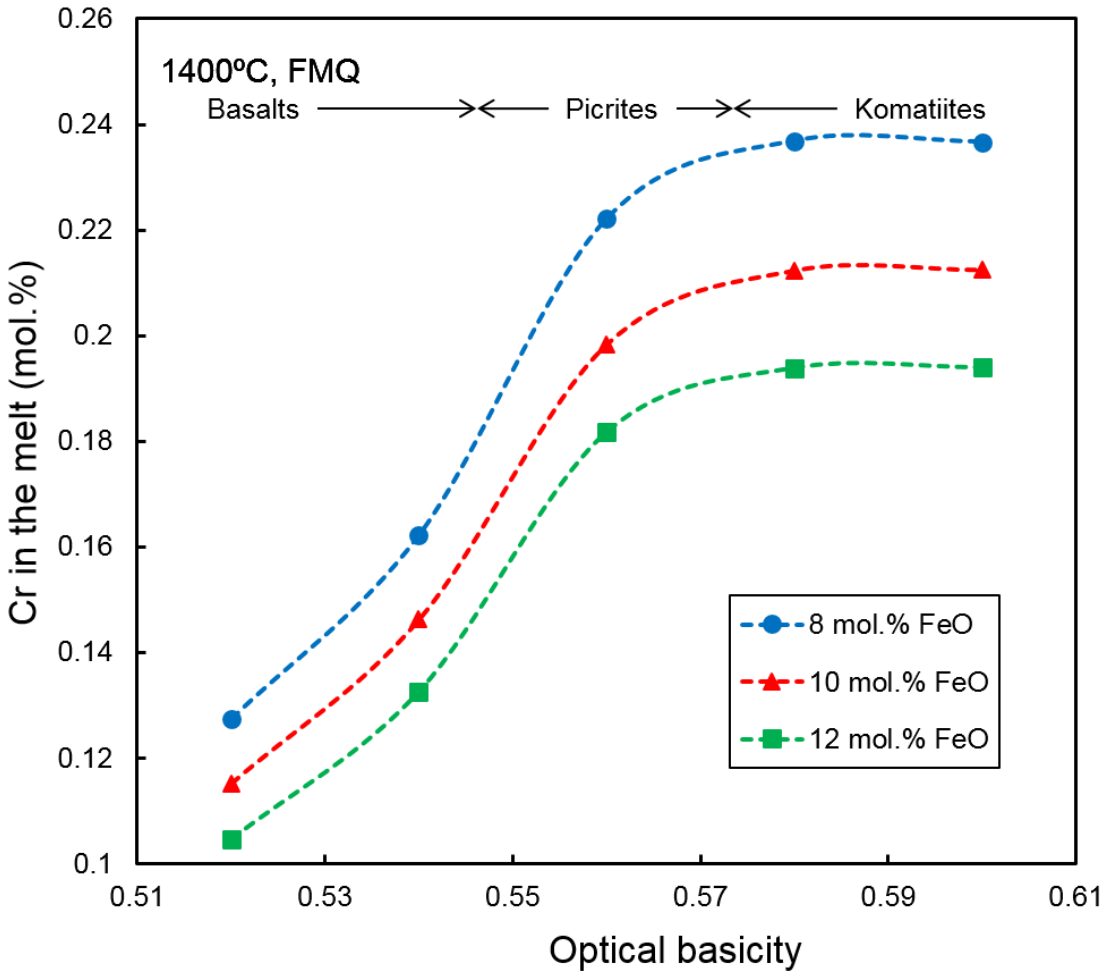

Figure 5.2. Variation of Cr in the melt with OB for melts with fixed FeO content at 1400°C and FMQ. Blue circles, red triangles, and green squares indicate melts with 8, 10, and 12 mol.% FeO, respectively. Dotted lines indicate unweighted best fit polynomial lines.

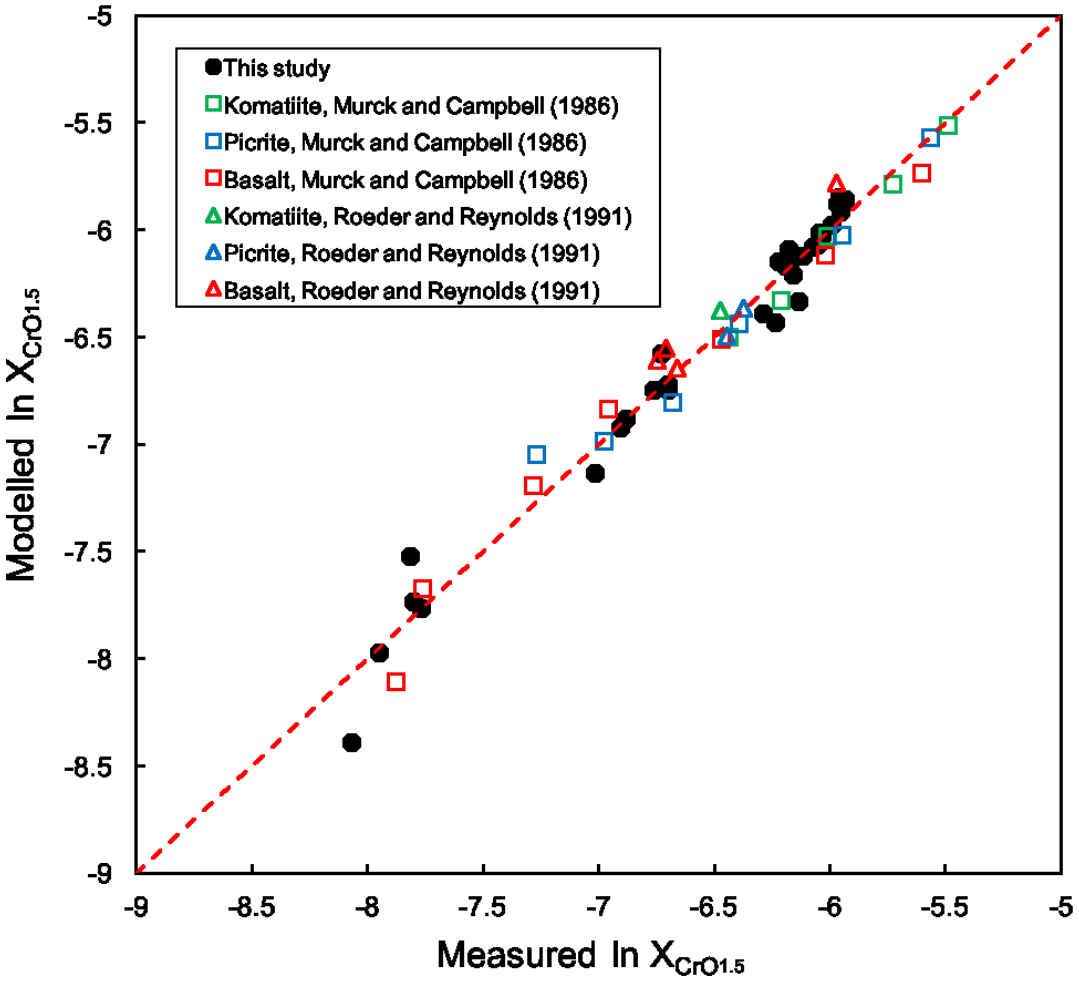

Figure 5.3. Comparison between values of CCCS measured by experiments and those calculated using Equation 5.10. Data from this study (solid black circles) were used to construct the model, which was tested against the results of Murck and Campbell (1986); open squares) and Roeder and Reynolds (1991; open triangles). Green, blue, and red indicate komatiitic, picritic, and basaltic compositions, respectively.

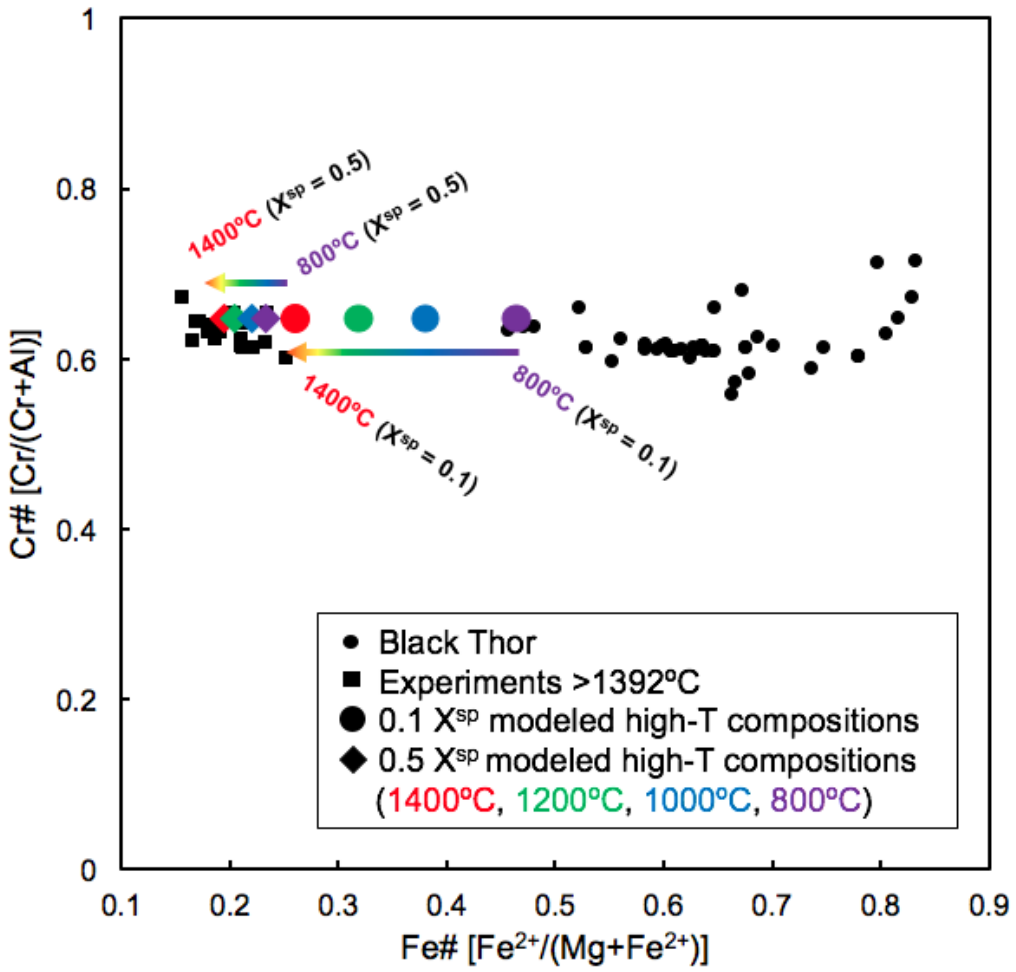

Figure 5.4. Plot of Cr# as a function of Fe# comparing the compositions of chromite from the Black Thor deposit (filled circles), chromites produced in high temperature experiments (this study, T>1392ºC, FMQ buffer) and calculated compositions based on olivine-spinel thermometry (O'Neill and Wall, 1987), assuming the mass fraction of spinel (X^{sp}) in the chromite-silicate assemblage is 0.1 and 0.5. The estimated average mass fraction of spinel of the Black Thor samples is 0.14.

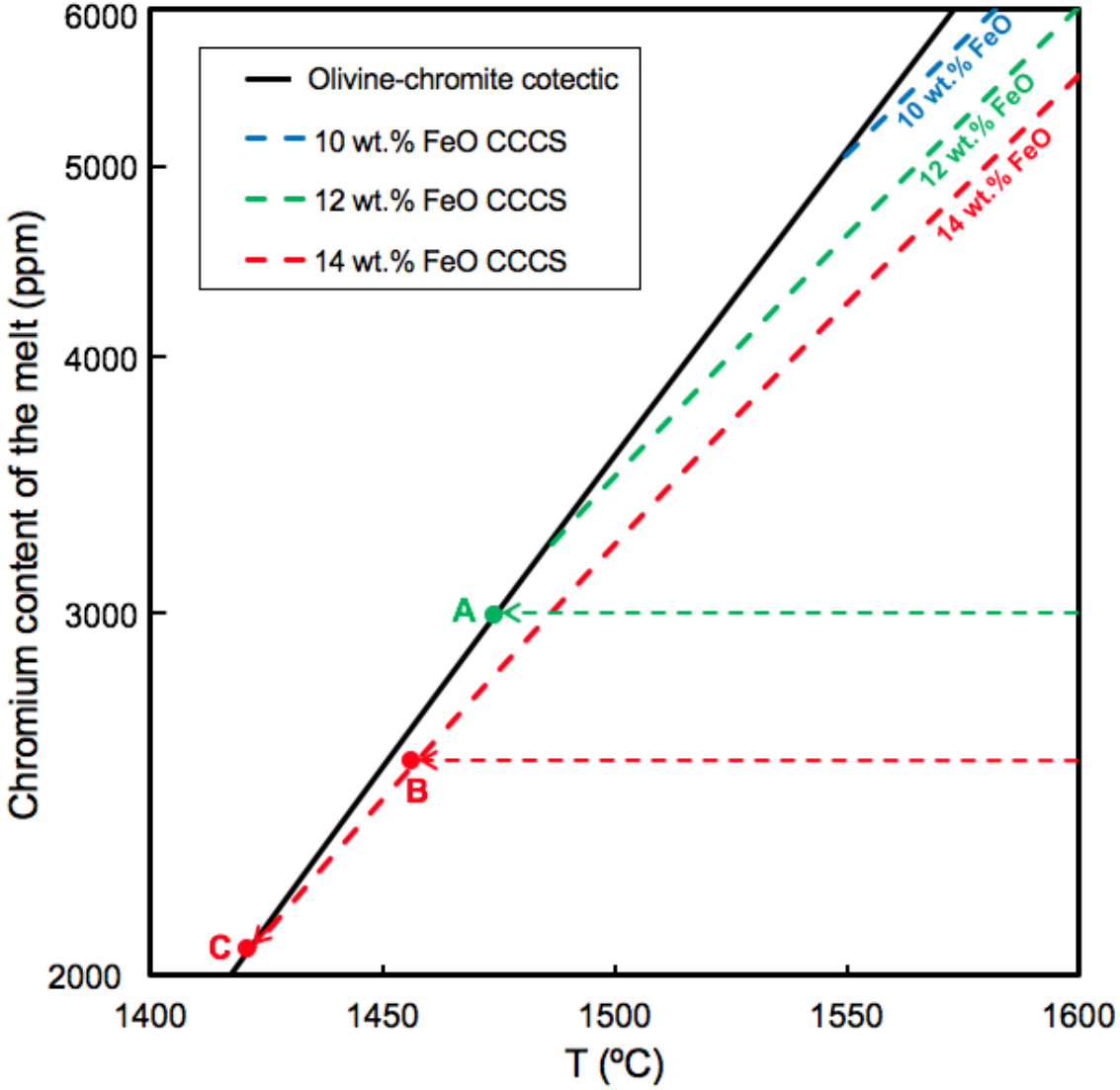

Figure 5.5. Plot of the CCCS (ppm) as a function of temperature for silicate liquids crystallizing chromite-only (dashed curves) or olivine and chromite (solid black curve). The dashed curves are labelled according to the FeO content of the melt. An uncontaminated komatiite melt with 3000 ppm Cr and 12 wt.% FeO (green dotted line) would be saturated in chromite and olivine simultaneously (point A). A komatiite melt contaminated with 16 wt.% BIF with 2520 ppm Cr and 14 wt.% FeO (red dotted line) would be saturated in chromite first (point B), and crystallize chromite alone until point C, at which point olivine and chromite would co-crystallize.

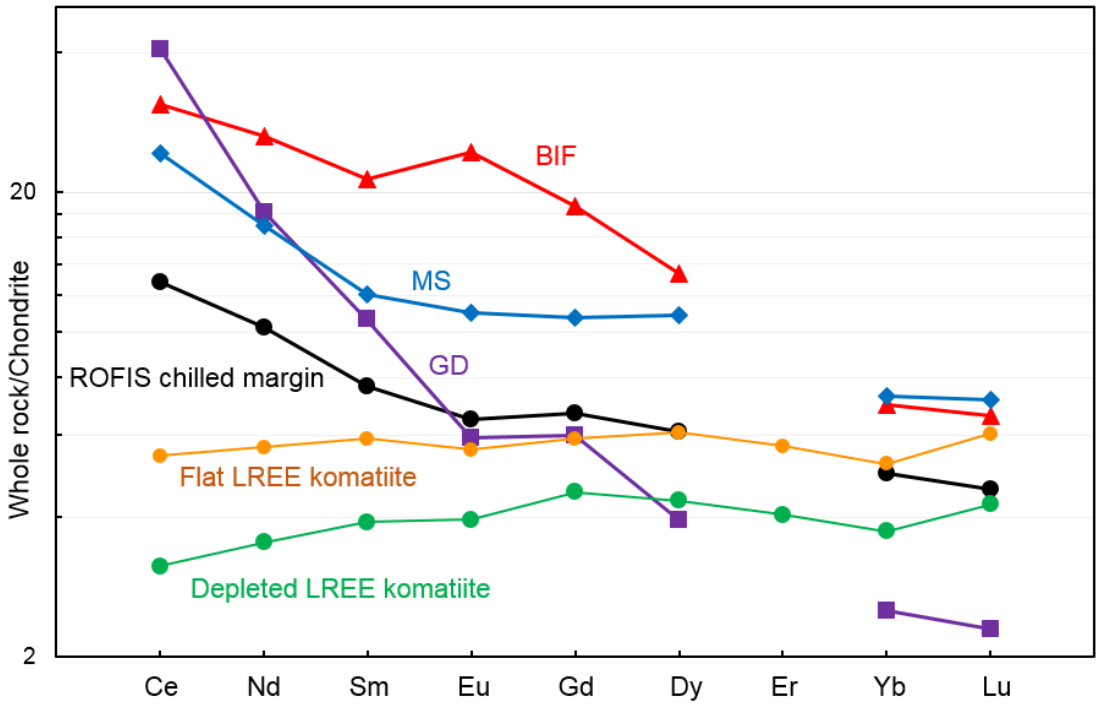

Figure 5.6. Chondrite-normalized REE concentration of typical Munro Township komatiites, ROFIS chilled margin, and country rock compositions. Black symbols indicate the ROFIS chilled margin composition from Azar (2010). Orange and green symbols indicate data from Arth et al. (1977) for pyroxenitic and peridotitic Munro Township komatiites. Red, blue, and purple symbols indicate BIF, granodiorite, and metasediment compositions from Azar (2010).

APPENDIX A: Analyses of Black Thor samples

Table A1. Summary of Black Thor chromite chemistry. Analytical conditions are summarized in the footnote.

Sample ID	SiO_2 (wt.%)	TiO_2 (wt.%)	Al_2O_3 (wt.%)	Cr_2O_3 (wt.%)	FeO (wt.%)	MnO (wt.%)	MgO (wt.%)	Total	Fe#	Cr/3+	Fe/3+	Al/3+	Ti/4O*
221-2-1a	0.00	0.61	18.41	43.95	26.75	0.41	8.28	98.42	0.60	0.58	0.07	0.36	0.015
221-2-1b	0.01	0.61	18.45	43.22	27.06	0.39	8.34	98.08	0.60	0.57	0.07	0.36	0.015
221-2-1c	0.01	0.66	18.57	43.55	27.34	0.42	7.92	98.47	0.62	0.57	0.07	0.36	0.016
221-2-2a	0.02	0.57	18.06	46.56	21.37	0.35	11.40	98.33	0.46	0.60	0.06	0.35	0.014
221-2-2b	0.01	0.52	17.86	46.93	21.50	0.35	11.03	98.21	0.47	0.60	0.05	0.34	0.013
221-2-2c	0.00	0.53	17.64	46.19	21.85	0.36	10.74	97.30	0.48	0.60	0.06	0.34	0.013
221-2-3a	0.01	0.50	18.37	43.69	27.54	0.43	7.40	97.94	0.64	0.58	0.06	0.36	0.012
221-2-4a	0.01	0.46	16.55	47.76	23.22	0.39	9.83	98.22	0.52	0.62	0.06	0.32	0.011
221-2-4b	0.00	0.44	18.64	44.05	24.40	0.38	9.73	97.64	0.53	0.57	0.07	0.36	0.011
221-2-5a	0.00	0.58	18.67	44.66	26.42	0.42	8.24	99.00	0.60	0.58	0.06	0.36	0.014
221-2-5b	0.02	0.58	18.78	43.77	26.98	0.42	8.11	98.66	0.61	0.57	0.06	0.37	0.014
264-4-1a	0.14	0.83	19.58	38.99	30.81	0.45	6.85	97.64	0.67	0.52	0.09	0.39	0.021
264-4-1b	0.01	0.72	18.58	38.47	32.19	0.44	6.47	96.88	0.68	0.52	0.11	0.37	0.018
264-4-1c	0.00	0.57	20.58	38.86	30.58	0.44	6.92	97.96	0.66	0.51	0.09	0.40	0.014
264-4-2b	0.02	0.53	18.03	38.50	33.55	0.48	5.21	96.32	0.74	0.52	0.11	0.37	0.013
264-4-2c	0.03	0.50	16.50	38.94	35.21	0.47	4.94	96.58	0.75	0.53	0.13	0.34	0.013
264-4-3a	0.03	0.70	17.94	41.45	29.98	0.44	7.18	97.72	0.65	0.55	0.09	0.36	0.017
264-4-3b	0.00	0.72	18.32	42.34	29.45	0.46	7.30	98.60	0.64	0.56	0.08	0.36	0.018
264-4-4a	0.00	0.69	17.30	39.19	35.55	0.51	4.37	97.61	0.78	0.53	0.11	0.35	0.018
251-2-1a	0.11	0.73	18.15	43.74	26.86	0.41	8.67	98.67	0.58	0.57	0.07	0.35	0.018
251-2-1b	0.01	0.67	17.66	42.17	31.10	0.51	6.02	98.12	0.70	0.56	0.08	0.35	0.017
251-2-1c	0.01	0.65	18.28	42.98	27.94	0.46	7.61	97.92	0.63	0.57	0.07	0.36	0.016
251-2-2a	0.01	0.63	15.76	45.66	28.54	0.46	7.11	98.17	0.65	0.61	0.07	0.31	0.016
251-2-2b	0.00	0.58	14.81	46.79	29.27	0.47	6.56	98.48	0.67	0.63	0.07	0.30	0.015

Sample ID	SiO_2 (wt.%)	TiO_2 (wt.%)	Al_2O_3 (wt.%)	Cr_2O_3 (wt.%)	FeO (wt.%)	MnO (wt.%)	MgO (wt.%)	Total	Fe#	Cr/3+	Fe/3+	Al/3+	Ti/4O*
251-2-2c	0.01	0.75	18.39	42.66	28.90	0.45	7.45	98.62	0.64	0.56	0.08	0.36	0.018
251-2-3a	0.00	0.63	18.61	43.03	28.28	0.44	8.10	99.10	0.61	0.56	0.08	0.36	0.015
251-2-3b	0.02	0.63	18.89	42.45	28.98	0.44	7.78	99.19	0.63	0.55	0.08	0.37	0.015
251-2-3c	0.01	0.57	18.47	43.03	29.17	0.46	7.63	99.33	0.63	0.56	0.08	0.36	0.014
202.5-1a	0.04	0.37	13.67	45.37	33.51	0.67	3.02	96.66	0.84	0.64	0.08	0.29	0.010
202.5-1b	0.12	0.50	12.58	44.94	35.55	0.73	2.63	97.05	0.86	0.64	0.10	0.27	0.013
202.5-1c	0.01	0.95	0.23	23.94	68.54	0.48	0.58	94.74	0.97	0.37	0.62	0.01	0.027
202.5-2a	0.11	1.48	0.62	40.75	50.70	0.78	1.00	95.43	0.94	0.64	0.34	0.01	0.042
202.5-2b	0.27	0.65	4.56	43.59	44.70	0.82	1.49	96.09	0.92	0.65	0.25	0.10	0.018
202.5-2c	0.03	1.39	0.72	40.56	50.69	0.79	0.96	95.13	0.95	0.64	0.35	0.02	0.040
202.5-4a	0.05	0.62	12.08	45.27	35.30	0.71	2.49	96.51	0.87	0.65	0.10	0.26	0.016
202.5-4b	0.05	1.34	0.46	38.41	52.66	0.81	0.85	94.57	0.95	0.61	0.38	0.01	0.039
202.5-4c	0.04	0.35	0.08	9.57	81.31	0.17	0.33	91.85	0.98	0.15	0.85	0.00	0.010
202.5-5a	0.09	0.30	12.68	46.87	33.59	0.52	3.89	97.93	0.80	0.65	0.09	0.26	0.008
202.5-5b	0.01	0.56	0.12	17.58	75.81	0.34	0.42	94.84	0.98	0.27	0.73	0.00	0.016
202.5-5c	0.03	0.82	0.24	26.13	66.10	0.53	0.58	94.43	0.97	0.41	0.59	0.01	0.024
209-1-2a	0.01	0.39	18.57	45.72	24.79	0.44	9.10	99.01	0.56	0.59	0.06	0.36	0.009
209-1-2b	0.01	0.38	19.14	44.92	25.64	0.45	8.65	99.19	0.58	0.58	0.06	0.37	0.009
209-1-2c	0.10	0.37	19.97	44.13	25.11	0.42	9.37	99.45	0.55	0.56	0.06	0.38	0.009
209-1-1a	0.02	0.50	17.57	43.62	29.93	0.50	6.30	98.45	0.69	0.58	0.07	0.35	0.013
209-1-1b	0.00	0.51	18.34	43.19	29.67	0.49	6.61	98.80	0.68	0.57	0.07	0.36	0.013
209.5-1a	0.00	1.31	0.48	34.04	57.82	0.65	0.74	95.04	0.96	0.53	0.45	0.01	0.038
209.5-1b	0.04	0.42	14.70	44.59	33.75	0.64	2.74	96.89	0.86	0.62	0.07	0.31	0.011
209.5-1c	0.05	1.40	0.47	36.28	55.08	0.69	0.81	94.78	0.95	0.57	0.42	0.01	0.040
209.5-2a	0.02	0.98	0.24	23.13	68.73	0.43	0.54	94.07	0.97	0.36	0.63	0.01	0.028
209.5-2b	0.05	0.45	13.81	42.35	36.83	0.54	3.29	97.31	0.83	0.59	0.12	0.29	0.012
209.5-2c	0.22	0.51	16.10	40.77	35.76	0.53	3.82	97.70	0.80	0.56	0.11	0.33	0.013

Sample ID	SiO_2 (wt.%)	TiO_2 (wt.%)	Al_2O_3 (wt.%)	Cr_2O_3 (wt.%)	FeO (wt.%)	MnO (wt.%)	MgO (wt.%)	Total	Fe#	Cr/3+	Fe/3+	Al/3+	Ti/4O*
209.5-2d	0.03	0.47	15.32	41.84	35.62	0.53	3.55	97.36	0.82	0.58	0.11	0.31	0.012
209.5-3a	0.09	0.56	11.28	46.22	35.97	0.67	2.31	97.10	0.88	0.66	0.10	0.24	0.015
209.5-3b	0.03	0.29	12.51	46.73	34.29	0.56	3.17	97.57	0.83	0.65	0.09	0.26	0.008
209.5-3c	0.02	1.09	0.51	34.73	57.08	0.65	0.68	94.75	0.96	0.54	0.44	0.01	0.031

*Ti/4O = number of Ti cations in spinel relative to 4 oxygens.

Analyses were done using a 20 kV accelerating voltage and a 30 nA focused beam. Standards were the natural chromite standard PSU 1436 (Cr, Al, Mg), hematite (Fe), bustamite (Mn), and synthetic olivine (Si, Mg, Fe). Counting times were 20/10 seconds of peak/background for major elements and 40/20 seconds for minor elements. Raw count rates were converted to concentrations using the ZAF data reduction scheme.

Table A2. Summary of Black Thor olivine compositions. Analytical conditions are summarized in the footnote.

Sample ID	SiO_2 (wt.%)	TiO_2 (wt.%)	Al_2O_3 (wt.%)	Cr_2O_3 (wt.%)	FeO (wt.%)	MnO (wt%)	ZnO (wt.%)	MgO (wt.%)	NiO (wt.%)	CaO (wt.%)	Na_2O (wt.%)	Total	Fe#
211-2-1a	40.75	0.052	0.014	0.015	9.76	0.15	0.011	49.35	0.24	0.000	0.007	100.35	0.10
211-2-1b	40.78	0.066	0.000	0.010	10.14	0.17	0.000	48.79	0.23	0.002	0.007	100.18	0.10
211-2-1c	41.04	0.070	0.000	0.006	10.29	0.17	0.000	48.99	0.23	0.022	0.000	100.81	0.11
211-2-2a	41.00	0.062	0.001	0.012	9.72	0.15	0.000	49.12	0.25	0.022	0.000	100.33	0.10
211-2-2b	40.66	0.061	0.000	0.000	9.81	0.16	0.019	49.08	0.29	0.030	0.000	100.10	0.10
211-2-2c	40.78	0.052	0.007	0.004	9.82	0.13	0.020	48.99	0.27	0.022	0.000	100.09	0.10
211-2-3a	41.00	0.069	0.007	0.003	9.98	0.14	0.010	48.98	0.27	0.000	0.000	100.45	0.10
211-2-4a	40.61	0.037	0.000	0.012	10.38	0.17	0.000	48.37	0.27	0.016	0.000	99.86	0.11
211-2-4b	40.73	0.054	0.002	0.000	10.29	0.16	0.008	48.23	0.28	0.003	0.018	99.77	0.11
211-2-5a	41.05	0.077	0.010	0.018	9.69	0.15	0.000	49.57	0.28	0.016	0.007	100.86	0.10
211-2-5b	40.75	0.050	0.000	0.119	8.93	0.14	0.000	49.54	0.26	0.022	0.000	99.82	0.09
264-4-1a	40.82	0.037	0.000	0.005	10.95	0.17	0.034	48.19	0.08	0.017	0.021	100.32	0.11
264-4-1b	40.83	0.070	0.000	0.004	10.93	0.18	0.000	48.57	0.08	0.014	0.000	100.67	0.11
264-4-1c	40.41	0.045	0.005	0.024	12.49	0.21	0.033	47.14	0.08	0.000	0.000	100.43	0.13
264-4-2a	40.06	0.057	0.000	0.007	12.70	0.20	0.000	46.36	0.07	0.007	0.000	99.47	0.13
264-4-2b	40.59	0.057	0.000	0.000	12.65	0.19	0.000	46.81	0.10	0.178	0.000	100.57	0.13
264-4-3a	40.34	0.057	0.000	0.021	12.72	0.21	0.000	46.47	0.10	0.013	0.006	99.93	0.13
264-4-3b	40.27	0.081	0.010	0.000	13.43	0.21	0.051	46.66	0.11	0.000	0.000	100.82	0.14
264-4-4a	40.17	0.069	0.000	0.000	13.81	0.22	0.000	45.95	0.13	0.000	0.023	100.37	0.14
251-2-1a	40.72	0.078	0.000	0.078	10.46	0.16	0.000	48.68	0.16	0.009	0.006	100.36	0.11
251-2-1b	41.23	0.067	0.016	0.066	8.73	0.14	0.000	50.06	0.13	0.016	0.000	100.44	0.09
251-2-1c	56.43	0.158	1.687	0.471	1.44	0.05	0.000	23.47	0.01	12.953	0.448	97.12	0.03
251-2-2a	39.52	0.071	0.000	0.003	11.79	0.20	0.016	47.04	0.13	0.000	0.023	98.80	0.12
251-2-2b	40.01	0.056	0.000	0.008	11.59	0.20	0.000	47.79	0.13	0.024	0.002	99.80	0.12
251-2-3a	40.72	0.063	0.000	0.000	10.23	0.16	0.000	48.71	0.12	0.018	0.035	100.05	0.11
202.5-1a	38.94	0.071	0.000	0.132	14.31	0.19	0.016	45.25	0.32	0.154	0.026	99.40	0.15
202.5-1b	40.40	0.040	0.000	0.051	15.24	0.24	0.034	44.76	0.26	0.012	0.000	101.04	0.16

Sample ID	SiO_2 (wt.%)	TiO_2 (wt.%)	Al_2O_3 (wt.%)	Cr_2O_3 (wt.%)	FeO (wt.%)	MnO (wt%)	ZnO (wt.%)	MgO (wt.%)	NiO (wt.%)	CaO (wt.%)	Na_2O (wt.%)	Total	Fe#
202.5-2a	39.44	0.050	0.000	0.017	15.66	0.25	0.000	44.15	0.29	0.000	0.006	99.86	0.17
202.5-4a	38.91	0.081	0.019	0.242	17.89	0.23	0.000	42.81	0.27	0.539	0.016	101.00	0.19
202.5-4b	39.98	0.036	0.024	0.062	15.77	0.27	0.000	43.21	0.30	0.641	0.041	100.32	0.17
202.5-4c	40.48	0.064	0.052	0.011	12.95	0.22	0.000	44.35	0.30	1.163	0.030	99.62	0.14
202.5-5a	39.72	0.070	0.000	0.057	12.68	0.18	0.000	46.77	0.26	0.132	0.000	99.87	0.13
202.5-5b	39.22	0.077	0.000	0.054	17.15	0.33	0.000	42.59	0.23	0.005	0.000	99.65	0.18
202.5-5c	40.02	0.061	0.000	0.022	12.43	0.19	0.000	46.68	0.29	0.194	0.012	99.89	0.13
209-1-2a	56.77	0.129	1.601	0.600	6.24	0.16	0.042	33.60	0.04	1.487	0.025	100.70	0.09
209-1-2b	57.34	0.128	0.953	0.236	1.48	0.11	0.010	24.17	0.03	12.518	0.201	97.17	0.03
209-1-2c	56.47	0.122	1.627	0.628	6.26	0.18	0.059	32.94	0.07	1.916	0.000	100.26	0.10
209-1-1a	54.48	0.071	4.835	0.067	1.87	0.04	0.000	22.24	0.03	13.170	0.871	97.68	0.04
209-1-1b	44.07	0.074	16.632	0.091	3.10	0.04	0.011	17.74	0.00	12.990	2.375	97.11	0.09
209-1-1c	57.62	0.076	0.646	0.000	1.74	0.08	0.000	23.87	0.03	12.836	0.151	97.05	0.04
209.5-1a	40.09	0.029	0.000	0.016	13.11	0.22	0.000	46.04	0.31	0.232	0.020	100.06	0.14
209.5-1b	40.80	0.078	0.152	0.408	14.80	0.17	0.000	41.11	0.30	3.621	0.041	101.48	0.17
209.5-1c	39.53	0.048	0.000	0.084	15.16	0.22	0.014	44.65	0.32	0.000	0.033	100.06	0.16
209.5-2a	40.13	0.054	0.025	0.032	12.62	0.20	0.000	46.67	0.32	0.004	0.009	100.07	0.13
209.5-2b	39.87	0.067	0.005	0.005	13.55	0.21	0.014	45.47	0.31	0.000	0.000	99.50	0.14
209.5-2c	39.66	0.067	0.026	0.008	15.06	0.23	0.003	44.49	0.30	0.005	0.000	99.84	0.16
209.5-2d	40.40	0.076	0.023	0.006	12.49	0.20	0.000	46.94	0.32	0.018	0.002	100.47	0.13
209.5-3a	39.98	0.059	0.005	0.001	14.28	0.22	0.078	45.22	0.26	0.000	0.004	100.11	0.15
209.5-3b	39.53	0.076	0.338	0.274	15.31	0.21	0.000	44.53	0.29	0.289	0.000	100.84	0.16
209.5-3c	40.01	0.024	0.000	0.012	14.42	0.22	0.000	45.13	0.29	0.000	0.005	100.12	0.15

Analyses were done using a 20 kV accelerating voltage and a 30 nA focused beam. Standards were the natural basaltic glass standard VG2 (Al), bustamite (Ca, Mn), and synthetic olivine (Si, Mg, Fe). Counting times were 20/10 seconds on peak/background for major elements and 40/20 seconds for minor elements. Raw count rates were converted to concentrations using the ZAF data reduction scheme.

APPENDIX B: BSE Images of Run Products

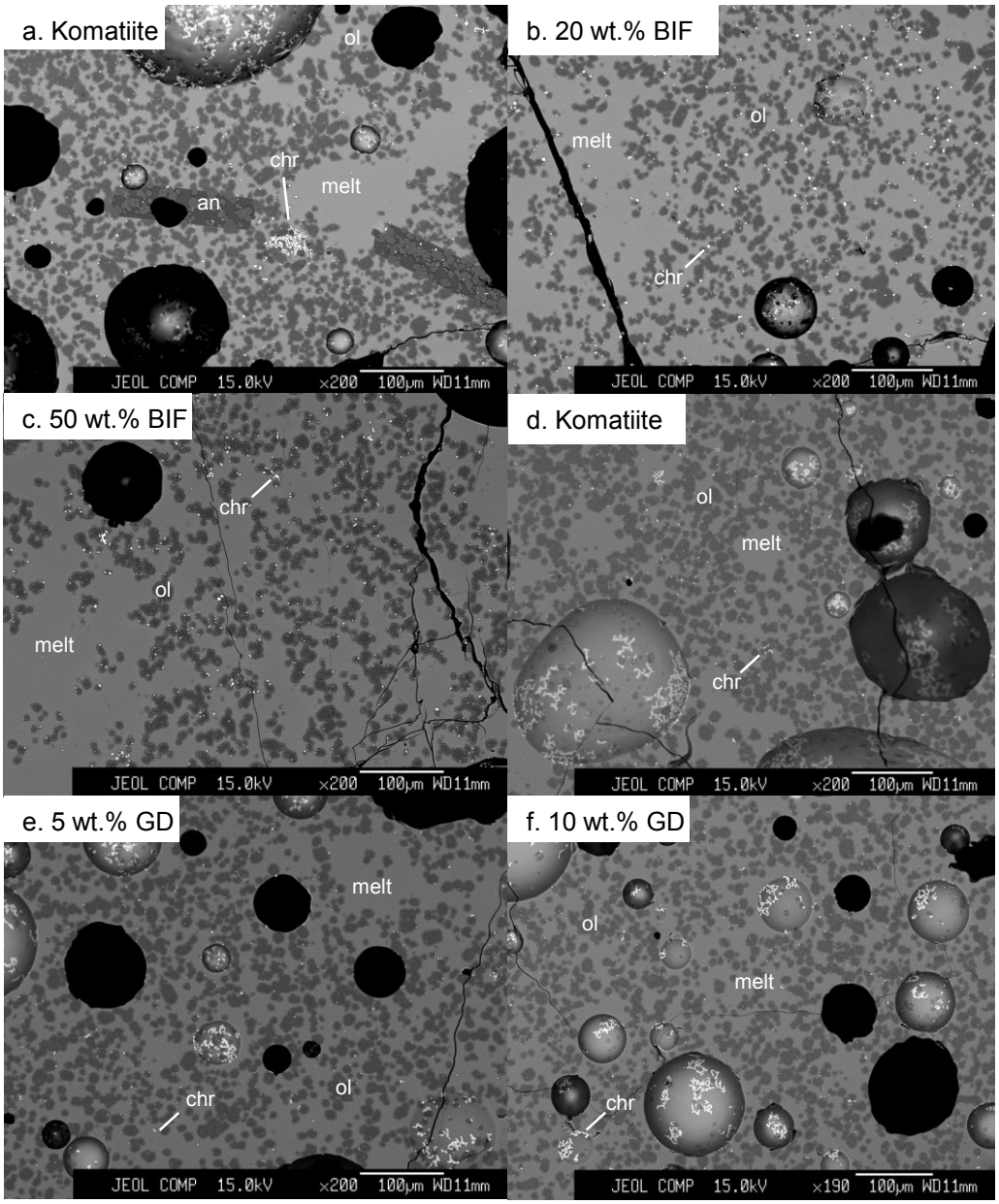

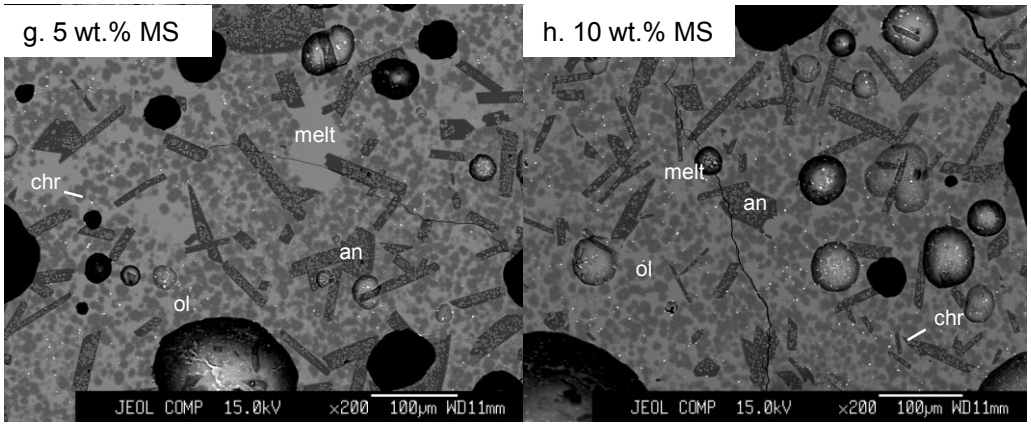

Figure B1. Back scattered electron (BSE) images of experiments run at 1192ºC. All images are at 200x magnification except f., which is at 190x. Ol = olivine, chr = chromite, an = anorthite.

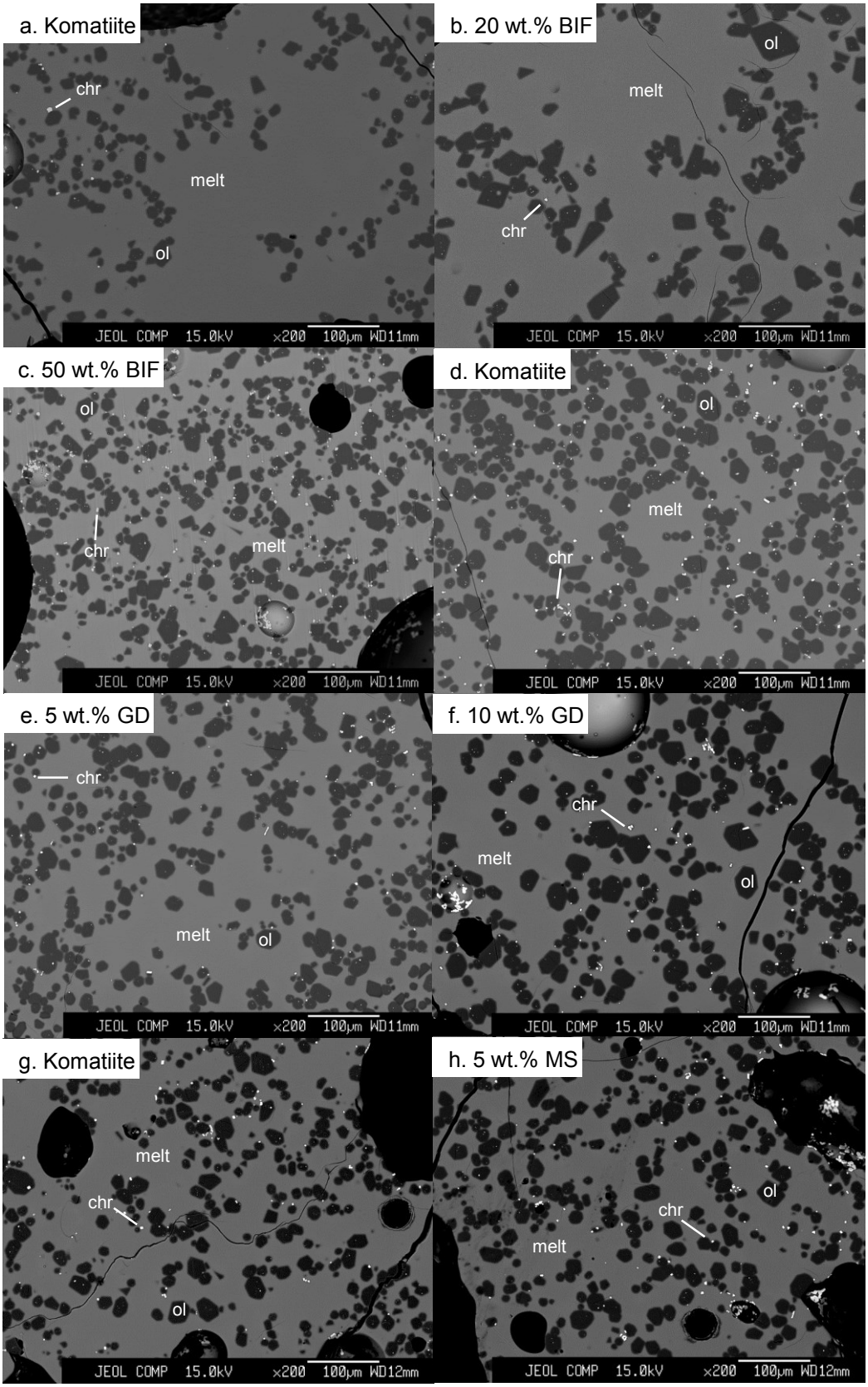
a. Komatiite
chr
melt
ol
JEOL COMP 15.0kV ×200 100μm WD11mm
b. 20 wt.% BIF
ol
melt
chr
JEOL COMP 15.0kV ×200 100μm WD11mm
c. 50 wt.% BIF
ol
chr
melt
JEOL COMP 15.0kV ×200 100μm WD11mm
d. Komatiite
ol
melt
chr
JEOL COMP 15.0kV ×200 100μm WD11mm
e. 5 wt.% GD
chr
melt
ol
JEOL COMP 15.0kV ×200 100μm WD11mm
f. 10 wt.% GD
chr
melt
ol
JEOL COMP 15.0kV ×200 100μm WD11mm
g. Komatiite
melt
chr
ol
JEOL COMP 15.0kV ×200 100μm WD12mm
h. 5 wt.% MS
ol
chr
melt
JEOL COMP 15.0kV ×200 100μm WD12mm

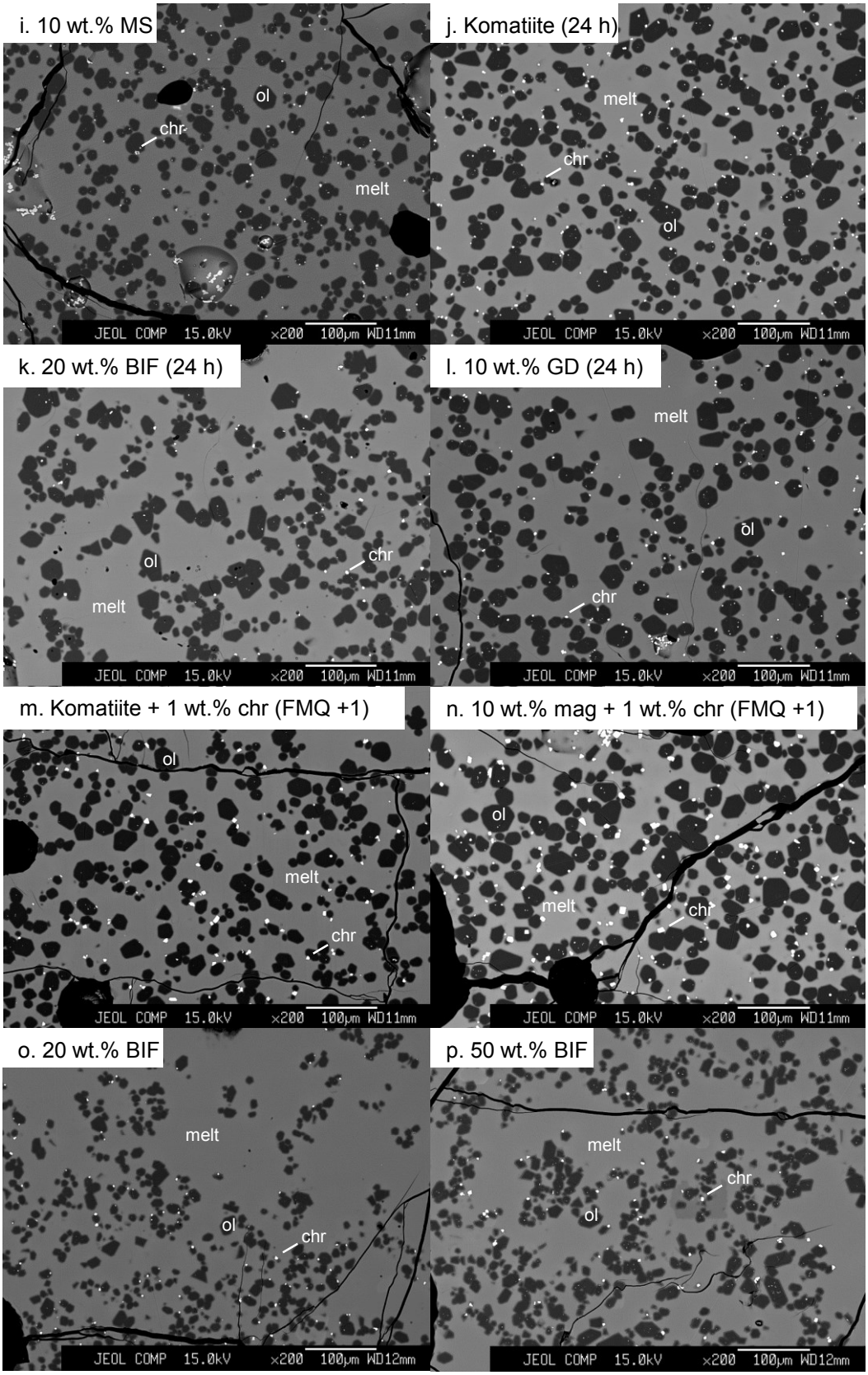
i. 10 wt.% MS
ol
chr
melt
JEOL COMP 15.0kV ×200 100µm WD11mm
j. Komatiite (24 h)
melt
chr
ol
JEOL COMP 15.0kV ×200 100µm WD11mm
k. 20 wt.% BIF (24 h)
ol
chr
melt
JEOL COMP 15.0kV ×200 100µm WD11mm
l. 10 wt.% GD (24 h)
melt
ol
chr
JEOL COMP 15.0kV ×200 100µm WD11mm
m. Komatiite + 1 wt.% chr (FMQ +1)
ol
melt
chr
JEOL COMP 15.0kV ×200 100µm WD11mm
n. 10 wt.% mag + 1 wt.% chr (FMQ +1)
ol
melt
chr
JEOL COMP 15.0kV ×200 100µm WD11mm
o. 20 wt.% BIF
melt
ol
chr
JEOL COMP 15.0kV ×200 100µm WD12mm
p. 50 wt.% BIF
melt
chr
ol
JEOL COMP 15.0kV ×200 100µm WD12mm

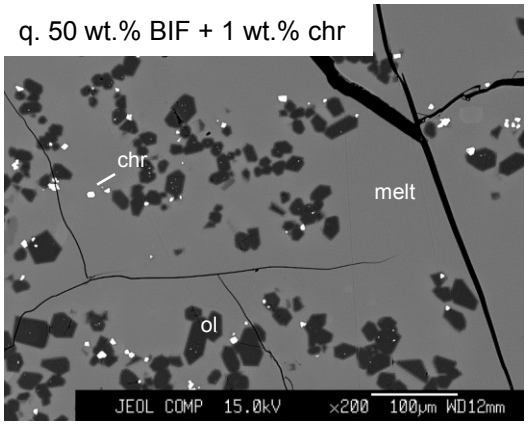

Figure B2. Back scattered electron images of experiments run at 1292ºC. All images are at a magnification of 200x. Ol = olivine, chr = chromite.

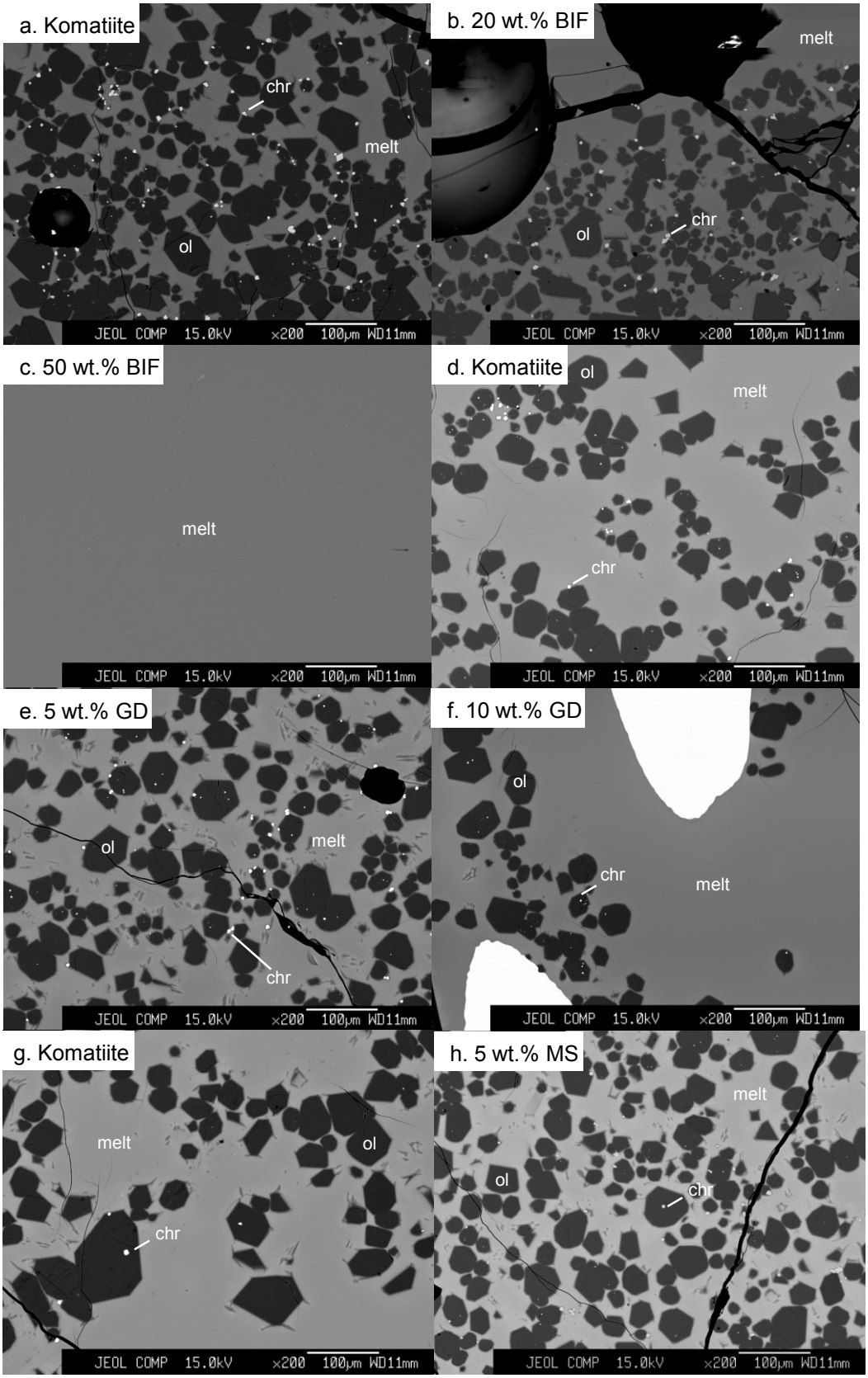
a. Komatiite
chr
melt
ol
JEOL COMP 15.0kV ×200 100μm WD11mm
b. 20 wt.% BIF
melt
ol
chr
JEOL COMP 15.0kV ×200 100μm WD11mm
c. 50 wt.% BIF
melt
JEOL COMP 15.0kV ×200 100μm WD11mm
d. Komatiite
ol
melt
chr
JEOL COMP 15.0kV ×200 100μm WD11mm
e. 5 wt.% GD
ol
melt
chr
JEOL COMP 15.0kV ×200 100μm WD11mm
f. 10 wt.% GD
ol
chr
melt
JEOL COMP 15.0kV ×200 100μm WD11mm
g. Komatiite
melt
ol
chr
JEOL COMP 15.0kV ×200 100μm WD11mm
h. 5 wt.% MS
melt
ol
chr
JEOL COMP 15.0kV ×200 100μm WD11mm

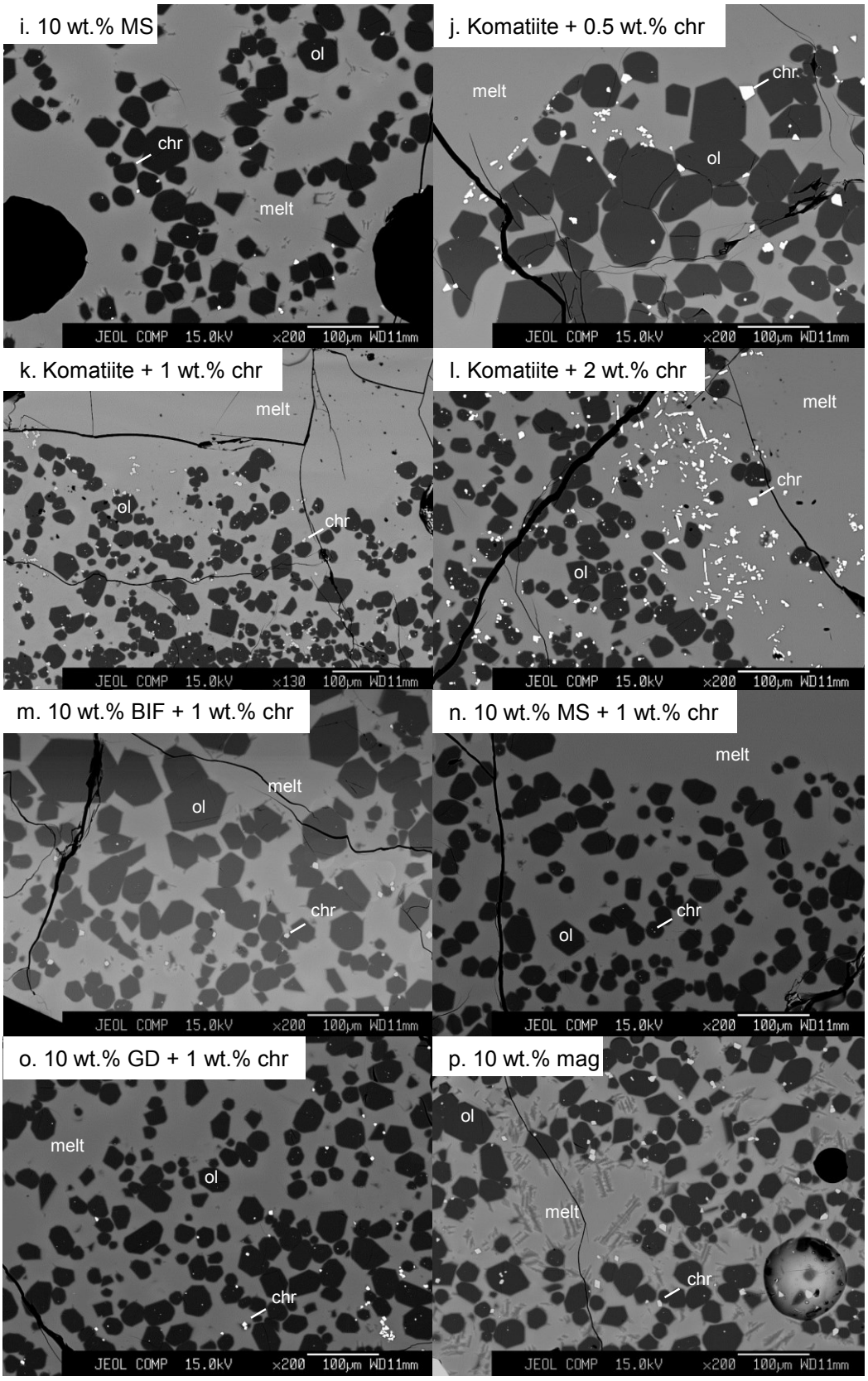
i. 10 wt.% MS
ol
chr
melt
JEOL COMP 15.0kV ×200 100μm WD11mm
j. Komatiite + 0.5 wt.% chr
chr
melt
ol
JEOL COMP 15.0kV ×200 100μm WD11mm
k. Komatiite + 1 wt.% chr
melt
ol
chr
JEOL COMP 15.0kV ×130 100μm WD11mm
l. Komatiite + 2 wt.% chr
melt
chr
ol
JEOL COMP 15.0kV ×200 100μm WD11mm
m. 10 wt.% BIF + 1 wt.% chr
melt
ol
chr
JEOL COMP 15.0kV ×200 100μm WD11mm
n. 10 wt.% MS + 1 wt.% chr
melt
chr
ol
JEOL COMP 15.0kV ×200 100μm WD11mm
o. 10 wt.% GD + 1 wt.% chr
melt
ol
chr
JEOL COMP 15.0kV ×200 100μm WD11mm
p. 10 wt.% mag
ol
melt
chr
JEOL COMP 15.0kV ×200 100μm WD11mm

q. 10 wt.% mag + 0.5 wt.% chr

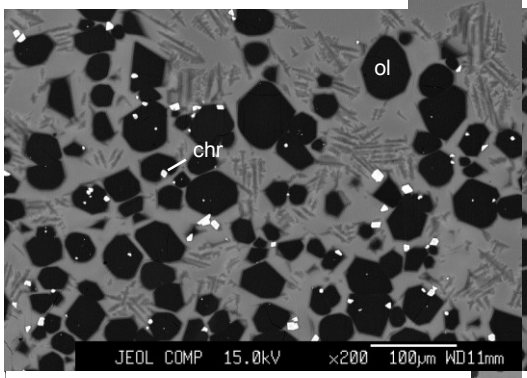

r. 10 wt.% mag + 1 wt.% chr

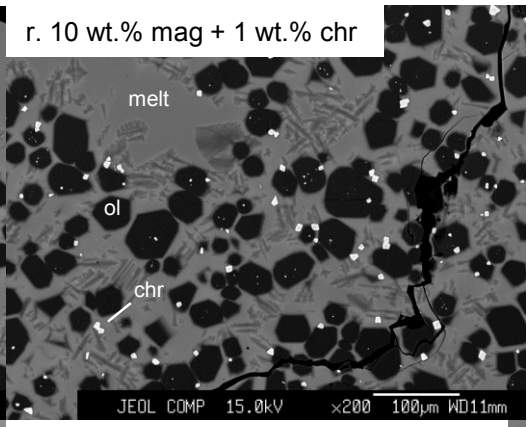

s. Komatiite + 1 wt.% chr (FMQ + 1)

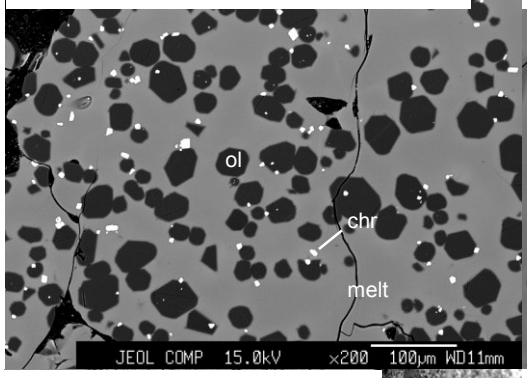

t. 10 wt.% mag + 1 wt.% chr (FMQ + 1)

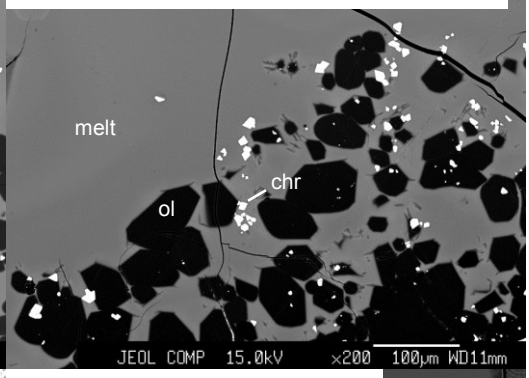

u. 20 wt.% BIF + 1 wt.% chr

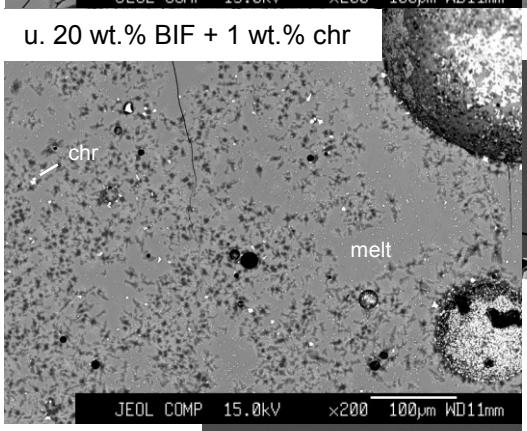

v. 40 wt.% BIF + 1 wt.% chr

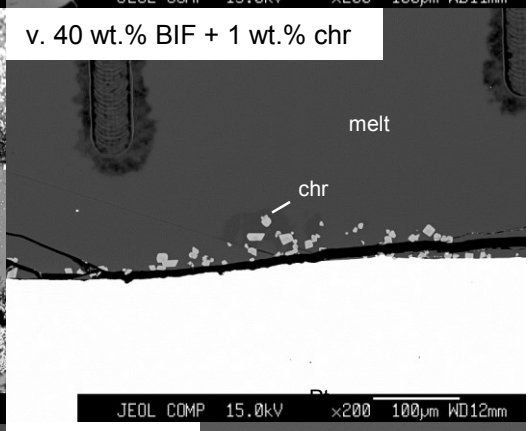

w. 30 wt.% BIF

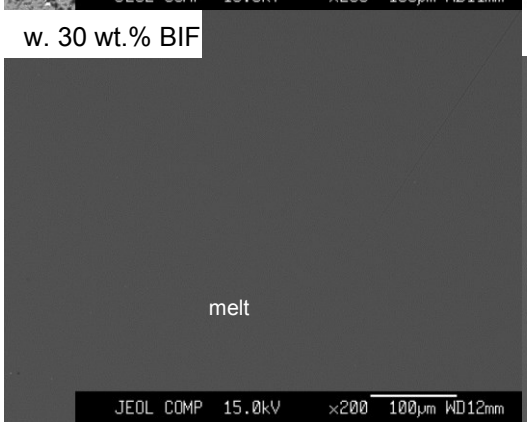

x. 40 wt.% BIF

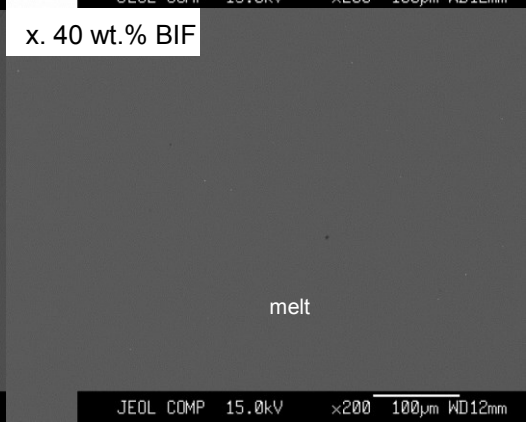

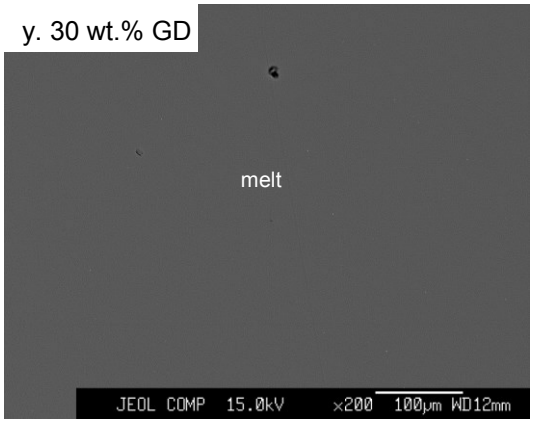

Figure B3. Back scattered electron images of experiments run at 1392ºC. All images are at a magnification of 200x except k., which is at 130x. Ol = olivine; chr = chromite; Pt = platinum loop.

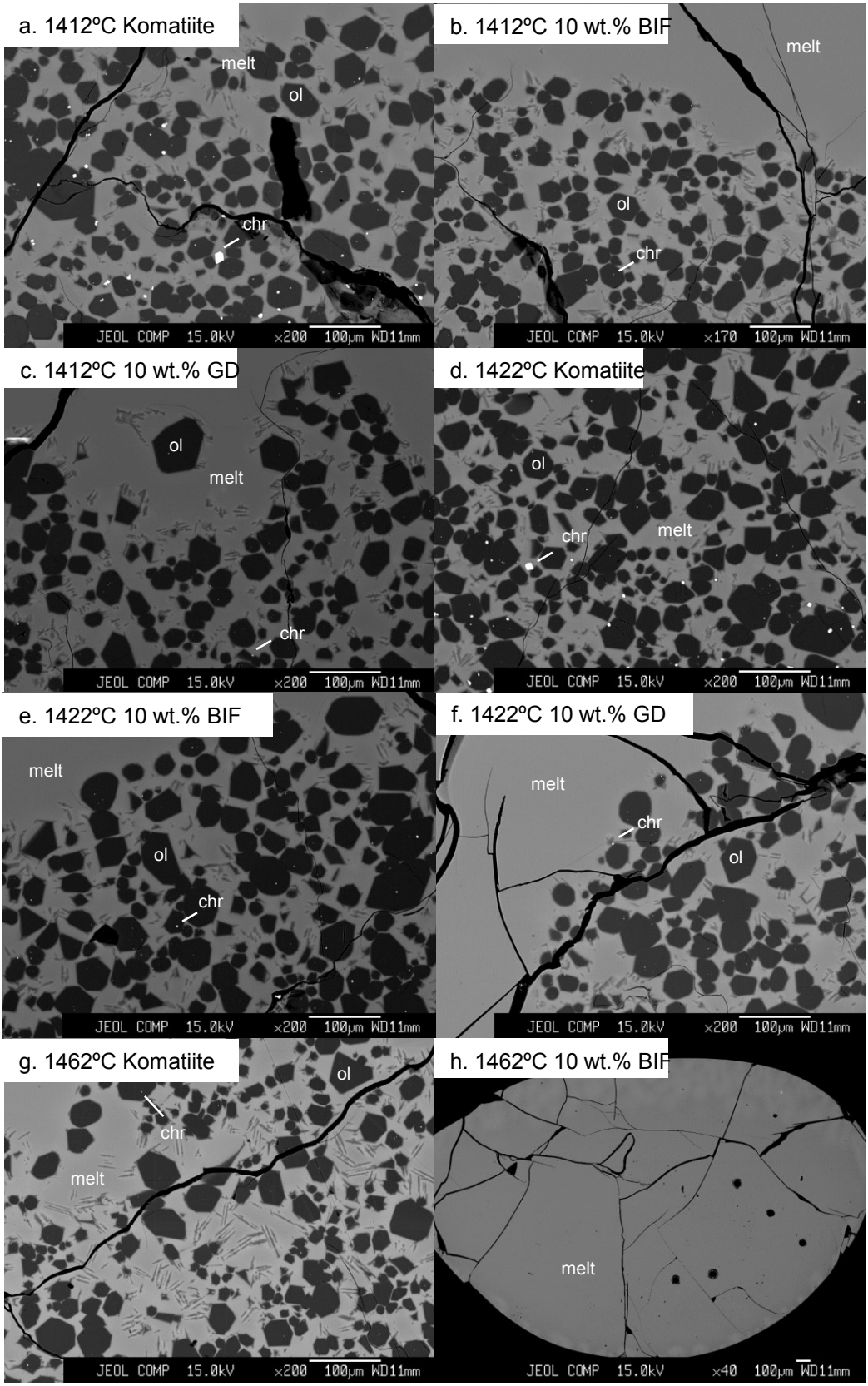
a. 1412ºC Komatiite
melt
ol
chr
JEOL COMP 15.0kV ×200 100µm WD11mm
b. 1412ºC 10 wt.% BIF
melt
ol
chr
JEOL COMP 15.0kV ×170 100µm WD11mm
c. 1412ºC 10 wt.% GD
ol
melt
chr
JEOL COMP 15.0kV ×200 100µm WD11mm
d. 1422ºC Komatiite
ol
chr
melt
JEOL COMP 15.0kV ×200 100µm WD11mm
e. 1422ºC 10 wt.% BIF
melt
ol
chr
JEOL COMP 15.0kV ×200 100µm WD11mm
f. 1422ºC 10 wt.% GD
melt
chr
ol
JEOL COMP 15.0kV ×200 100µm WD11mm
g. 1462ºC Komatiite
ol
chr
melt
JEOL COMP 15.0kV ×200 100µm WD11mm
h. 1462ºC 10 wt.% BIF
melt
JEOL COMP 15.0kV ×40 100µm WD11mm

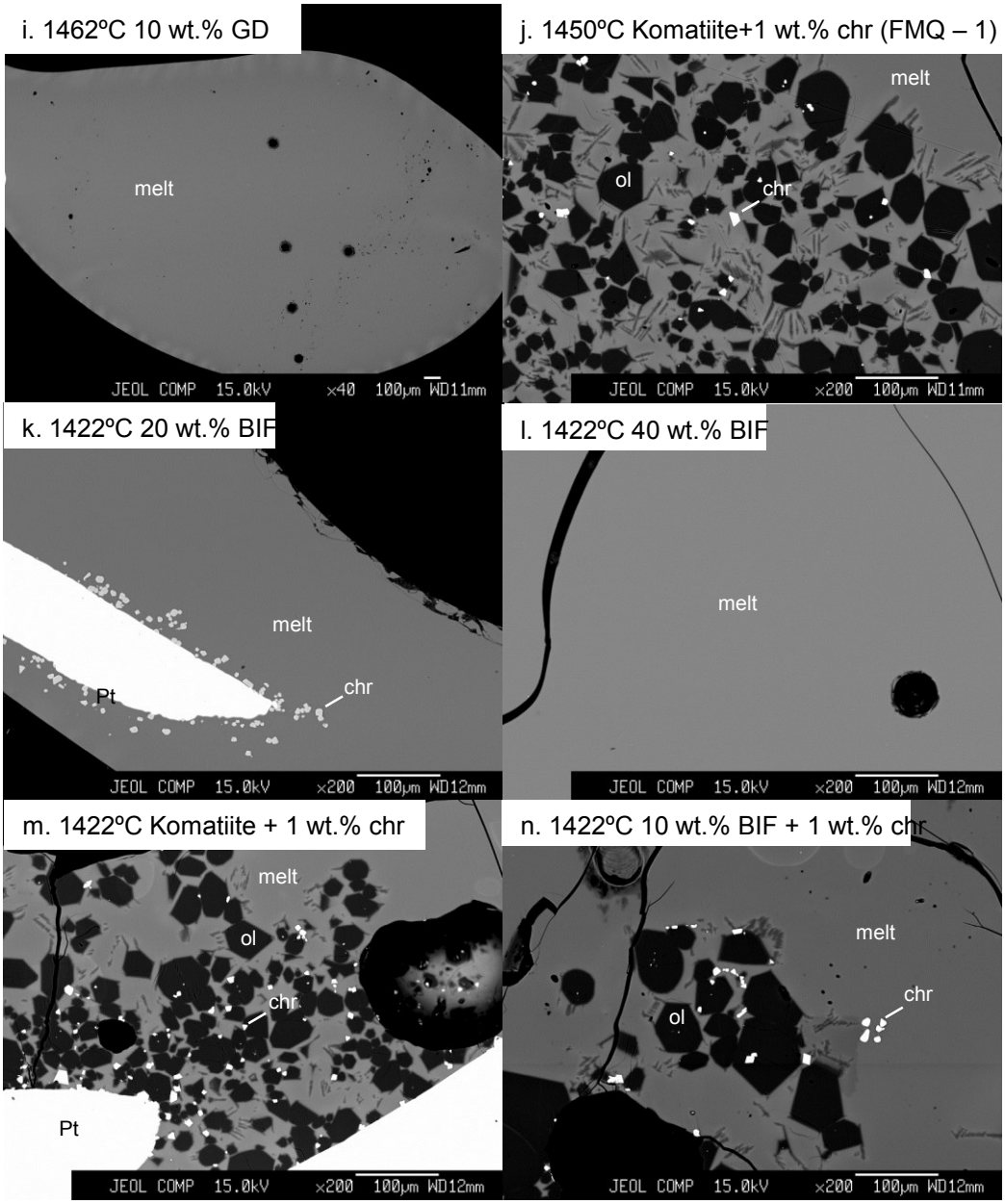

Figure B4. Back scattered electron images of experiments run above 1450ºC. All images are at a magnification of 200x, with the exceptions of b., which is at 130x, as well as h. and i., which are at 40x. Ol = olivine, chr = chromite, Pt = platinum loop.

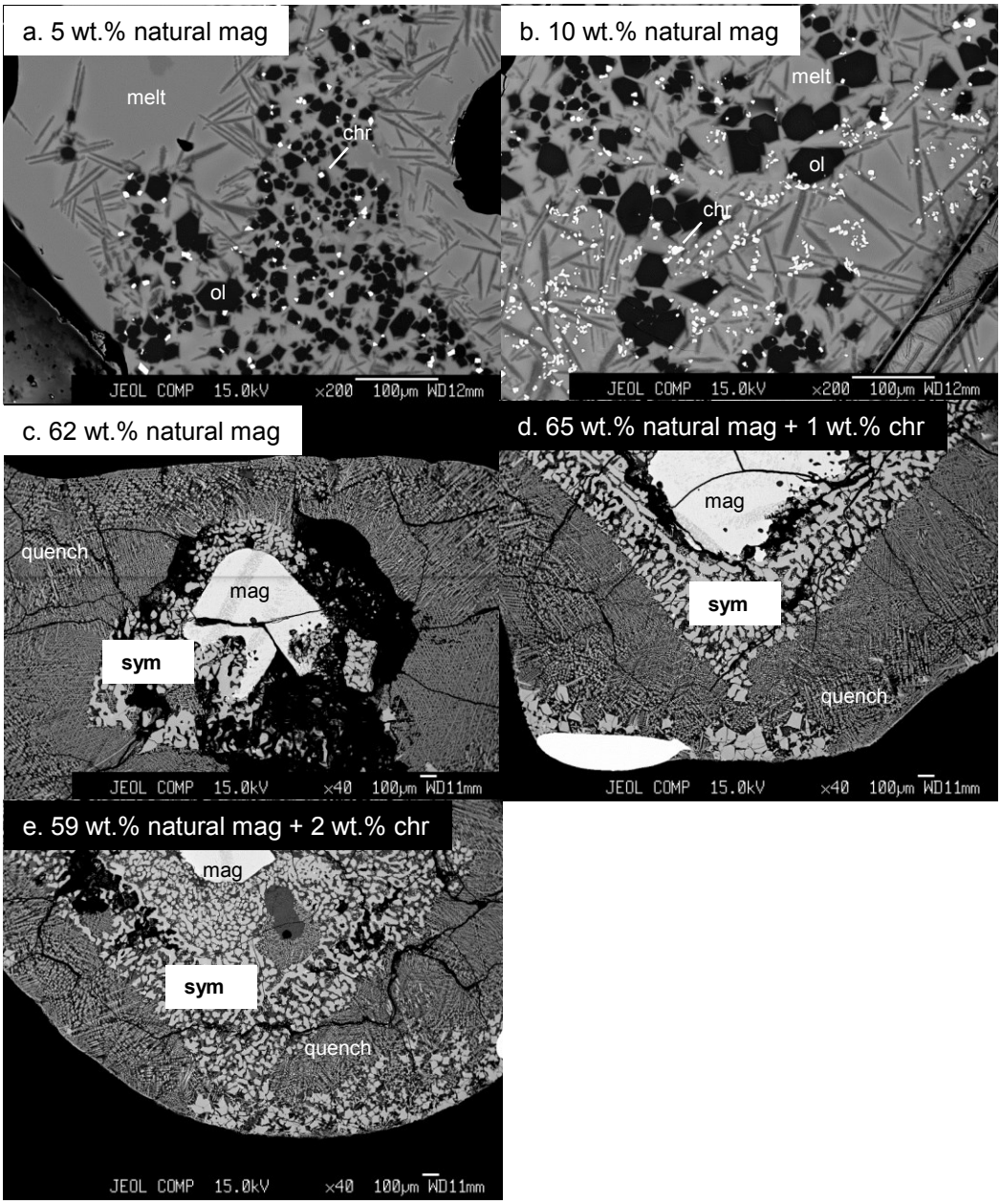

Figure B5. Back scattered electron images of experiments containing natural magnetite. a. and b. are at a magnification of 200x; c, d, and e are at 40x. Ol = olivine, chr = chromite, mag = relict magnetite core, sym = magnetite-melt symplectite, quench = quench texture.